

Design and optical characterization of specialty optical fibers
for the stable transmission of vector-vortex beams

by

Manish SHARMA

MANUSCRIPT-BASED THESIS PRESENTED TO ÉCOLE DE
TECHNOLOGIE SUPÉRIEURE IN PARTIAL FULFILLMENT FOR THE
DEGREE OF DOCTOR OF PHILOSOPHY
Ph.D.

MONTREAL, June 22, 2021

ÉCOLE DE TECHNOLOGIE SUPÉRIEURE
UNIVERSITÉ DU QUÉBEC



This Creative Commons license means that it is permitted to distribute, print or save in another medium part or all of this work provided the author is acknowledged, that these uses are made for non-commercial purposes and that the content of the work has not been modified.

BOARD OF EXAMINERS
THIS THESIS HAS BEEN EVALUATED
BY THE FOLLOWING BOARD OF EXAMINERS

Mr. Bora Ung, Thesis Supervisor
Department of Electrical Engineering, École de technologie supérieure

Mme Nicole R. Demarquette, President of the Board of Examiners
Department of Mechanical Engineering, École de technologie supérieure

Mr. Ricardo Izquierdo, Member of the jury
Department of Electrical Engineering, École de technologie supérieure

Mr. Martin Rochette, External Evaluator
Department of Electrical and computer engineering, McGill University

THIS THESIS WAS PRESENTED AND DEFENDED
IN THE PRESENCE OF A BOARD OF EXAMINERS AND PUBLIC
11 JUNE 2021
AT ÉCOLE DE TECHNOLOGIE SUPÉRIEURE

ACKNOWLEDGMENT

The undertaking of this PhD has truly been a new experience for me, and it would not have been possible without the love, support, and guidance of these amazing peoples. First and foremost, I express my heartfelt gratitude to my director Professor Bora Ung for his real-time support, constant encouragement, patience, and constructive feedbacks followed by the focused supervision in the course of my doctoral studies. Thank you for all the trust, encouragement, and motivation all these years. Thank you for guiding me in becoming a researcher and helping me develop scientific rigor. Words fall short when it comes to acknowledging Professor Bora for his unyielding moral and financial support towards your professionalism in my academic and research journey. I would also like to thank Professor François Blanchard for helping me performing experiments in his lab, while giving me all needful suggestion and guidance. Special thanks to all the members of the jury's for evaluating my PhD thesis. Thank you for your valuable feedback and suggestions.

I would also like to thank all my colleagues from the research group for their moral support in and outside the lab. In particular special thanks to Prabin Pradhan, for his immense support both in personal and professional life for first 2 years of my work at ETS. He is main guiding force in my life apart from Professor Bora Ung in my transformation from a complete mechanical engineer to an effective researcher (an ongoing process) in the field of optics. I would also like to thank Dr. Dipankar Sengupta, Dr. Satyendra K. Mishra and Saeed Azad for their inputs in lab. My special thanks to Koffi Novignon for coming forward to help me with the review of French writing. In addition to this, I would like to thank Fatemeh Amir Khan in helping me perform lab experiments in François Blanchard's lab. Apart from the academic people, I would like to acknowledge the technical assistance received from Mr. André Zalzal, Mr. Samuel Gagné, Mr. Normand Gravel and Mr. Youssef Bekbouti.

I would like to express my sincere gratitude to my parents Mr. Chhitar Singh Sharma and Ms. Pravesh Sharma, my brother Pankaj, my sister Radha for their unending love and support

in my life. Thanks for all the love mom and dad. It was only possible with their blessing and unconditional love.

I am eternally grateful to my spouse Richa Upadhyay, who patiently accepted continuation of my study, while waiting for my real job. Thank you for the support, encouragement and push you gave me at difficult times. Thank you for allowing me to continue my passion in exploring and learning new things. Thank you to my child, Subhi Sharma a wonderful daughter and source of energy in my life.

Finally, I would like to acknowledge the financial supports extended from the Fonds de recherche du Québec - Nature et technologies for the duration of 3 years of my PhD.

Conception et caractérisation optique de fibres optiques spécialisées pour la transmission stable de faisceaux vector-vortex

Manish SHARMA

RÉSUMÉ

De nombreuses recherches ont été développées ces dernières années pour explorer des faisceaux d'intensité complexes tels que le vortex optique. Le vortex optique est une classe particulière de faisceaux lumineux qui montre des profils d'intensité en forme de beignet et caractérisé par un trou central noir. Ce vortex est constitué soit des faisceaux à moment orbital angulaire (de l'acronyme anglais *orbital angular momentum* (OAM) beams) ou des faisceaux de polarisation à vecteurs cylindriques (de l'acronyme anglais *cylindrical vector beams* (CVBs)). Compte tenu de ce profil d'intensité unique, les faisceaux vortex ont démontré des avancées prometteuses dans de nombreuses applications telles que: l'optique quantique, la microscopie optique, la manipulation de particules, la détection, le piégeage optique et le multiplexage par répartition spatiale. Les faisceaux vortex (avec un profil d'intensité en forme de beignet) sont impliqués dans des applications liées à la microscopie à super résolution où les faisceaux annulaires permettent de briser la limite de diffraction. Une autre application est l'utilisation de vortex optiques dans des interactions lumière-matière (avec des applications possibles en spectroscopie moléculaire) qui pourraient conduire à des résultats inédits en comparaison avec les faisceaux gaussiens conventionnels.

Ces applications innovantes des faisceaux vortex ont motivé davantage de travaux de recherches afin de les explorer lorsqu'ils se propagent à la fois en espace libre et dans une fibre optique. De plus, des innovations supplémentaires dans les technologies actuelles sont vitales afin de garantir le maintien d'une haute pureté dans la génération et la transmission de ces faisceaux uniques. Différentes techniques de création des faisceaux vortex ont été par conséquent explorées par les chercheurs: on peut citer entre autres: la lame de phase hélicoïdale, le modulateur de phase spatial, les métamatériaux nanostructurés. Dans cette thèse nous étudions la conception, l'optimisation et la caractérisation de fibres optiques adaptées à la propagation de faisceaux vortex optiques. L'objectif principal consiste à développer une fibre optique adaptée à une transmission stable du vortex optique, tout en conservant une pureté de mode élevée.

Dans ce travail, nous proposons une nouvelle conception de fibre qui prouve un nouveau régime de guidage nommé régime infiniment mono-radial, régime où la fibre ne supporte que les modes d'ordre radial fondamental pour une très grande plage de longueurs d'onde. Cette propriété est importante pour la transmission stable et efficace des faisceaux OAM et CVBs mono-radiaux qui sont le sujet d'études intenses. Un modèle basé sur la méthode des éléments finis a été développé et simulé pour étudier la fibre à cristaux photoniques (cœur

annulaire), ce qui facilite l'optimisation des paramètres permettant de trouver un nouveau régime de guidage et d'évaluer les propriétés souhaitées de la fibre pour les faisceaux vortex. Les résultats des simulations sont en accord avec les résultats du modèle théorique. Ensuite, des simulations numériques sont faites pour générer un supercontinuum non-linéaire de faisceaux vortex à l'aide d'un laser à impulsions femtoseconde 835 nm utilisant des paramètres optimisés de conception de fibre. Dans la deuxième partie de ce travail, la fibre théorique conçue et simulée dans la première partie est fabriquée et caractérisée expérimentalement pour la transmission de vortex optique. Cette dernière affiche une stabilité et une pureté modale plus élevée dans la fibre. Dans cette expérience, les faisceaux OAM et CVBs sont générés à l'aide d'une lame à phase hélicoïdale commerciale dans un espace libre. Ces faisceaux sont ensuite envoyés dans une fibre fabriquée afin d'analyser la pureté et la stabilité du mode après propagation à travers la fibre. Cette expérience permet une meilleure compréhension de la transmission de ces faisceaux dans la fibre. Dans la dernière partie de cette thèse, nous proposons une fibre avec un cœur annulaire radialement anisotrope pour une nouvelle caractéristique de guidage, c'est-à-dire que la fibre pourrait permettre une co-propagation stable (avec un couplage intermodal inférieur) de différents types de faisceaux OAM (formés par superposition des modes radiales (TE) et polarisés azimutalement (TM) ou modes hybrides (HE / EH)). Une manipulation précise des paramètres de la fibre proposée permet une dégénérescence des modes TE et TM (généralement non dégénérés), tout en conservant une dégénérescence plus des modes hybrides (HE / EH)). De plus, un tel design de fibre pourrait permettre un régime de guidage unique dans lequel le mode polarisé radialement (TM_{01}) ou azimutalement (TE_{01}) devient le mode fondamental guidé dans la fibre à la place du mode HE_{11} . Nous croyons que ces résultats sont pertinents au développement de la prochaine génération de systèmes de détection et de communication optiques.

Mots-clés : Optical vortex, orbital angular momentum beam, annular - core photonic crystal fiber, radially anisotropic ring fiber, cylindrical vector beams.

Design and optical characterization of specialty optical fibers for the stable transmission of vector-vortex beams

Manish SHARMA

ABSTRACT

In recent years, significant research has been dedicated towards exploring complex structured light beams such as optical vortices, a class of light beams that demonstrate doughnut shape intensity profiles and characterized by dark central hole, formed either due to phase singularities (known as *orbital angular momentum* (OAM) beams) or polarization singularities (*cylindrical vector beams* (CVBs)). Owing to such unique optical properties, vortex beams have demonstrated promising advances in numerous applications such as: quantum optics, optical microscopy, particle manipulation, sensing, optical trapping, and space division multiplexing. For example, vortex beams (with doughnut shaped intensity profile) are well-established in applications related to stimulated emission depletion (STED) super resolution microscopy, where annular beams enable breaching the diffraction limit. Another application is associated to using optical vortices in unique light-matter interactions (with possible applications in molecular spectroscopy), which could lead to new physical phenomenon not observable with conventional Gaussian beams.

These captivating applications of vortex beams have inspired more research work in probing these beams in both free space and guided fiber optics. Moreover, further innovation in currently existing technology is vital in order to realize the high purity generation and stable transmission of these exotic beams. Consequently, researchers and engineers have been on the forefront to explore different generation techniques such as: spiral phase plate, spatial light modulator (SLM), and nanostructured metamaterials, to name few. In parallel, numerous novel fiber designs have been proposed and developed towards the stable transmission of optical vortex. This thesis examines specific designs, optimization and characterization of optical fibers tailored for the propagation of optical vortex beams. The principal objective is to develop an optical fiber suitable for the stable transmission of optical vortex, which maintains high mode purity.

In this thesis, we propose a novel fiber design that demonstrates a new guiding regime termed endlessly mono-radial, where the fiber supports only guided modes of the fundamental radial order over a very large wavelength range. The latter property is important for the stable and broadband transmission of mono-radial CV and OAM beams. A finite element method (FEM) based model was developed for studying ring shaped (i.e. annular) core photonic crystal fiber. Moreover a systematic parameter investigation allows one to find new guiding regimes and evaluate fiber properties desirable for vortex beams. The simulation

results are compared with a theoretical analytical model based on the exact solution of Helmholtz equation. This is followed by a demonstration of numerical simulation for non-linear supercontinuum generation of vortex beams using 835 nm femtosecond pulse laser employing optimized fiber design parameters. In the second part of thesis, fiber theoretical designed and simulated in first part, is later fabricated and experimentally characterized for transmission of optical vortex, which displays higher mode stability and purity in fiber. In this experiment, OAM and CV beams are generated using S-plate (commercially available spiral phase plate) in free space and launched in fabricated fiber for analyzing mode purity and stability upon propagating through the fiber. This experimental characterization allows a deeper understanding of the CV and OAM beams transmission in fiber. In the last part of thesis, we proposed a radically new design: the radially anisotropic ring-core fiber for novel guiding characteristic. We show that the proposed fiber could in principle allow the stable co-propagation (with lower intermodal coupling) of different kind of OAM beams formed by the superposition of both the radially (TE) and azimuthally (TM) polarized modes, and coherent combination of hybrid (HE / EH) modes. This feat is possible because the proposed fiber enables to bridge the non-degeneracy of the TE and TM modes, without affecting the degeneracy of hybrid (HE / EH) modes. In addition to this, this fiber design could unlock further unconventional waveguiding regime, where either the doughnut-shaped radially or azimuthally polarized mode becomes the fundamental mode of the fiber in place of usual Gaussian-like HE_{11} mode. We hope that these findings will help in further development of next generation optical sensing and communication systems.

Keywords: Optical vortex, orbital angular momentum beam, annular - core photonic crystal fiber (AC-PCF), radially anisotropic ring fiber, cylindrical vector beams.

TABLE OF CONTENTS

	Page
INTRODUCTION	1
CHAPTER 1 LITERATURE REVIEW AND BACKGROUND INFORMATION	11
1.1 Cylindrical vector beams	11
1.1.1 Generation of cylindrical vector beams	13
1.1.2 Applications of cylindrical vector beams	15
1.2 Orbital angular momentum beams.....	16
1.2.1 Generation of orbital angular momentum beams.....	17
1.3 OAM and CV beams in optical fibers.....	19
1.3.1 OAM and CV beams propagation in optical fibers	22
1.3.2 Photonic crystal fibers.....	23
1.3.3 Radially anisotropic fiber.....	25
1.4 OAM and CV beams characterization	27
1.5 Summary.....	28
CHAPTER 2 ENDLESSLY MONO-RADIAL ANNULAR CORE PHOTONIC CRYSTAL FIBER FOR THE BROADBAND TRANSMISSION AND SUPERCONTINUUM GENERATION OF VORTEX BEAMS ...	31
Résumé.....	31
2.1 Abstract.....	32
2.2 Introduction.....	32
2.3 Description of the annular-core photonic crystal fiber design.....	34
2.4 Optimization of fiber parameters for supercontinuum generation in the visible- near-infrared.....	37
2.5 Chromatic dispersion engineering	40
2.6 Numerical simulation of supercontinuum generation in AC-PCF.....	43
2.7 Conclusion	48
2.8 Appendix.....	49
Methods.....	49
CHAPTER 3 TRANSMISSION OF ORBITAL ANGULAR MOMENTUM AND CYLINDRICAL VECTOR BEAMS IN A LARGE-BANDWIDTH ANNULAR CORE PHOTONIC CRYSTAL FIBER	55
Résumé.....	55
3.1 Abstract.....	56
3.2 Introduction.....	56
3.3 Mode structure and attenuation of AC-PCF	58
3.4 Experimental setup and discussion	59
3.5 Conclusions.....	65
3.6 Appendix.....	66

Experimental setup for generating fork interferogram pattern of vortex beams66
Mode purity method.....67

CHAPTER 4 RADIALLY ANISOTROPIC RING-CORE OPTICAL FIBER:
 TOWARDS VECTOR-VORTEX GUIDED TRANSMISSION
 USING THE FULL MODAL SPACE69

Résumé.....69

4.1 Abstract70

4.2 Introduction.....70

4.3 Fiber design parameters72

4.4 Results and discussion74

4.5 Conclusion83

4.6 Appendix.....84

CONCLUSION.....87

STATEMENT OF ORIGINAL CONTRIBUTION & FUTURE RECOMMENDATIONS..91

ANNEXE I PRINCIPLES OF THE FINITE-ELEMENT METHOD95

ANNEXE II BEAM SIZE MEASUREMENT (KNIFE – EDGE METHOD).....99

LIST OF PUBLICATIONS105

BIBLIOGRAPHY107

LIST OF TABLES

	Page
Table 2.1	
Linear and nonlinear optical properties of the HE_{21} mode in two designs of silica AC-PCF optimized for supercontinuum generation at 835 nm wavelength.	42

LIST OF FIGURES

		Page
Figure 0.1	Schematic diagram of different data multiplexing techniques, including space division multiplexing a new degree of freedom for data multiplexing in future communication systems.....	2
Figure 0.2	Schematic overview of working principle of STED microscopy, (a) shows the schematic of light emission from a conventional microscopy (b) schematic of a depletion laser “doughnut shape”, and effective point spread function (PSF) demonstrate super resolution spot.....	4
Figure 0.3	Schematic outline of the overall thesis work	7
Figure 1.1	Focusing properties with high-NA lenses for different beam shapes; (a) Gaussian beam results in complex polarization, while (b) a radially polarized beam yields an intense, well-defined electric field along the optic axis	11
Figure 1.2	Intensity distribution of cylindrical vector beams: TE_{01} , TM_{01} , HE_{21}^e and HE_{21}^o , the arrows depict polarization orientations	12
Figure 1.3	Experimental setup for measuring the polarization dependence of LPFG (top), the transmission spectra of LPFGs (bottom).....	15
Figure 1.4	The intensity profile and phase information of regular Gaussian beam ($l = 0$) and OAM beams ($l = +1$) and ($l = +2$)	17
Figure 1.5	A spiral phase plate can generate a helically phased beam from a Gaussian. In this case $\ell=0 \rightarrow \ell=2$,	18
Figure 1.6	Three approaches to convert a Gaussian beam into an OAM beam: (a) a spiral phase plate, (b) a phase hologram with a spiral phase pattern, or (c) a phase hologram with a “fork” pattern. In this example, the conversion to an OAM beam with $\ell=+3$ is depicted.....	19
Figure 1.7	Phase and intensity profiles of OAM ($l = \pm 1$) formed by combination of (a) $TE_{0,1} + iTM_{0,1}$ and (b) $HE_{2,1}^e + iHE_{2,1}^o$ modes.....	21
Figure 1.8	Annular fiber geometry (top view, and profile).....	23

Figure 1.9	Cross section and structure parameters of (a) ring photonic crystal fiber (PCF) (b) the twisted air-core PCF (c) Cross-section and main parameters of C-PCF.....	25
Figure 1.10	Schematic diagram of radially anisotropic ring-core fiber with refractive index profiles shown along the radial and azimuthal axes (n_r & n_ϕ).....	26
Figure 1.11	Experimental identification of the generated PCVBs (TM_{01} , TE_{01} , even and odd HE_{21} beams) via the rotation of a linear polarizer located in front of the CCD camera	27
Figure 2.1	(a) Schematic of the cross-section of AC-PCF (b) Simulated intensity profiles of the first 4 guided vector modes. (c) Intensity and phase distributions of the $OAM_{\mp 11}$ modes supported by the AC-PCF.....	35
Figure 2.2	(a) Localization of the endlessly mono-radial-order regime in the normalized λ/Λ vs d/Λ parameter space of AC-PCFs (b) Modal cut-offs for the TE_{01} , HE_{21} , TM_{01} , HE_{31} , EH_{11} and HE_{12} modes predicted by analytical theory and validated by full-vector FEM	36
Figure 2.3	(a) Effective mode area, and (b) nonlinear parameter of the HE_{21} mode at $\lambda = 835$ nm in a silica AC-PCF operating in the endlessly mono-radial-order guiding regime.....	38
Figure 2.4	(a) Effective index of the HE_{21} mode and (b) its minimum effective index separation inside the LP_{11} group at $\lambda = 835$ nm in a silica AC-PCF operating in the endlessly mono-radial-order regime	39
Figure 2.5	(a) Plot of the group velocity chromatic dispersion and (b) dispersion slope of HE_{21} mode at $\lambda = 835$ nm in silica AC-PCF within the endlessly mono-radial-order regime	41
Figure 2.6	(a) Effective index of the HE_{21} mode and (b) its minimum effective index separation inside the LP_{11} group at $\lambda = 835$ nm in a silica AC-PCF operating in the endlessly mono-radial-order regime	42
Figure 2.7	(a) Pulse spectral and temporal profiles as a function of propagation in (a) Fiber 1 with $\Lambda = 1.3$ μm and $d/\Lambda = 0.34$, and (b) Fiber 2 with $\Lambda = 0.5$ μm and $d/\Lambda = 0.2$ for 10 kW peak input power.....	45

Figure 2.8	Output pulse spectra after 20 cm propagation in AC-PCF with (a) $\Lambda = 1.3 \mu\text{m}$ and $d/\Lambda = 0.34$ (Fiber 1), and (b) $\Lambda = 0.5 \mu\text{m}$ and $d/\Lambda = 0.2$ (Fiber 2) as a function of input pulse peak powers P_p47
Figure 2.9	(a) Unit cell used in the FEM solver of the (b) effective index of the fundamental space-filling mode (n_{FSM}) as a function of normalized wavelength (λ/Λ) for different values of d/Λ aspect ratios. A comparison between the full-vector calculations with the approximate empirical relation.49
Figure 2.10	Profiles of (a) TM_{01} (b) HE_{31} and (c) HE_{12} modes exactly at the modal cut-off threshold when $f_p = 40\%$ for an exemplar AC-PCF with $d/\Lambda = 0.5$ where the dashed white lines indicate the core region of interest of effective radius $b = 2\Lambda/3$51
Figure 2.11	(a) OAM charge weights in Fiber 1 of generated OAM beam with topological charge ($l = -1$) at 835 nm (b) OAM mode purity as a function of wavelength for Fiber 1 and Fiber 2.52
Figure 3.1	(a) Cutback losses of the used annular core photonic crystal fiber (AC-PCF), where the scanning electron microscope (SEM) image of the actual AC-PCF is shown in inset. (b) V-parameter of the AC-PCF as a function of the input wavelength in the 300–1800 nm range as calculated with finite-element method (FEM) simulations.59
Figure 3.2	Experimental setup for launching and imaging (a) orbital angular momentum (OAM) beams and (b) cylindrical vector beams (CVB) (TE01 and TM01) in the AC-PCF60
Figure 3.3	Experimental identification of the obtained CVBs (radial TM01 and azimuthal TE01) before (top two rows) and after propagation in the AC-PCF (bottom two rows) through rotation of the analyzer positioned in front of the CCD camera61
Figure 3.4	(a,b,c) Interference pattern of a $L = +1$ doughnut-shaped OAM beam with a reference Gaussian beam as they progressively merge to generate a single fork pattern before (Top row) and (d,e) after propagation in the fiber (Bottom row)62
Figure 3.5	Mode purity of OAM beam at fiber output as a function of wavelength (from 805 to 845 nm in step on 1 nm using tunable laser), Inset: output beam images for selected wavelengths64

Figure 3.6	Experimental setup for recording the interference pattern of the Gaussian beam (path identified in green) and the vortex OAM beam (path identified in red) on the CCD camera.	66
Figure 3.7	Azimuthal Intensity distribution of a typical vortex OAM beam at 821 nm (inset image of OAM with azimuthal ring).....	68
Figure 4.1	Schematic diagram of the anisotropic ring-core fiber showing the radial and azimuthal axes along which the refractive index profile is defined (n_r & n_ϕ), and for two general cases of core anisotropy (b) $n_\phi > n_r$ and (c) $n_\phi < n_r$	73
Figure 4.2	(a) Effective index (n_{eff}) of the HE_{11}^e and (c) HE_{21}^e modes, while (b) effective index separation (Δn_{eff}) between HE_{11}^e and HE_{11}^o and (d) HE_{21}^e and HE_{21}^o modes.....	75
Figure 4.3	(a) Effective index (n_{eff}) of the TM_{01} and (b) TE_{01} mode (c) Effective index separation (Δn_{eff}) between TM_{01} and TE_{01} (d) Anisotropic fiber condition for degeneracy ($\Delta n_{eff} (TM_{01} - TE_{01}) < 10^{-10}$) of radially and azimuthally polarized mode propagation for four different fibers (with $\rho = 0.25, 0.50, 0.75$ and $b = 4 \mu m$ as well as $\rho = 0.55$ and $b = 2.7 \mu m$) based on FEM calculation.	76
Figure 4.4	(a) Anisotropic fiber design criterion for fundamental TE_{01} and (b) TM_{01} mode.....	78
Figure 4.5	(a) Relative minimum absolute refractive index separation ($\min \Delta n_{eff}(UV_{11}^- - CV_{11}) $) between CV_{11} and unstable UV_{11} beams and (b) for different anisotropic fiber designs as done in Fig. 4.3(d)....	79
Figure 4.6	Simulated phase distribution and intensity profile of (a) UV_{+11}^- and CV_{-11}^- modes for $\rho = 0.25$ (b) 0.50 and (c) 0.75, while fiber core radius $b = 4 \mu m$ and (d) for $\rho = 0.55$ and $b = 2.7 \mu m$	80
Figure 4.7	(a) OAM charge weights of generated OAM beams ($CV_{-1,1}^-$ and $UV_{+1,1}^-$) in fiber with $\rho = 0.25$, $b = 4 \mu m$ and $\Delta_r = 0.036$, $\Delta_\phi = 0.0359$ (for design point with highest Δ_ϕ in Fig. 4.3(d)) (b) Vortex mode purity of ($UV_{+1,1}^-$, $CV_{-1,1}^-$, $CV_{-2,1}^-$ and $CV_{+2,1}^+$) for all fiber designs (red curve in Fig. 4.3(d)).....	82

Figure 4.8	(a) Effective index (n_{eff}) of EH_{11}^e and (c) HE_{31}^e modes, while (b) effective index separation (Δn_{eff}) between EH_{11}^e and EH_{11}^o , (d) between HE_{31}^e and HE_{31}^o modes84	84
Figure-A I-1	Example of an FEM simulation the generated mesh by COMSOL at different zoom scales, farthest (a) to closest (c) and (d) simulated mode field of HE_{11} guided in core for modelling annular core photonic crystal fiber96	96
Figure-A II-1	(a) Experimental setup of knife edge method for beam (OAM) size measurement (b) Variation of OAM beam size along Z (Focus) -axis.99	99
Figure-A II-2	(a) Experimental data of power obtained during knife-edge measurement for beam (OAM) size (b) numerical differentiation (data) of the power measured by the knife-edge method (c) Polynomial fitting of power measured (d) numerical differentiation of the fitted power100	100

LIST OF ABBREVIATIONS

AC-PCF	Annular core photonic crystal fiber
AFM	Atomic force microscopy
BS	Beam splitter
CCD	Charge-coupled device
CD	Chromatic dispersion
CVB	Cylindrical vector beam
EMR	Endlessly mono-radial
EDFA	Erbium doped fiber amplifiers
FEM	Finite element method
FMF	Few-mode fibers
FWHM	Full width at half maximum
GNLSE	Generalized nonlinear Schrödinger equation
GVD	Group velocity chromatic dispersion
HWP	Half wave plate
IPGIF	Inverse-parabolic graded-index fibers
LPFG	Long-period fiber grating
LP	Linear polarizer
MCF	Multi-core fibers
MDM	Mode-division multiplexing
MMF	Multi-mode fiber

MO	Microscope objective
NA	Numerical aperture
OAM	Orbital angular momentum
PDM	Polarization dependent multiplexing
PSF	Point spread function
PCF	Photonic crystal fiber
QWP	Quarter wave plate
SAM	Spin angular momentum
SCG	Supercontinuum generation
SDM	Space-division multiplexing
SEM	Scanning electron microscopy
SLM	Special light modulator
SMF	Single-mode fiber
SMPMF	Single-mode polarization-maintaining fiber
STED	Stimulated emission depletion
TM	Time multiplexing
WDM	Wavelength division multiplexing
WP	Wollaston prism
CAD	Computer-aided design

LIST OF SYMBOLS

l	Topological charge
d	Air hole diameter
Λ	Air hole pitch
N	Number of air hole ring
V	Dimensionless number (normalized frequency)
λ	Wavelength
n_{core}	Effective index core of fiber
n_{clad}	Effective index cladding of fiber
n_{FSM}	Effective index of the fundamental space-filling mode
b	Effective core radius
A_{eff}	Effective mode area
γ	Nonlinear parameter
n_2	Nonlinear refractive index
n_{eff}	Effective refractive index
Δn_{eff}	Effective refractive index difference
D	Dispersion parameter
$\beta(\omega)$	Wavenumber
ω_0	Center frequency
β_1	Group velocity
β_n	n^{th} order dispersion coefficient

$A(z,t)$	Electric field envelop
τ_{shock}	Optical nonlinear shock
$R(t)$	Nonlinear Raman response of the material
f_R	Fractional Raman contribution of silica glass material
$\delta(t)$	Dirac function
h_R	Raman response function
τ_{FWHM}	Full width half maxima of gaussian pulse
P_p	Peak power
J_ν	Bessel functions of the first kind
N_ν	Bessel functions of the second kind
f_p	Optical power fraction
S_z	Poynting vector
P_l	Normalized power weight
Δ_r	Radial refractive index contrast
Δ_ϕ	Azimuthal refractive index contract
k	Wavenumber
w_0	Beam width at the beam waist
\vec{e}_r	Radial unit vector
\vec{e}_ϕ	Azimuthal unit vector
z_R	Rayleigh range
w	Beam waist

L_p^l	Laguerre polynomial
$e(r)$	Radial electric field
$f_v(\phi)$	Azimuthal electric field
I_{max}	Maximum intensity distribution
I_{min}	Minimum intensity distribution

INTRODUCTION

Context of the research work

During the last many decades, Gaussian laser beam has been the main driving force for major scientific research done in the field of optics and photonics. In particular, most optical communication systems are operating on Gaussian-like beams, where single-mode fiber (SMF) has been flag-bearer for transmission of these beams (D. J. Richardson, 2010). Further in order to maintain the ever-increasing demand towards data hungry applications, researchers and communication engineers have been continuously exploring novel technologies to increase data transmission capabilities using SMF. Their relentless efforts have made it possible to achieve many technological breakthroughs towards increasing data transmission capabilities such as: low-loss SMF, erbium doped fiber amplifiers (EDFA) and coherent transmission (D. Richardson, Fini, & Nelson, 2013). In addition, researchers have also exploited most of data multiplexing schemes (degrees of freedom for more communication channels) starting from wavelength division multiplexing (WDM), polarization dependent multiplexing (PDM), multiplexing in time (TM), to phase multiplexing in order to enhance the data transmission capacities of optical networks (Ishio, Minowa, & Nosu, 1984; Rao, Ribeiro, Jackson, Zhang, & Bennion, 1995; Shtaif, 2008).

Yet, this exponential increase in demand for data consumption has pushed the trusty SMF to its physical limits (Essiambre & Tkach, 2012). Potentially the last remaining dimension to be explored is space (in fiber), known as spatial division multiplexing (SDM) (G. Li, Bai, Zhao, & Xia, 2014; D. Richardson et al., 2013). This can be accomplished using multi-core fibers (MCF) that contains multiple cores, however limited by modal crosstalk between guided modes in different fiber cores, hence tradeoff between maximum number of cores and low modal crosstalk is pivotal (Saitoh & Matsuo, 2013). Multi-mode (MMF) and few-mode fibers (FMF), that works on mode division multiplexing (MDM) (both fiber types have large core diameter in comparison to SMF, hence can guide multiple higher order modes) or

multimode based multicore fiber (where all fiber cores support multiple mode) are fitting prospects for spatial division multiplexing. Figure 0.1 shows the schematic representation of different multiplexing techniques.

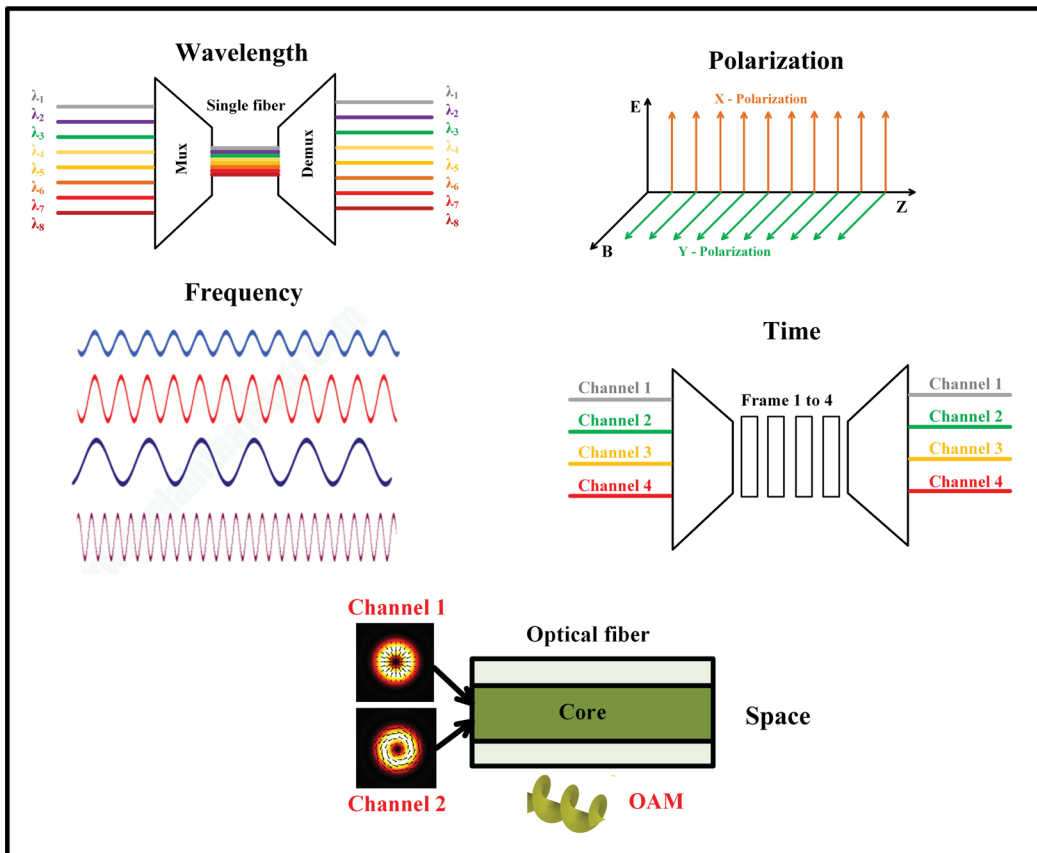


Figure 0.1 Schematic diagram of different data multiplexing techniques, including space division multiplexing a new degree of freedom for data multiplexing in future communication systems

In order to employ these higher order modes in space multiplexing one needs to gain detailed knowledge of unconventional modes. Consequently, research is widely evolving to understand different higher-order modes such as cylindrical vector beams, which demonstrate unique doughnut shaped intensity profile, thus characterized by on-axis zero intensity (dark) hole owing to polarization singularities (Zhan, 2009). All polarization states in vector beams are orthogonal to each other, therefore, provides multiple communication

channels. Another high-order beam that displays similar annular intensity profile are beams carrying orbital angular momentum (OAM), which can be formed (in fiber) by superposition of two orthogonal vector modes. These OAM beams carry both spin (i.e. circular polarization) and orbital angular momenta owing to helically varying phase front and are characterized by a topological number for each OAM state (Yao & Padgett, 2011). These infinite OAM states can in theory provide unlimited orthogonal transmission channels (Trichili, Park, Zghal, Ooi, & Alouini, 2019). In addition, such peculiar intensity distribution beams along with either angular momentum carrying ability or polarization inhomogeneity have attracted researcher towards finding new modalities in applications as: probing new (non) linear chiral light-matter interactions (Brullot, Vanbel, Swusten, & Verbiest, 2016; Forbes & Andrews, 2018), optical trapping to nanoscale imaging (M. Chen, Mazilu, Arita, Wright, & Dholakia, 2013; K. Liu et al., 2017). Another promising application of these beams can be realized in space division multiplexing where doughnut shaped intensity beams along with either theoretically infinite topological number could help in providing many communication channels (Ren et al., 2015, Bovino, Braccini, Bertolotti, & Sibilìa, 2011; R. Chen, Agarwal, Sheppard, & Chen, 2013; Padgett, 2014; Padgett & Bowman, 2011).

One such well-established application of optical vortex (OAM and CV beams) relates to stimulated emission depletion (STED) super-resolution microscopy, where two co-aligned beams (one doughnut shaped intensity beams (either phase or polarization vortex) and the other a Gaussian beam) are used together to breach the diffraction limit. Figure 0.2 shows the diagrammatic view of working principle of both common diffraction limited microscopy and STED microscopy. The conventional microscopy uses Gaussian beam that works as excitation beam shown in Fig. 0.2(a), whereas STED microscopy employs both Gaussian (excitation beam) and doughnut (depletion beam) beam to create super resolution spot, as a result breaches the diffraction limit as in Fig. 0.2(b). There are many other applications that can use both type of higher order beams as: particle manipulation, sensing, optical trapping to list a few.

However, all discussed application of these beams prominently requires stable and efficient transmission and therefore one need fiber design suitable for optical vortex. This motivates the subject of thesis, which is to explore design of novel fibers that allows stable propagation of optical vortex to exploit them in above mentioned applications.

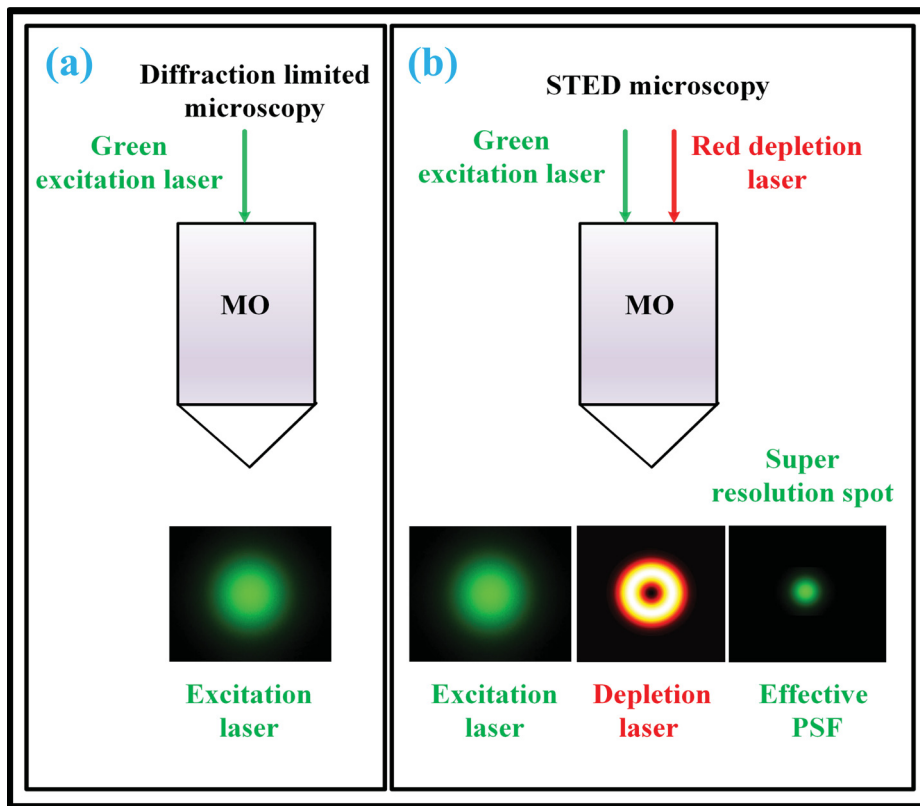


Figure 0.2 Schematic overview of working principle of STED microscopy, (a) shows the schematic of light emission from a conventional microscopy (b) schematic of a depletion laser “doughnut shape”, and effective point spread function (PSF) demonstrate super resolution spot

In addition to this, application of these optical vortex would immensely benefit from the versatility of a broadband source (Wildanger, Rittweger, Kastrup, & Hell, 2008; Yan, Kristensen, & Ramachandran, 2019). Hence, exploring fiber designs that facilitate stable

propagation as well as in-fiber supercontinuum generation of these optical vortices is the ultimate objective of thesis.

The identified research problem and their potential solutions

Intermodal crosstalk is one of the major challenges, which need considerable attention when exploring fiber design that support numerous spatial modes. Few-mode fibers are promising candidates as these fibers are generally designed for transmission of a limited number of modes (< 20), henceforth allows highly efficient transmission with low intermodal crosstalk. In particular, FMFs with ring core structure as: ring core fiber (Brunet, Vaity, Messaddeq, LaRochelle, & Rusch, 2014) and inverse-parabolic graded-index fiber (IPGIF) (Ung, Vaity, et al., 2014) designs assist in lifting intermodal effective refractive index separation, consequently, reduce intermodal crosstalk. Moreover, a fiber design that enables optimization of optical properties such as: chromatic dispersion and non-linearities, towards in-fiber supercontinuum generation of optical vortices could have potential applications in STED microscopy, biosensing and micro-manipulations: as this allows one to employ broadband of optical vortices in all discussed applications in results could facilitate investigation flexibility. A promising design solution lies in photonic crystal fiber (PCF) structure, where the fiber holey cladding structure can be engineered by modifying air hole diameter (d) and pitch (Λ) and accordingly one can tailor fiber optical properties. Hence, ring core fiber with photonic crystal cladding could be an ideal candidate to achieve desired optical properties (by engineering the photonic crystal cladding) as well as lifting intermodal effective index separation (ring-core of fiber).

In this regard, ring core photonic crystal fiber based on chalcogenide glass was initially proposed for the supercontinuum generation of optical vortex in the infrared spectrum and demonstrate promising results, however proposed fiber design is limited to numerical

simulation and lacks experimental work (Yue et al., 2012). Later numerous other ring shape fibers based on photonics crystal structure (Hu Zhang et al., 2017) were reported, details in chapter 1 of thesis. However, most reports based on ring core photonic crystal fiber are limited to theoretical work. Very few groups in the world have successfully fabricated these intricate fibers (Tandjè et al., 2019; Yue et al., 2012), and achieved limited success in OAM mode purities. Henceforth extensive research is needed to address the issue of broadband stability of vortex beams in optical fibers, which is critical to ensure higher mode purity of optical vortex upon propagation through the fibers.

The OAM beams created by combination of radial TE_{0m} and azimuthal TM_{0m} vector modes have been neglected in applications as optical communication, since these modes are generally considered to be sources of noise (due to inter-modal crosstalk), and because these modes remain non-degenerated in classical fibers, thus preventing them to form stable OAM modes. Final part of this thesis is related to detailed investigation of fiber design that enables co-propagation of all possible combination of optical vortex (which could be created by superposition of either radially / azimuthally polarized modes or hybrid HE/EH modes), a feat not conceivable in conventional step index ring core fiber or even the ring core photonic crystal fiber (as radially / azimuthally polarized modes propagate as non-degenerated modes in standard isotropic step index fiber designs). Radially anisotropic fibers present promising solution to problem as the fiber's radial anisotropy could be engineered to embolden degeneracy of radial TE_{0m} and azimuthal TM_{0m} vector modes. This fiber class has also been reported for several unique guiding characteristic as: (1) controlled selective mode excitation of the radial and azimuthal (TE_{0m} and TM_{0m}) families, (2) tailor fiber design such as azimuthal TE_{0m} or radial TM_{0m} mode becomes fundamental modes instead of HE_{11} mode (in case of conventional step index fibers).

Objective of the research

The objective of this research work is to design and characterize novel fibers towards stable transmission of OAM and CV beams, with high mode purity. The effective knowledge of fiber properties is critical for stable guidance of such complex shape beams. This could allow future researchers to explore such fibers in specific applications such as: space-division multiplexing, optical sensing, and super-resolution microscopy. Although several fiber design candidates have been theoretically proposed for the transmission of optical vortex, further widespread research is required to design and investigate fibers that allows the practical and broadband guiding of mono-radial (i.e. single doughnut-shaped) vortex beams. Other than this, stable propagation of all optical vortex formed by superposition of fiber vector modes (i.e. TE_{0m} , TM_{0m} modes or hybrid HE/EH modes), while empowering higher vortex mode purity necessitates exploration of novel fiber designs.

The main objectives of the research work shown in this thesis, which are schematically presented in Fig.0.3, are:

1. The first objective is design and simulate a novel fiber toward stable transmission and supercontinuum generation of optical vortex which preserve better mode purity, thus effectively designed fiber should be able to minimize intermodal coupling as well as permits optimization in optical nonlinearities and chromatic dispersion.
2. Second objective is to fabricate and experimentally characterize the proposed fiber design. This characterization is essential in order to identify experimental limitations and shortcoming in fiber fabrication. It helps in exploiting such fiber to its maximum potential, particularly for application related to OAM and CV beams.
3. The final objective is to design and engineer a radially anisotropic ring fiber, that enables co-propagation of all types of optical vortex (created by superposition of either azimuthal (TE_{0m}) / radial (TM_{0m}) modes or hybrid HE/EH modes, while maintaining higher mode

purity. This kind of fiber has the potential to enable communication engineers to use the previously discarded TE/TM vector modes into creating OAM states for SDM.

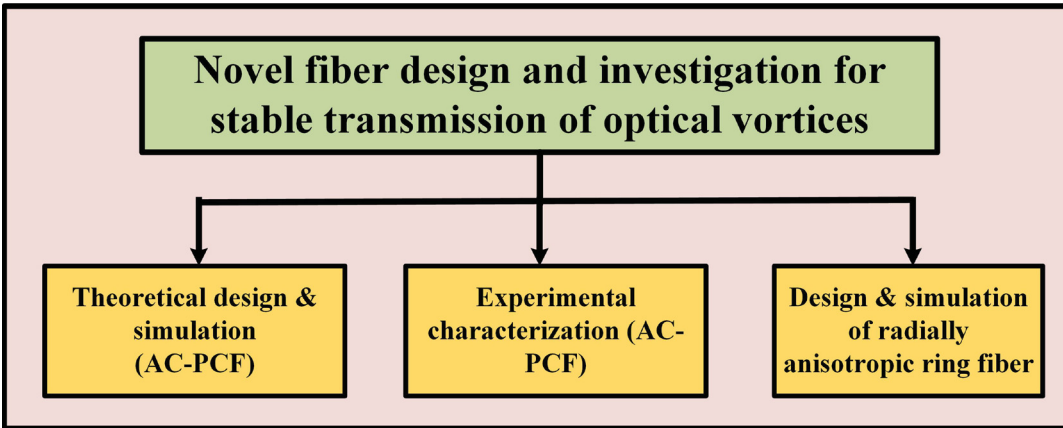


Figure 0.3 Schematic outline of the overall thesis work

The main part of this research work is taken as an original research article-based thesis, as mentioned in the submission policies of ETS. While accomplishing my research objective, I have contributed to the publication of 4 peer-reviewed journal papers (published/submitted), where being part as first author of 3 articles and co-author for other 1 article. The three first author articles correspond to the three chapters (2, 3 & 4) of this thesis. These chapters constitute an abstract, introduction, theoretical & experimental methods employed in fiber design and characterization followed by the results and discussion. The principal content of the thesis consists of abstract, introduction with research objectives, literature review, conclusion, and statement of original contribution with future recommendations.

Thesis outline

The thesis has been structured as follows:

The first chapter of this thesis contains no original contribution but gives information (introduction) about different techniques and concepts needed later in this thesis. The chapter

starts with introduction of OAM and CV beams, while stating their importance in several promising applications. It is followed by literature reviews of different optical fiber design candidates that have been proposed for transmission of these beams. The following chapter presents the design and characterization of fibers for achieving objectives of the proposed research, which results to journal publications.

The second chapter is an article published in *Scientific Reports* in 2019, followed by a conference presentation at *Photonics North 2018*, Montreal Canada:

In this work, a novel endlessly mono-radial annular core photonic crystal fiber (AC-PCF) design is demonstrated, which supports a unique waveguiding regime make it an ideal medium to study mono-annular beams, namely cylindrical vector beams and orbital angular momentum beams, within a linear or nonlinear broadband regime irrespective of operational wavelength. In particular, it is demonstrated through numerical solutions that precisely optimized design of the endlessly mono-radial AC-PCF can support the supercontinuum generation of stable optical vortex beams. The proposed fiber design has potential applications in space-division multiplexing, and optical sensing via structured light and super-resolution microscopy.

The third chapter is an article published in *Fibers*, MDPI Journal in 2020, also presented in *Cleo 2020* and *OSA Advanced Photonic Congress 2020*, Montreal:

This article demonstrates experimental characterization of annular core photonic crystal fiber proposed in chapter 2. The fiber design for broadband single-radial order guidance was fabricated, which is characterized for stable propagation of OAM and CV beams. The characterization experiment shows that fiber can maintain higher mode purity (above 18 dB) of vector and vortex beams (generated in free space using tunable laser and spiral plate) after propagation in the fiber under test over the wavelength range from 805 to 845 nm. This work is one more step towards the stable and broadband transmission of vector as well as vortex beams in photonic crystal fibers, and especially, in designs identical to AC-PCF.

The fourth chapter of this thesis is an article Published in *OSA Continuum*:

In this article, radially anisotropic ring-core fiber is designed and simulated for novel transmission of optical vortex, demonstrating unique properties. The simulation results demonstrated the parametric conditions where the fiber supports *modal replacement* i.e: the doughnut-shaped radial TM_{01} or azimuthal TE_{01} mode replaces the Gaussian-like HE_{11} mode as the fundamental mode of the fiber. In addition to this, we demonstrate that a small radial birefringence ($\sim 10^{-4}$) could significantly engineer the waveguiding properties of ring-core fiber, such that non-degenerate TE_{0m} and TM_{0m} modes, becomes degenerate. In result it allows co-propagation of high purity optical vortex, created by either superposition of TE_{0m} , TM_{0m} modes or hybrid HE/EH modes, an accomplishment not feasible with standard few-mode fibers using isotropic or linear birefringent materials.

CHAPTER 1

LITERATURE REVIEW AND BACKGROUND INFORMATION

1.1 Cylindrical vector beams

The cylindrical vector beams are vector wave solutions of Maxwell's equations that demonstrate axial symmetry in amplitude and phase. These beams are characterized by doughnut shape intensity profile and possess zero intensity center as the polarization state of these beams is undetermined (also recognized as polarization vortices) at beam center ($r = 0$). These beams have the space varying states of polarizations, for example radial (TM_{01}) and azimuthal (TE_{01}) (Zhan, 2009).

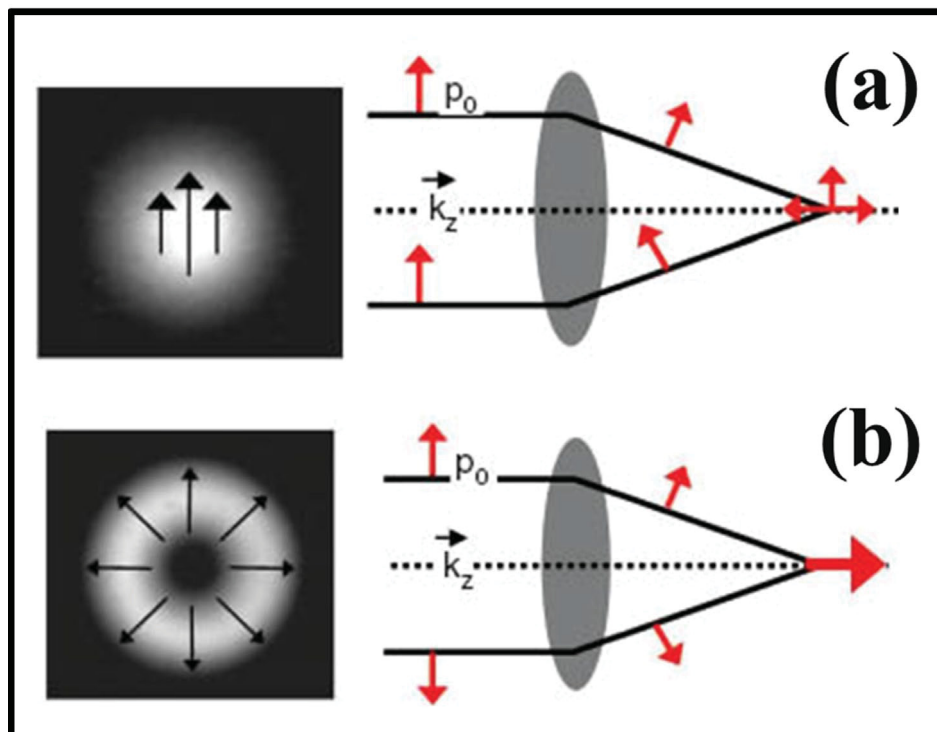


Figure 1.1 Focusing properties with high-NA lenses for different beam shapes; (a) Gaussian beam results in complex polarization, while (b) a radially polarized beam yields an intense, well-defined electric field along the optic axis

Taken from Siddharth Ramachandran & Kristensen (2013)

The difference between polarization vortices and plane polarized Gaussian beam can be visualized when these beams are focused using high numerical aperture lens (Siddharth Ramachandran & Kristensen, 2013). When focused, different spatial segments of radially polarized light create constructive interference, hence forming unique light distribution (Youngworth & Brown, 2000), in contrast to plane polarized Gaussian beam as in Fig. 1.1.

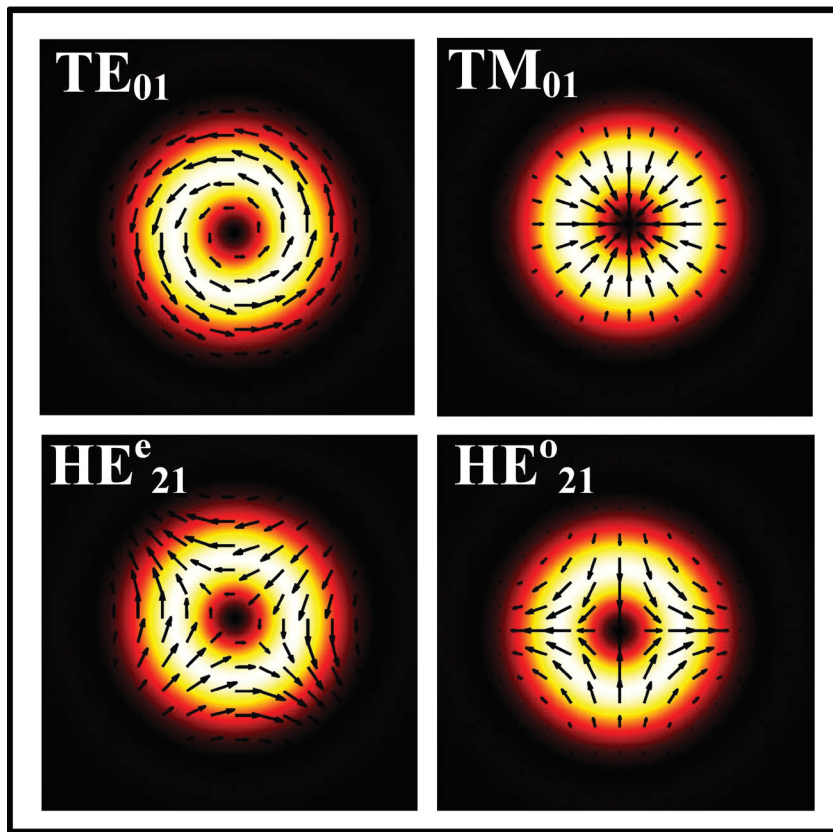


Figure 1.2 Intensity distribution of cylindrical vector beams: TE_{01} , TM_{01} , HE_{21}^e , and HE_{21}^o , the arrows depict polarization orientations

The cylindrical vector beams mathematically can be represented as the solution of wave equation as:

$$(\nabla^2 + k^2)E = 0 \quad (1.1)$$

here, $k = 2\pi/\lambda$ is wavenumber

The two conventional CVBs can be expressed as azimuthally and radially polarized vector Bessel-Gaussian beams, in the paraxial approximation and using cylindrical coordinates:

$$\vec{E}(r, z) = E_0 \frac{r}{w_0} e^{\frac{r^2}{w_0^2}} e^{i(\omega t - kz)} \vec{e}_i, \quad \vec{e}_i = (\vec{e}_r, \vec{e}_\phi) \quad (1.2)$$

Where E_0 is constant electric field amplitude, r and ϕ are the radial and azimuthal coordinates respectively, w_0 is the beam width at the beam waist, \vec{e}_r , \vec{e}_ϕ are unit vectors radial and azimuthal in directions. Here, general CVBs can be considered as linear combination of radial and azimuthal CVBs. Figure 1.2 displays the intensity distribution of cylindrical vector beams TE_{01} , TM_{01} , HE_{21}^e , and HE_{21}^o .

1.1.1 Generation of cylindrical vector beams

CVBs can be generated by using various methods developed since 1972 (Mushiakhe, Matsumura, & Nakajima, 1972; Pohl, 1972), both active and passive techniques depending on whether it involves amplifying media. Generally, active methods make use of laser intracavity devices that induce oscillation of laser to CV modes. These intracavity devices axial (dichroic or birefringent) components are employed to distinguish CV modes from the fundamental mode (Bisson, Li, Ueda, & Senatsky, 2006; Kozawa & Sato, 2005).

The passive methods are also used to generate CV beams both in free space and in-fiber, where linear and circular polarized Gaussian beams are generally converted (known as spatially homogeneous polarizations) into CV beams (spatially heterogeneous polarizations). The radial analyzer (birefringent or dichroic radial analyzer) owing to their specially varying polarization properties enable them to convert a circularly polarized beam into a radially or azimuthally polarized beams and the beam type depends on input beam polarization orientation (Yi et al., 2014). Similarly, spiral phase element (SPE) created using spatial light modulator (SLM) or space variant polarization rotation (Levy, Tsai, Pang, & Fainman, 2004;

Rosales-Guzmán, Bhebhe, & Forbes, 2017; Saripalli, Ghosh, Apurv Chaitanya, & Samanta, 2019) can be used to convert linear or circular polarized light into CV beams.

Another passive generation technique depends on fiber-based mode conversion methods. The few mode fibers are known to guide higher order modes as: TE_{01} (azimuthally polarized) and TM_{01} (radially polarized) annular modes. These vector modes can be easily excited in few mode fibers, when the fundamental mode from SMF couple to a vector mode of a few mode fiber with careful core misalignment, although conversion efficiency remains low as power is generally distributed amongst various undesired higher order modes. Another more reliable method for CV beam generation in fiber, works on mode converter using fiber gratings such as permanent or temporary long-period fiber gratings (LPFGs) written using electric arc discharges or a mechanical grating. The symmetrically fabricated grating in few-mode fiber (with defined constant pitch across grating length) allows light coupling from fundamental mode to forward propagating higher order modes.

The mode purity and conversion efficiency of CV beams depends on polarization orientation of fundamental HE_{11} mode, and mode excitation can be controlled by controlling polarization of HE_{11} input mode in fiber before grating location. In this regard, an extensive research is performed by Ramachandran *et al.*, (Siddharth Ramachandran, Wang, & Yan, 2002) where they reported the conversion of linearly polarized mode into CV beams (TE_{01} , TM_{01} , HE_{21}^e , and HE_{21}^o) with more than 99% conversion efficiency (Siddharth Ramachandran & Kristensen, 2013; Siddharth Ramachandran, Kristensen, & Yan, 2009).

Recently, Yimin, Zhang, *et al.* has demonstrated the mode conversion of linearly polarized HE_{11} mode to TE_{01} and TM_{01} modes (coupling ratios more than 15 dB) with single-mode polarization-maintaining fiber (SMPMF) and 10-meter-long ring-core fiber, using two vector-mode coupling LPFGs. The mode purity was 92.4% for TE_{01} and 97.3% for TM_{01} modes (Yimin et al., 2020). Mode purity was estimated by fraction content of vector (TE_{01} and TM_{01}) modes obtained versus LP_{01} mode, which was done by scanning one-dimensional intensity distribution across the center of beam and then estimating power ratio

of vector mode to LP_{01} mode. Figure 1.3 shows the schematic of experimental set-up and obtained transmission spectra of LPFG.

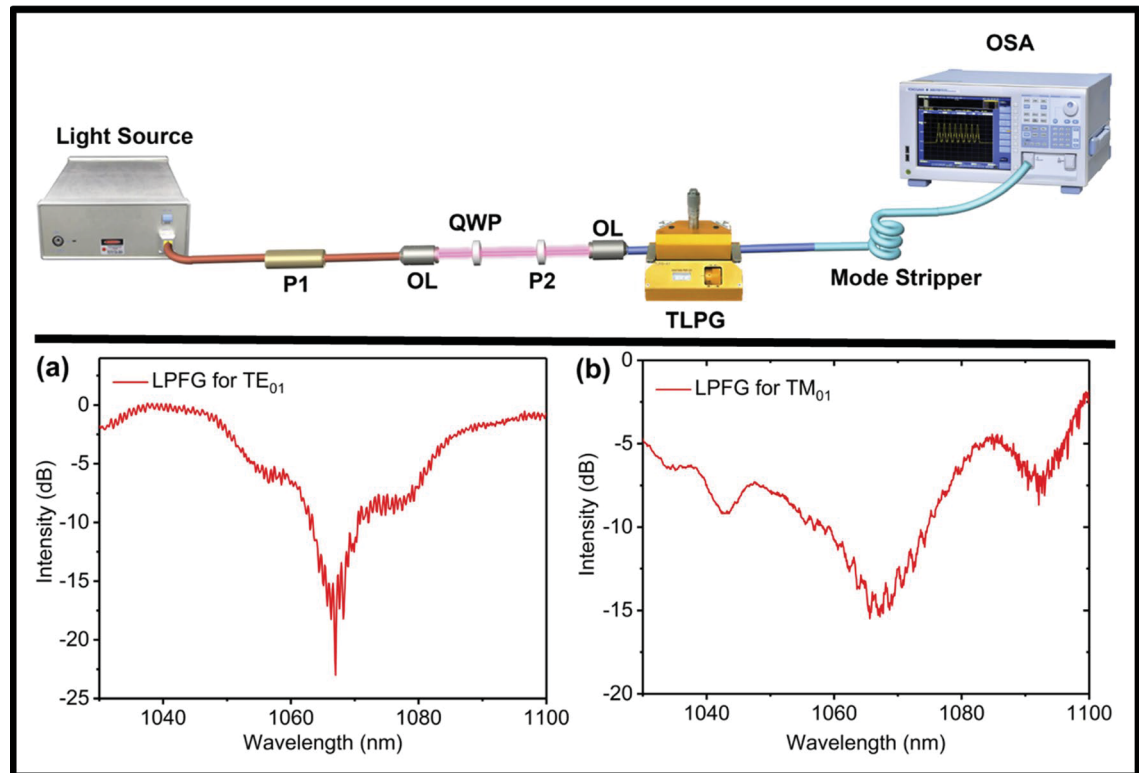


Figure 1.3 Experimental setup for measuring the polarization dependence of LPFG (top), the transmission spectra of LPFGs (bottom)
Adapted from Yimin et al. (2020)

1.1.2 Applications of cylindrical vector beams

The CV beams have been gaining lot of interest lately, owing to unique focusing properties under high numerical aperture (NA) condition. Particularly, radially polarized beams can be focused into a tighter spot due to strong and localized longitudinal component in comparison to linearly polarized or circularly polarized conventional beam. This unique characteristic is vital in optical imaging and manipulation (R. Chen *et al.*, 2013; Kozawa & Sato, 2010). Apart from this, unique vectorial electric field distribution (single doughnut shaped) has many promising applications such as: optical trapping (Kozawa & Sato, 2010), laser

machining (Duocastella & Arnold, 2012), fiber-optic sensing, light-matter interactions (M. Li et al., 2019) space division multiplexing (Qiao *et al.*, 2017) and many more.

1.2 Orbital angular momentum beams

Orbital angular momentum beam are optical vortices that exhibit an annular intensity profile (identical to cylindrical vector beams) characterized by a null intensity center created by a phase singularity. When propagating in optical fibers, the OAM beams are known to carry both spin and orbital angular momentum. The light carries spin angular momentum (SAM) in either circularly or elliptically polarized orientation, i.e., transverse electric field rotates around its axis. Similarly, it can carry orbital angular momentum when phase front of light rotates about its axis, which does not depend on state of polarization. Therefore, circular, or elliptically polarized light that possess helical phase front, can carry both type of angular momentums. In analytic expression, this helical phase front is generally related to a phase term of $\exp(\pm il\theta)$ in the transverse plane, where θ is the azimuthal coordinate and l is an integer number of tangled helices or OAM order. The handedness (i.e. sign) of the helix corresponds to the (counter-)clockwise orientation of the phase corkscrew upon propagation.

In 1992 Allen *et al.* demonstrated that helically phased beam carries an OAM corresponding to $l\hbar$ per photon (Allen, Beijersbergen, Spreeuw, & Woerdman, 1992). Moreover, this OAM values increases with increasing l value and thus can attain higher momentum than SAM.

A Laguerre-Gaussian beam with the helical phase term $\exp(il\phi)$ as shown below can be represented as mathematical solution for OAM beams in cylindrical coordinates system:

$$E(r, \phi, z) = E_0 \left(\left(\sqrt{2} \frac{r}{\omega(z)} \right)^l \right) L_p^l \left(2 \frac{r^2}{\omega(z)^2} \right) \cdot e^{\left(\frac{-r^2}{\omega(z)^2} - \frac{-ikr^2z}{2(z^2+z_R^2)} \right)} \cdot e^{i(2p+l+1) \cdot \arctan\left(\frac{z}{z_R}\right)} \cdot e^{\pm il\phi}$$

(1.3)

Where, z_R is the Rayleigh range, w is beam waist, L_p^l is Laguerre polynomial and $p + 1$ is the number of annular rings. Figure 1.4 displays the phase and intensity profile of Gaussian beam ($l = 0$) and OAM beams with $l = +1$ and $+2$. The intensity profiles of OAM beams show the dark central hole size increases with increasing phase singularities (Willner et al., 2016).

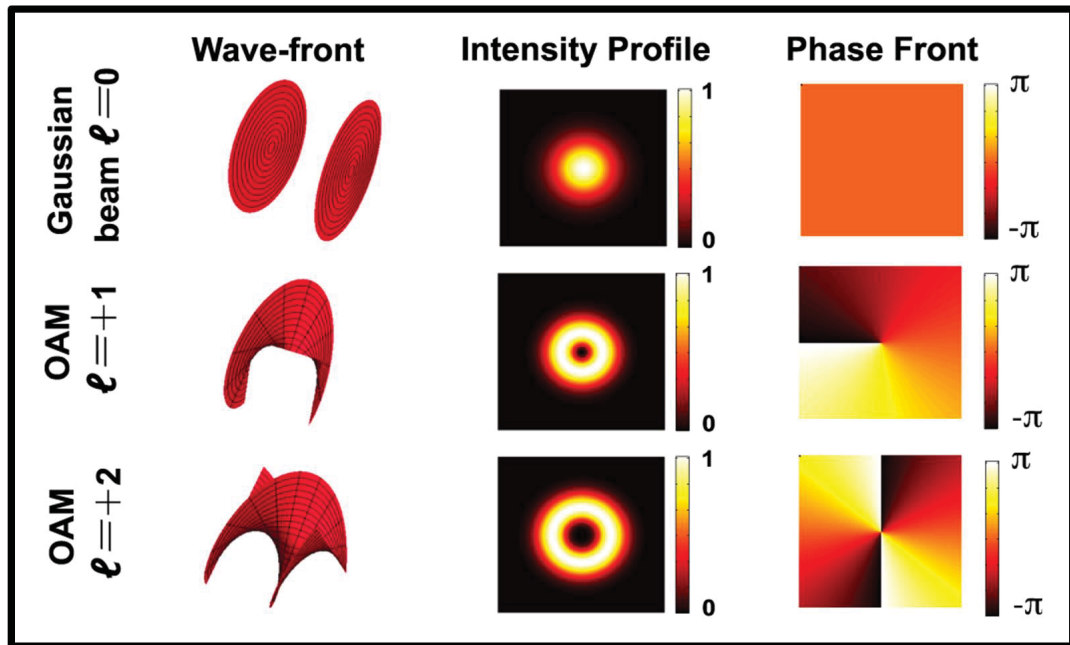


Figure 1.4 The intensity profile and phase information of regular Gaussian beam ($l = 0$) and OAM beams ($l = +1$) and ($l = +2$)
Taken from Willner et al. (2016)

1.2.1 Generation of orbital angular momentum beams

OAM beams can be generated using well know generation techniques. Perhaps most typical of them is using spiral phase plate (an optical component with helical surface), where the thickness of optical component changes with variation in azimuthal orientation with relation as: $\frac{l\lambda\phi}{2\pi(n-1)}$, here n is refractive index of material used, λ is wavelength of operation, ϕ is azimuthal coordinate. When the plane wave is incident on a spiral phase plate, it gets converted into a helical phase beam. This device is very simple and efficient toward high purity beam conversion. Although, one needs different phase plate (high precision) for every

order of OAM beam generation, thus it needs very high cost in production of different phase plates. Figure 1.5 shows schematic diagram of spiral phase plate that can generate helical phase beam as in Fig.1.5 (Yao & Padgett, 2011).

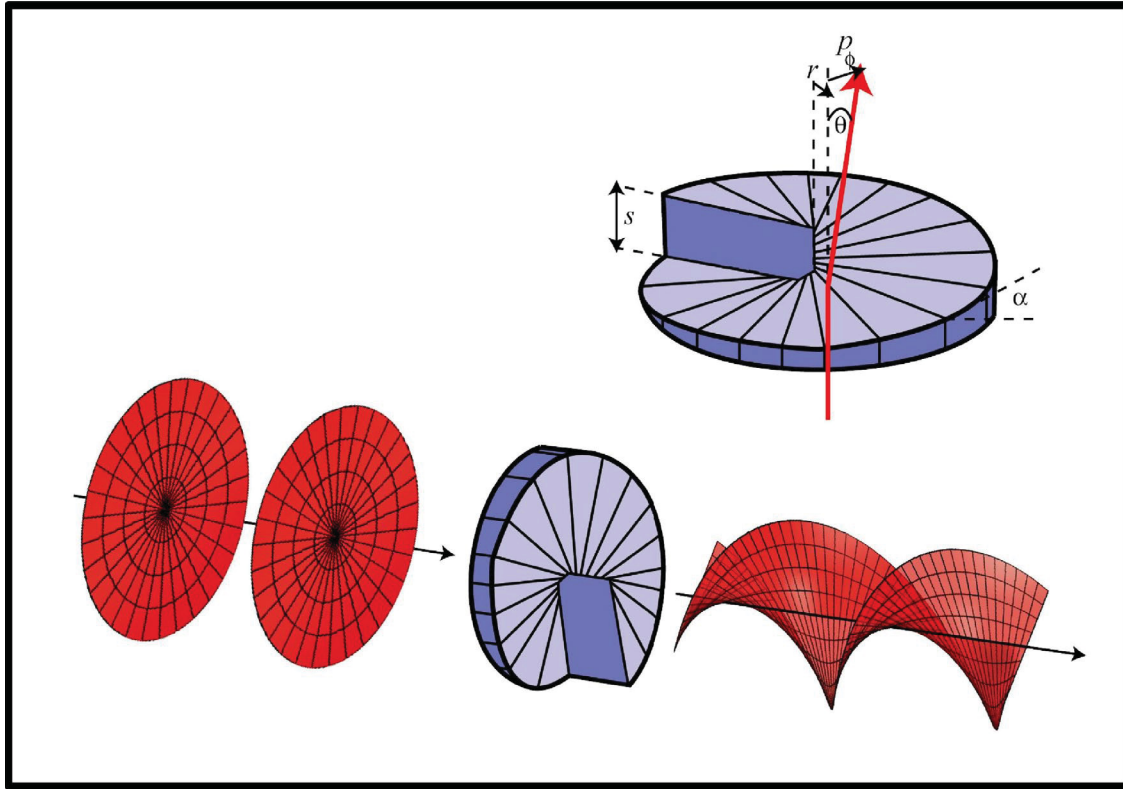


Figure 1.5 A spiral phase plate can generate a helically phased beam from a Gaussian. In this case $\ell=0 \rightarrow \ell=2$

Taken from Yao & Padgett (2011)

OAM can be created by diffraction optical elements generated by computer-generated holographic technique. One general method is to create fork grating by etching or printing on transparent material. In addition to this, two different fork grating could be superimposed to create multiple topological charges. Although, the passive nature and poor efficiency of these elements have made them less suitable for current needs (Gibson et al., 2004). However, same computer-generated holograms when employed on a digitally-addressable spatial light modulator (SLM) for creating gray fork image is a very flexible approach for generating OAM beams of any desired topological charge.

An SLM is a liquid crystals device, which is programmable using interface to the computer. It contains matrix of pixels that can be programmed to generate different fork patterns (by superposition of linear phase ramp on helical phase mask) as required for each given phase (Lazarev, Hermerschmidt, Krüger, & Osten, 2012).

The SLM works in both reflection and transmission modes. The most important thing about SLM is its versatility; one can either program it to create OAM phase mask or diffractive pattern. Figure 1.6 shows the schematic of three different OAM generation techniques using: (a) spiral phase plate, phase hologram with (b) spiral phase pattern and (c) “fork” pattern.

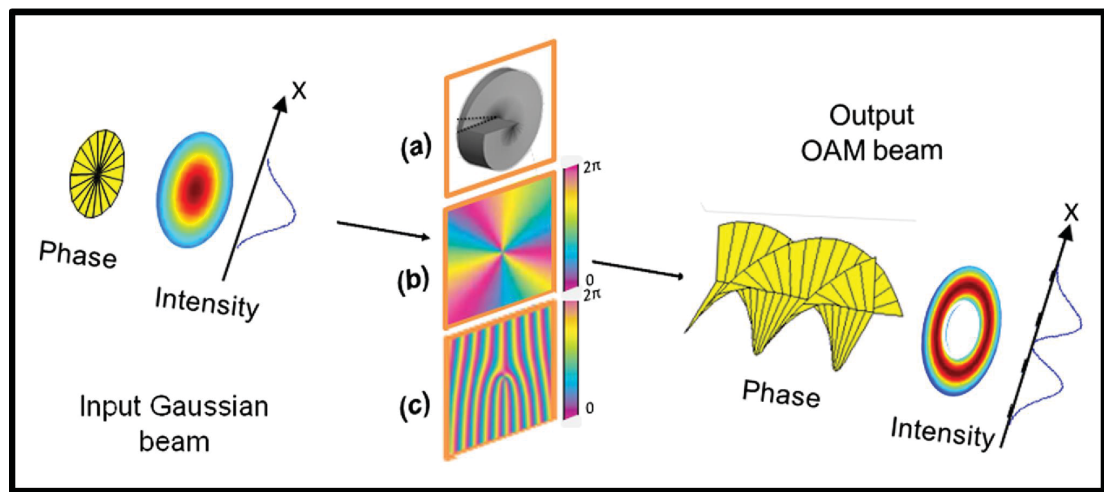


Figure 1.6 Three approaches to convert a Gaussian beam into an OAM beam: (a) a spiral phase plate, (b) a phase hologram with a spiral phase pattern, or (c) a phase hologram with a “fork” pattern. In this example, the conversion to an OAM beam with $\ell=+3$ is depicted, Taken from Willner et al. (2015)

Other than this, there are other many techniques, which can be used for generation of OAM beams such as: meta-materials (Karimi et al., 2014; Zeng *et al.*, 2013) and q -plates (Marrucci *et al.*, 2011; Rubano, Cardano, Piccirillo, & Marrucci, 2019; Yan *et al.*, 2015) . OAM beam can also be generated in optical fiber using mode convertor (Witkowska, Leon-Saval, Pham, & Birks, 2008), mode couplers (Kumar *et al.*, 2008) and different grating techniques (W. Zhang *et al.*, 2016; H. Zhao, Wang, Yamakawa, & Li, 2019; Y. Zhao *et al.*, 2017).

1.3 OAM and CV beams in optical fibers

In circularly symmetric optical fibers, the vector electric field equations can be written (in cylindrical coordinate system) as:

$$\vec{E}(r, \phi, z, t) = e(r) f_v(\phi) e^{(j\beta z - j\omega t)} \quad (1.4)$$

Where, $e(r)$ and $f_v(\phi)$ are radially and azimuthally dependent electric field components, respectively, v is a non-negative integer, β is the propagation constant and $E(r, \phi, z, t)$ is electric field envelop. Here $f_v(\phi)$ azimuthal field component is assigned by sin or cos function for even and odd modes, due to the circular symmetry of optical fiber thus the field repeat after 2π azimuthal rotation. This electric field equation can represent combination of cylindrical vector modes inside circular fiber ($TE_{01}, TM_{01}, HE_{21}^e$, and HE_{21}^o).

Further, combination of orthogonal vector modes (even and odd) with $\pi/2$ phase shift can represent OAM beam inside optical fiber, addition of even and odd vector mode components of the electric field can be written as:

$$\begin{aligned} E(r, \phi, z, t) &= e(r) \{ \sin(v\phi) \pm j \cos(v\phi) \} e^{(j\beta z - j\omega t)} \\ &\text{or} \\ E(r, \phi, z, t) &= e(r) \{ \cos(v\phi) \pm j \sin(v\phi) \} e^{(j\beta z - j\omega t)} \end{aligned} \quad (1.5)$$

These equations can also be written as:

$$E(r, \phi, z, t) = e(r) \times e^{(\pm jv\phi)} \times e^{(j\beta z - j\omega t)} \quad (1.6)$$

The above equation demonstrates similar azimuthal dependence of phase front of beam as: $\exp(il\phi)$, where v represents total angular (both spin and orbital) momentum, thus vector modes (even and odd) with $\pi/2$ phase shift give OAM beam as indicated previously.

The OAM and degenerate (same propagation constant) high-order hybrid modes relation can be encapsulated as:

$$OAM_{\pm l, m}^{\pm} = HE_{l+1, m}^e \mp iHE_{l+1, m}^o \quad (1.7a)$$

$$OAM_{\pm l, m}^{\mp} = EH_{l-1, m}^e \mp iEH_{l-1, m}^o \quad (1.7b)$$

Where sign convention (\pm or \mp) in superscript signifies orientation of circular polarization and l represents the OAM order (Dashti, Alhassen, & Lee, 2006). This displays that OAM formed by combination of $HE_{l, m}$ modes have opposite spin orientation to rotation direction and OAM formed by $EH_{l, m}$ modes have same spin and orbital orientation.

Similarly, OAM beams formed by combination of TE_{0m} and TM_{0m} modes can be represented as:

$$OAM_{\pm l, m}^{\mp} = TM_{0, m} \mp iTE_{0, m} \quad (1.8)$$

However, OAM beams created by superposition of TE_{0m} and TM_{0m} modes are not stable in fiber as these modes are non-degenerated (different β value), hence know as unstable optical vortex. Figure 1.7 show intensity distribution and phase profile of OAM ($l = \pm 1$) formed by combination of $TE_{0,1} + i TM_{0,1}$ and $HE_{2,1}^e + i HE_{2,1}^o$.

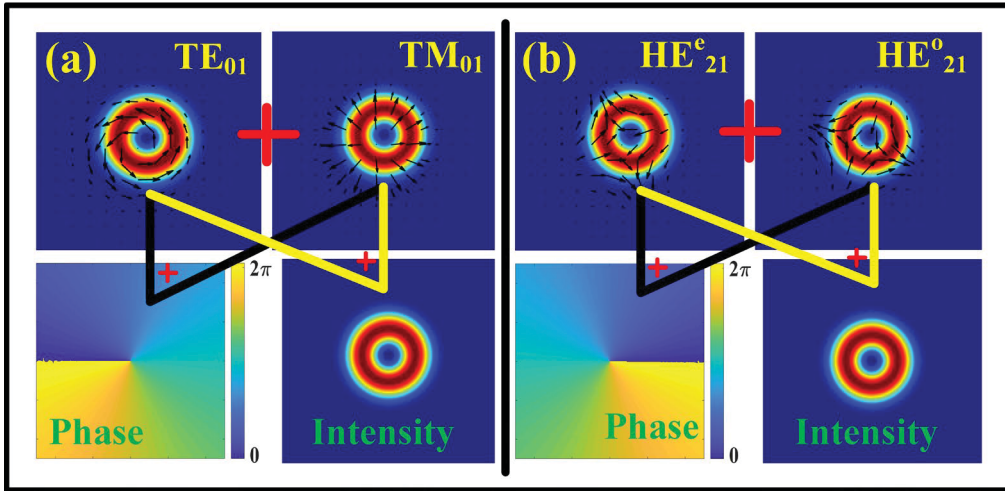


Figure 1.7 Phase and intensity profiles of OAM ($l = \pm 1$) formed by combination of (a) $TE_{0,1} + i TM_{0,1}$ and (b) $HE_{2,1}^e + i HE_{2,1}^o$ modes

Similar phase and intensity images can be obtained for other OAM beam by combination of higher order vector beams.

1.3.1 OAM and CV beams propagation in optical fibers

At the initial stage of research optical fiber were mostly used for generation and transformation of OAM or CV beams (Hwang, Yun, & Kim, 1999; Volpe & Petrov, 2004), except for one study discussing possibilities of OAM transmission through optical fiber was reported by Alexeyev *et al.* in 1998 (Alexeyev, Fadeyeva, Volyar, & Soskin, 1998). Ramachandran *et al.* in 2009 first demonstrated the transmission of CV beams in fiber lengths exceeding 20 m (Siddharth Ramachandran *et al.*, 2009), while maintaining mode stability, even in the presence of micro bend (5 mm radius). The author designs a special fiber names as vortex fiber. The fiber design had two core regions, where step-index central core (to guide conventional Gaussian beam) was surrounded by annular high-index rings (support doughnut shaped beams). Later, transmission of OAM beam was reported for more than 1 km length (Bozinovic, Kristensen, & Ramachandran, 2011; Bozinovic, Ramachandran, Brodsky, & Kristensen, 2011).

To guide OAM or CV beam in optical fiber while maintaining higher mode purity requires special fiber design that could increase refractive index contrast between co-propagating vector modes, hence minimize intermodal crosstalk. A fiber design with an annular shaped core (ring core with higher refractive index than cladding and air hole) identical to intensity profiles of OAM or CV beams is reported to lift intermodal effective refractive index separation. Thus, fibers that possess annular core refractive index profile have gain a lot of attention, a fiber with ring core and central air hole was reported in (Golowich, Kristensen, Bozinovic, Gregg, & Ramachandran, 2012). Same fiber design was fabricated and later reported for transmission of 2 OAM states over 1 km (Gregg *et al.*, 2013). Moreover, same group demonstrated that higher order OAM modes are more stable while propagating in fiber (Gregg, Kristensen, & Ramachandran, 2015).

Similar other fibers with annular core refractive index profiles were reported in recent years such as: inverse parabolic graded index fiber for transmission of CV and OAM beams (Ung, Vaity, *et al.*, 2014; Ung, Wang, *et al.*, 2014), other ring core fibers that study OAM guidance (Brunet *et al.*, 2015; Brunet, Vaity, *et al.*, 2014). Figure 1.8 shows schematic image of refractive index profile of ring core fiber (Brunet *et al.*, 2015), where a and b denote the inner and outer ring radii, while n_1 and n_2 are the refractive indices of core and cladding materials, correspondingly. The authors report five different fiber designs and perform theoretical modeling to select two fiber design for fabrication. The fabricated fibers were then characterised for transmission of OAM beams that presents promising results. However, ring shaped OAM fibers are limited in terms of parameters flexibility and in result no ideal for parametric optimization such that in order to prevent higher radial order modes (more than one rings intensity) one need to limit fiber ring thickness and consequently thin ring hinders possibility of transmission of higher number of OAM beam (with single ring) while still keeping high mode purity.

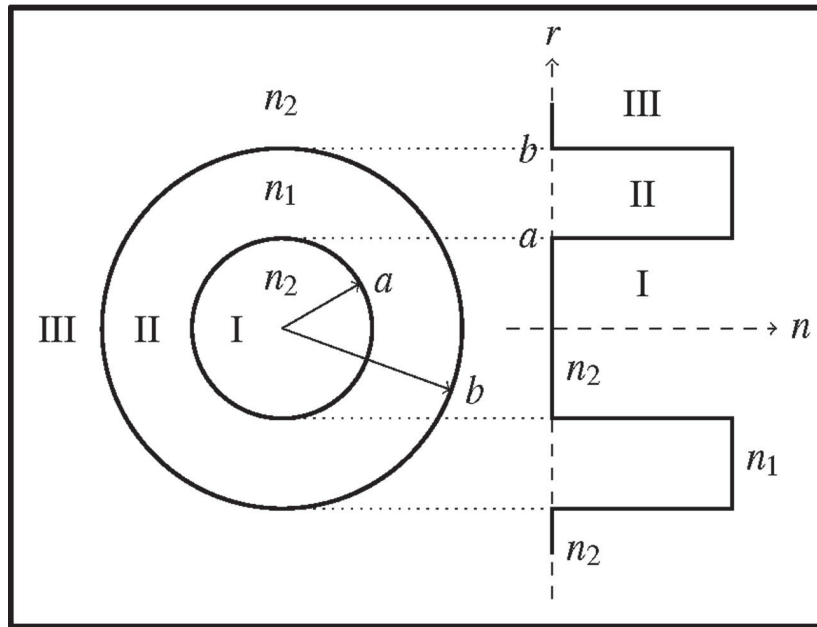


Figure 1.8 Annular fiber geometry (top view, and profile)
Adapted from Brunet *et al.* (2015)

1.3.2 Photonic crystal fibers

The photonic crystal fiber (PCF) structure offers the freedom to engineer parameters (owing to their tunable cladding structure, formed by symmetric array of air holes) such that it is possible to control fiber properties as: flatten chromatic dispersion (CD), tailored nonlinearities (Dudley, Genty, & Coen, 2006) and endlessly single-mode guiding (Birks, Knight, & Russell, 1997). Driven by these attributes, PCFs have recently been adopted for the transmission of OAM beams. The evident benefit of PCFs over the ring-core OAM fibers lies in more adjustable parameter optimization to confirm good OAM mode quality. Another virtue of PCF based OAM fiber is that it is possible to achieve higher refractive index contrast between fiber core and cladding without need for up-doping. Finally, OAM fiber based on PCF structure could offer possibilities toward supercontinuum generation of OAM beam using fiber nonlinearities.

The first study using PCF structure for propagation of OAM modes was a ring core chalcogenide glass photonic crystal fiber design. The proposed fiber design supported 2 OAM modes and author demonstrated promising numerical results of supercontinuum generation of OAM beams in the infrared. However, fiber design demonstrates low mode quality and higher confinement loss (Yue *et al.*, 2012). Another helically twisted PCF with hexagonal lattice of air holes as cladding is surround by glass core. This fiber type possesses continuous twist along propagation axis of fiber, in order to mimic, helical twist in OAM beam (Wong *et al.*, 2012). Although, this fiber only supports single OAM state and demonstrate high losses. The OAM mode number in helically twisted PCF can be increased by increasing index contract between ring core and cladding, however at cost of losing higher order modes (Ye *et al.*, 2016). Lately, circular symmetry ring shaped PCF design has been proposed to support a higher number of OAM modes with good quality. Circular PCF supports high quality OAM beams as well as provide flexibility to tune optical properties as: low loss, flat chromatic dispersion and low nonlinear coefficient ideal for optical communication (Hu *et al.*, 2016; Kabir, Hassan, Hossain, Paul, & Ahmed, 2020; Hu Zhang *et al.*, 2017; L. Zhang *et al.*, 2018), although most of these proposed design remains limited to theoretical studies and very few studies successfully fabricated and experimentally investigated such fiber designs (Tandjè *et al.*, 2019), albeit with limited mode quality. Figure 1.9 shows the cross-section of (a) ring photonic crystal fiber, (b) the twisted air-core PCF and (c) circular photonic crystal fiber details found in (Hu Zhang *et al.*, 2017).

We have also designed similar ring core photonic crystal fiber towards stable optical communication and supercontinuum generation of OAM and CV beams (Sharma *et al.*, 2020; Sharma, Pradhan, & Ung, 2019a) and further details of fiber design and characterization have been discussed in Chapter 2 and 3.

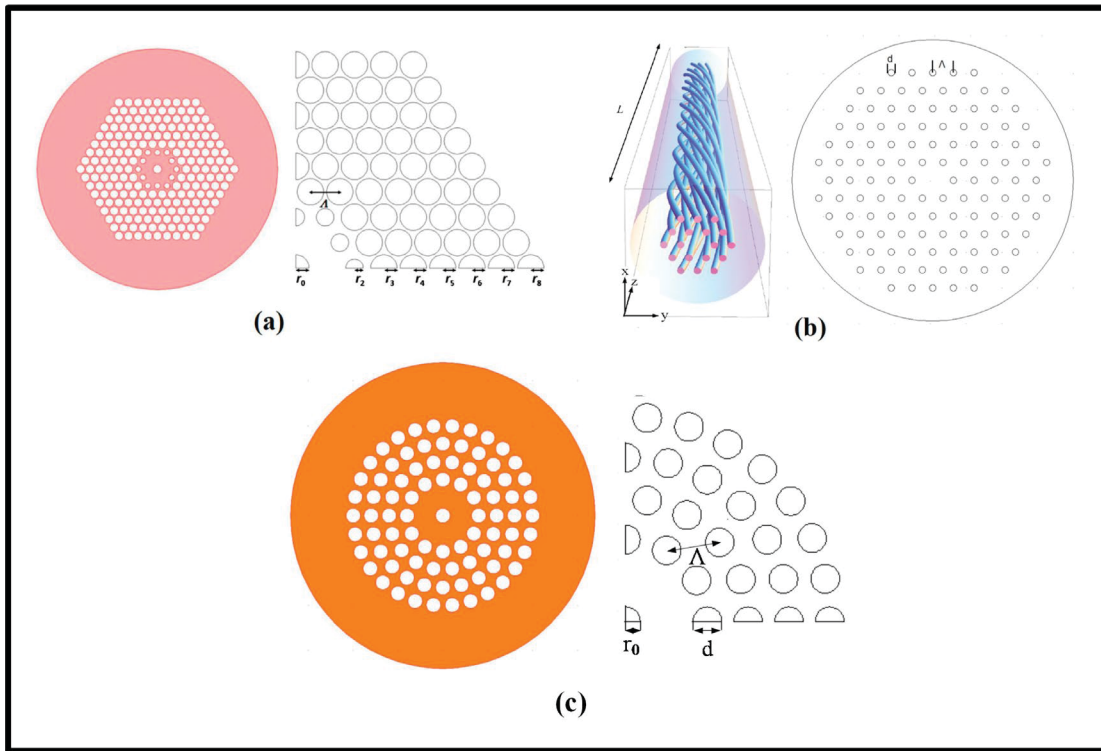


Figure 1.9 Cross section and structure parameters of (a) ring photonic crystal fiber (PCF) (b) the twisted air-core PCF (c) Cross-section and main parameters of C-PCF
Adapted from Hu Zhang et al. (2017)

1.3.3 Radially anisotropic fibers

Radially anisotropic fiber is new class of optical fiber with radial birefringence (birefringence in polar coordinates) and was first proposed by Black *et al.* in 1985. The research demonstrated in theoretical analysis that, in such anisotropic fiber, radial (TM_{01}) and azimuthal (TE_{01}) vector mode becomes fundamental mode in place of linearly polarized HE_{11} mode. This was latter followed by similar investigation of radially anisotropic fiber, where either core or cladding of fiber demonstrates polar birefringence (T.-J. Chen & Chen, 1995; Y. Chen, 1991; Yijiang, 1987). Figure 1.10 shows the schematic diagram of anisotropic fiber where fiber ring core have different refractive index profile in radial and azimuthal orientation, while cladding remain identical for all coordinates.

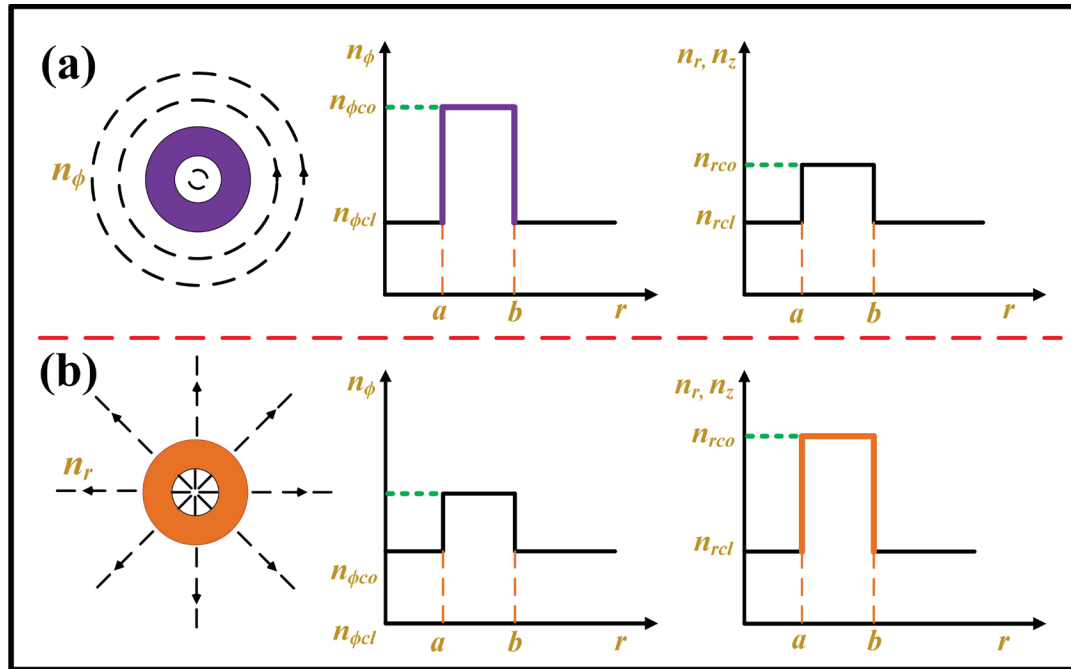


Figure 1.10 Schematic diagram of radially anisotropic ring-core fiber with refractive index profiles shown along the radial and azimuthal axes (n_r & n_ϕ)

This type of anisotropy also offers control in mode selection or mode separation of the azimuthal and radially polarized modes in optical fibers (S. H. Chen & Chen, 1994). Although experimental realization of such fiber designs is limited to liquid crystal structures and therefore limited in most applications (Ertman, Rutkowska, & Woliński, 2018), however recently proposed metamaterial based optical fibers could provide desire stimuli toward further research (Pollock, Iyer, Pratap, & Anantha Ramakrishna, 2016; Pratap, Bhardwaj, & Ramakrishna, 2018; Pratap, Ramakrishna, Pollock, & Iyer, 2015).

We have performed an extensive numerical investigation in relation to attain fiber design (parameter) optimization and details of this work are given in chapter 4 of this thesis. This study reveals several anisotropic fiber design candidates to achieve unique OAM and CV modes guiding regime.

1.4 OAM and CV beams characterization

OAM and CV beams are known to have zero intensity center as already mentioned above, although this characteristic does not inform OAM topological charge or polarization state of vector mode. Thus, one need to confirm phase information for OAM beam and polarization orientation for CV beams. The experimental identification for CV beams can be done using rotating analyzer, where one need to pass CV beam through linear polarizer (analyzer) and scan its intensity profile using camera(Grosjean, Courjon, & Spajer, 2002; Zheng, Gu, Wang, Xu, & Ming, 2010). The lobe shaped intensity profile is obtained after passing analyzer, and this lobe intensity rotates in defined orientation (based on type of vector mode) with rotation of analyzer.

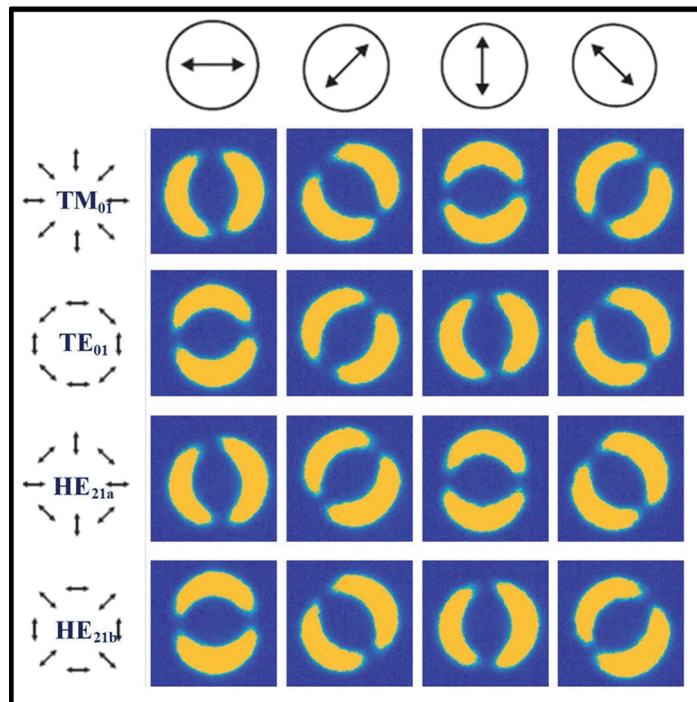


Figure 1.11 Experimental identification of the generated PCVBs (TM_{01} , TE_{01} , even and odd HE_{21} beams) via the rotation of a linear polarizer located in front of the CCD camera
Taken from Pradhan et al. (2018)

Hence by monitoring the intensity profiles of these beams while rotating, one can identify mode under investigation. The Fig. 1.11 shows the intensity patterns of all vector modes profiles with rotating analyzer as detailed in (Pradhan, Sharma, & Ung, 2018).

1.5 Summary

This chapter provides the introduction of OAM and CV beams so as to lay the theoretical bases and the background literature review relevant to this research thesis. The chapter includes a detailed account of scientific advances that have happened in recent years to achieve effective and stable transmission of optical vortex beams. Ring core fiber both standard step index profile and ring core photonic crystal fiber can become the potential solution to achieve high-end optical communication with optical vortices. Therefore, some of the proposed fiber designs for these optical vortices have been reviewed. This chapter further gives information about OAM and CV beams generation in both free space and in optical fiber. Moreover, we include information about the relationship between CV and OAM beams, particularly in fiber. Techniques proposed for the characterization of optical vortex modes are reviewed in detail. The literature review also includes a discussion on recent developments in specialty fiber designs tailored for optical vortices which could benefit application areas like: optical communications, optical sensing, high-resolution imaging and optical trapping.

The following three chapters of this thesis present the novel fiber design, optimization and characterization in order to support optical vortices. Chapter 2 discusses about finite element method (FEM) based simulation of AC-PCF fiber design and parametric optimization to attain fiber properties as: chromatic dispersion, nonlinearities. This is followed by design selection (with optimized parameters) toward supercontinuum generation of optical vortex beams, later using optimized fiber design parameter, a numerical study is presented toward supercontinuum generation. In next chapter, the optimized fiber design is fabricated and characterized for stable propagation of optical vortices, that retains good mode purity. Finally, radially anisotropic ring fiber design is proposed in chapter 4, to achieve co-

propagation of all kinds of OAM (stable or nonstable) beams. Such fiber design could open possibilities for increasing more communication channels as needed.

CHAPTER 2

ENDLESSLY MONO-RADIAL ANNULAR CORE PHOTONIC CRYSTAL FIBER FOR THE BROADBAND TRANSMISSION AND SUPERCONTINUUM GENERATION OF VORTEX BEAMS

M. Sharma¹, P. Pradhan¹ and Bora Ung¹

¹ Department of Electrical Engineering, École de technologie supérieure,
1100 Notre-Dame West, Montreal, Quebec, Canada H3C1K3

Paper published in *Scientific Reports*, February 2019

Résumé

Nous démontrons un nouveau régime de guidage mono-radial dans une fibre à cristaux photoniques avec un cœur annulaire (AC-PCF de l'acronyme anglais: *annular core photonic crystal fiber*) dans lequel seuls les modes guidés d'ordre radial fondamental sont supportés par la fibre à toutes les longueurs d'onde d'excitation. Ce comportement est d'un grand intérêt pour les applications qui nécessitent le guidage stable et à large bande de faisceaux vectoriels cylindriques mono-radiaux (c'est-à-dire en forme de beignet) et de faisceaux vortex transportant un moment angulaire orbital. Nous montrons par ailleurs que l'on peut sculpter de manière significative la dispersion chromatique et les non-linéarités optiques du guide d'onde grâce à une optimisation appropriée de la gaine microstructurée à cristaux photoniques. L'étude analytique des propriétés modales remarquables de la fibre à cristaux photoniques avec un cœur annulaire est validée par des simulations des équations de Maxwell. Par ailleurs, nous avons effectué des simulations de la propagation guidée non linéaire d'impulsions femtosecondes à une longueur d'onde centrale de 835 nm et à une puissance crête du kilowatt, qui indiquent que la fibre à cristaux photoniques avec un cœur annulaire représente une approche prometteuse pour étudier la génération de supercontinuum

de vortex optique. La fibre que nous proposons a des applications potentielles dans le multiplexage spatial, la détection optique et la microscopie à super-résolution.

2.1 Abstract

We demonstrate a new guiding regime termed endlessly mono-radial, in the proposed annular core photonic crystal fiber (AC-PCF), whereby only modes of the fundamental radial order are supported by the fiber at all input wavelengths. This attribute is of high interest for applications that require the stable and broadband guiding of mono-radial (i.e. doughnut shaped) cylindrical vector beams and vortex beams carrying orbital angular momentum. We further show that one can significantly tailor the chromatic dispersion and optical nonlinearities of the waveguide through proper optimization of the photonic crystal microstructured cladding. The analytical investigation of the remarkable modal properties of the AC-PCF is validated by full-vector simulations. As an example, we performed simulations of the nonlinear fiber propagation of short femtosecond pulses at 835 nm center wavelength and kilowatt-level peak power, which indicate that the AC-PCF represents a promising avenue to investigate the supercontinuum generation of optical vortex light. The proposed fiber design has potential applications in space-division multiplexing, optical sensing and super-resolution microscopy.

2.2 Introduction

Orbital angular momentum (OAM) beams, aka optical vortices, and cylindrical vector beams (CVB) exhibit an annular intensity profile that possesses a zero on-axis intensity due to a phase singularity and a polarization singularity, respectively (Yao & Padgett, 2011; Zhan, 2009). Optical vortex beams may carry both spin and orbital angular momenta owing to circular polarization and a helically varying phase front (described by a phase term $\exp(il\theta)$ in the transverse plane, where θ is the azimuthal coordinate and l refers to the topological charge), respectively. The peculiar doughnut shaped intensity distribution as well as the theoretically infinite topological states and the inhomogeneous polarization have allowed

researchers to push the frontiers of optical physics and explore new modalities in super-resolution imaging (L. Li & Li, 2013; K. Liu et al., 2017; Snoeyink & Wereley, 2013), laser material processing (Duocastella & Arnold, 2012; Hamazaki et al., 2010; Weber et al., 2011), optical trapping (Gecevičius, Drevinskas, Beresna, & Kazansky, 2014; Padgett & Bowman, 2011), sensing (Brullot et al., 2016; Niederriter, Siemens, & Gopinath, 2015) and space-division multiplexing (SDM) (Rusch, Rad, Allahverdyan, Fazal, & Bernier, 2018; Willner et al., 2015), to name a few.

One well-established application of vortex beams pertains to stimulated emission depletion (STED) super-resolution microscopy where an annular beam is used together with a co-aligned Gaussian beam in order to breach the diffraction limit (Yu et al., 2016). Another intriguing area of research relates to probing of chiral light-matter interactions with potential applications in molecular spectroscopy (Cameron, Götte, Barnett, & Yao, 2017). These applications of vortex beams would benefit from the versatility of a broadband coherent source of OAM light (Wildanger et al., 2008). In this regard, researchers have explored free-space methods for the generation of broadband vortex light, including: nonlinear crystals (Neshev, Dreischuh, Maleshkov, Samoc, & Kivshar, 2010; Tokizane, Oka, & Morita, 2009), nonlinear gases (Hansinger et al., 2016), nanostructured metamaterials (Z. Zhao, Wang, Li, & Willner, 2013) and wideband q -plates (Gecevičius et al., 2018; Rumala et al., 2013). However, these free-space methods still harbour some technical limitations in the continuum's wavelength coverage or in spatial dispersion. An alternate approach pertains to supercontinuum generation in nonlinear optical fibers, which could extend the spectral coverage of the ensuing optical vortex beams.

To this end, photonic crystal fibers (PCF) have demonstrated key optical properties such as *endlessly single-mode guiding*, high nonlinearities and chromatic dispersion engineering, making it an ideal medium for supercontinuum generation (Birks et al., 1997; Dudley et al., 2006). Prior research was conducted on PCF and photonic bandgap fiber designs towards SDM transmission applications (H. Li et al., 2016; Hu Zhang et al., 2017). A recent study

proposed a ring core chalcogenide glass photonic crystal fiber design with promising numerical results of supercontinuum generation in the infrared (Yue et al., 2012). A fiber based supercontinuum generation of the high-order ($l = 8$) OAM beam was also experimentally demonstrated in the near-infrared spectrum using a 3.5m long air-core fiber (Prabhakar, Gregg, Rishøj, & Ramachandran, 2016). Both previous studies however did not specifically address the issue of the broadband stability of vortex beams guided in the fundamental radial order, which is critical to ensure high purity of the mono-annular CVB and OAM beams at the fiber output across the widest spectral range possible.

In this work, we uncover a novel waveguiding regime in the annular core photonic crystal fiber (AC-PCF) thereby supporting the *endlessly mono-radial* (EMR) guiding regime, where the fiber enforces wavelength independent “doughnut-shaped” mono-annular guided modes. The latter property is vital as it opens the possibility to achieve the broadest and purest fiber supercontinuum vortex light supported by fiber eigenmodes of the fundamental radial order. The parameterization of the AC-PCF is presented below along with the theory that allows the optimization of its modal properties, including the special EMR guiding regime. These results are validated through full-vector finite element method (FEM) calculations (using COMSOL Multiphysics package) with perfectly matched layer boundary conditions. Further, we theoretically study optimized designs of nonlinear AC-PCF towards the supercontinuum generation in the visible-near-infrared spectrum by the numerical solution of the generalized nonlinear Schrödinger equation via the split step Fourier method.

2.3 Description of the annular-core photonic crystal fiber design

The proposed AC-PCF structure shown in Fig. 2.1(a) resembles that of a standard hexagonal lattice PCF described via air hole diameter (d), pitch (Λ) and number of rings of air holes (N). The key difference though, is that in the case of the AC-PCF waveguiding occurs within a “ring” of six missing holes; while in the standard PCF the optical mode is guided around a missing center hole.

Assuming that the holey cladding can be modeled as a homogeneous material of tunable refractive index via the fill ratio d/Λ , one realizes that the modal properties of the AC-PCF can be investigated by means of the functionally comparable all-solid ring-core fiber (Brunet, Ung, et al., 2014). Therefore, the AC-PCF exhibits analogous waveguiding features such as a fundamental HE_{11} mode showing an annular intensity profile (Fig. 2.1(b)) along with other cylindrical vector modes TE_{0m} , HE_{2m} , TM_{0m} and other higher order mode EH_{1m} and HE_{3m} with radial order $m = 1$. In Fig. 2.1(c) we present the intensity and phase distributions of $OAM_{\pm 11}$ modes supported in a AC-PCF through the coherent superposition of hybrid modes: $OAM_{\pm 11} = HE_{21(\text{even})} \mp i HE_{21(\text{odd})}$. We note that other higher-order OAM modes can be supported by the fiber such as: $OAM_{\pm 21} = HE_{31(\text{even})} \mp i HE_{31(\text{odd})}$ and $OAM_{\pm 21} = EH_{11(\text{even})} \pm i EH_{11(\text{odd})}$.

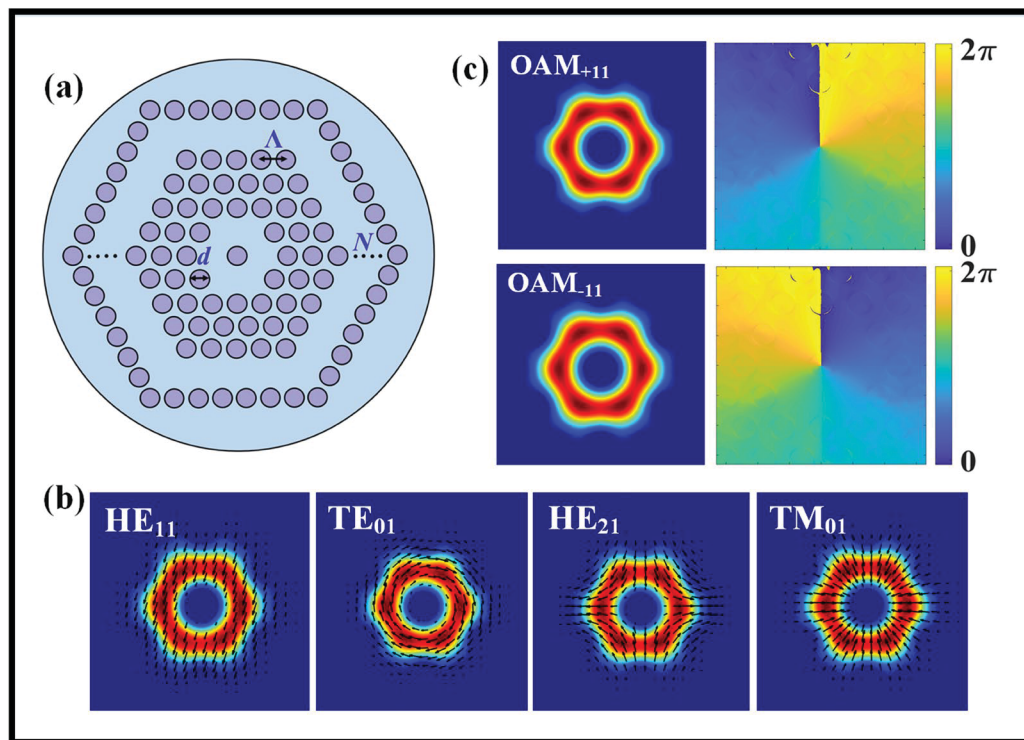


Figure 2.1 (a) Schematic of the cross-section of AC-PCF (b) Simulated intensity profiles of the first 4 guided vector modes. (c) Intensity and phase distributions of the $OAM_{\mp 11}$ modes supported by the AC-PCF

The light guiding properties of optical fibers are commonly modelled via the dimensionless V -number. In the case of the AC-PCF we define this parameter as $V = (2\pi b/\lambda) \left(\sqrt{n_{core}^2 - n_{clad}^2} \right)$ where the effective core radius is $b = 2\Lambda/3$, the core refractive index corresponds to that of the solid glass ($n_{core} = n_{glass}$), and the refractive index of the holey cladding is defined by the effective index of the fundamental space-filling mode ($n_{clad} = n_{FSM}$), in the triangular lattice of air-holes. Based on the latter analytical formalism, the AC-PCF enables single mode operation for $V < 2.405$, as displayed by standard optical fibers and all-solid ring-core fibers (Brunet, Ung, et al., 2014).

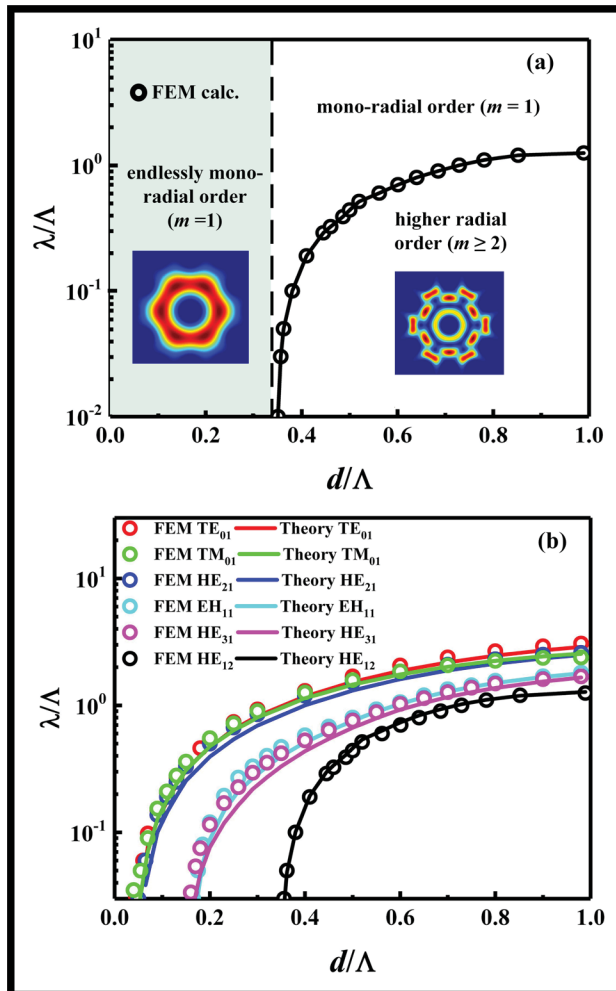


Figure 2.2 (a) Localization of the endlessly mono-radial-order regime in the normalized λ/Λ vs d/Λ parameter space of AC-PCFs (b) Modal cut-offs for the TE_{01} , HE_{21} , TM_{01} , HE_{31} , EH_{11} and HE_{12} modes predicted by analytical theory and validated by full-vector FEM

For applications previously outlined, it is crucial to prevent the onset of the first bi-annular eigenmode with $m = 2$, namely the HE_{12} mode, which occurs for $V \geq V_{cut}$; where $V_{cut} = 3.832$ is the HE_{12} mode cut-off. In that regard, the most prominent feature of the AC-PCF is its ability for *endlessly mono-radial-order* (EMR) guiding, in which case modes with fundamental radial order $m = 1$ are strictly supported by the fiber at all input wavelengths (Fig. 2.2(a)). The threshold of this special waveguiding regime was identified through FEM calculations for relative hole diameters less than 0.35 (namely $d/\Lambda < 0.35$). The ability to enforce modes with $m = 1$ inside an EMR-guiding AC-PCF helps to mitigate issues related to mode coupling with undesired higher-radial-order modes ($m \geq 2$). The latter feature is also desirable, among others, in SDM applications using CVB and OAM beams where mux/demux operations generally assume the coaxial alignment of modes in the fundamental radial order (Willner et al., 2015). The full list of possible mono-radial ($m = 1$) modes supported in the EMR regime are: HE_{11} , TE_{01} , HE_{21} , TM_{01} , EH_{11} and HE_{31} . Figure 2.2(b) demonstrates that the cut-off conditions for these modes of interest along with that of the HE_{12} mode, as predicted by the analytical model (Brunet, Ung, et al., 2014), are in good quantitative agreement with the full-vector FEM numerical calculations.

We recall that the fundamental HE_{11} mode has no cut-off. Small deviations between the analytical description and FEM simulations of the AC-PCF can be attributed to the fact that ring-core fibers and AC-PCF fibers are not identical in shape due to the inhomogeneous photonic crystal cladding present in the latter type of fiber, and also because the ring-core fiber model assumes the same refractive index in the inner and outer claddings (while this condition is not exactly met in the case of the AC-PCF). The procedure used for the determination of the modal cut-offs is detailed in the Methods section.

2.4 Optimization of fiber parameters for supercontinuum generation in the visible-near-infrared

In this section, a fused silica glass AC-PCF is optimized for parameters relevant to supercontinuum generation (SCG) in fiber by means of guided CVB and OAM modes: high optical nonlinearity, high modal effective index separation and near-zero chromatic dispersion at the input pump wavelength of 835 nm. Figure 2.3 shows the value of the effective mode area (A_{eff}) and nonlinear parameter (γ) of a silica AC-PCF operating inside the EMR waveguiding regime ($d/\Lambda < 0.35$) at $\lambda = 835$ nm for the HE_{21} mode. We note that in this section we have limited our discussion to the HE_{21} mode for concision since its modal properties very closely mirror that of the TE_{01} and TM_{01} modes, and also because the even and odd HE_{21} modes serve as the basis set to create the $OAM_{\pm 11}$ modes of interest. In our numerical analysis we have defined the threshold for modal cut-off as the level where less than 40% of the optical power is guided within the core region of the fiber (a detailed description of this criterion for modal cut-off is presented in the Methods section). Inexistent data corresponding to regions of modal cut-offs have duly been identified in Figs 2.3 to 2.5.

One can observe in Fig. 2.3(a) that the mode confinement, i.e. value of A_{eff} , decreases with increase in the d/Λ ratio, and increases with the hole pitch (Λ). Since the nonlinear parameter is defined as $\gamma = 2\pi n_2 / (\lambda A_{eff})$, where n_2 is the nonlinear refractive index of the glass, we observe the reverse relationship for γ as a function of d/Λ and Λ .

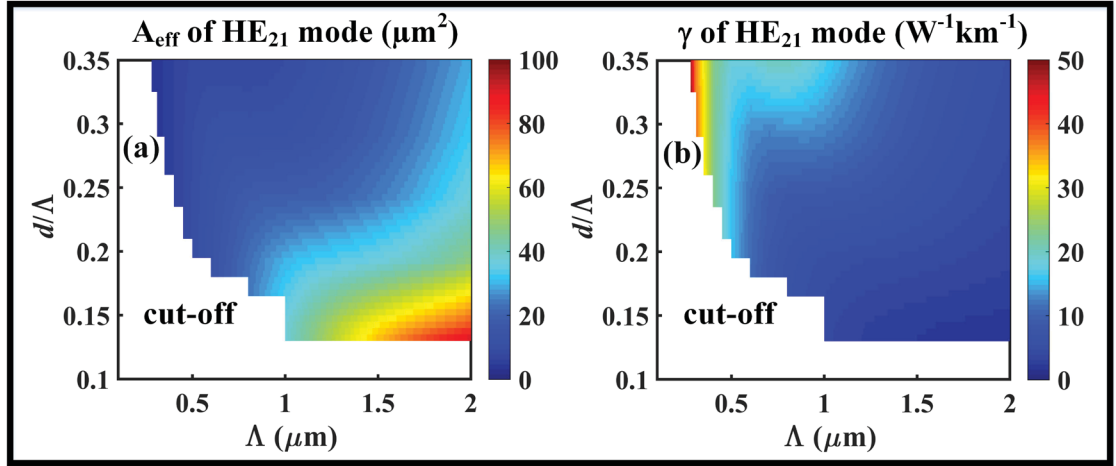


Figure 2.3 (a) Effective mode area, and (b) nonlinear parameter of the HE_{21} mode at $\lambda = 835$ nm in a silica AC-PCF operating in the endlessly mono-radial-order guiding regime

Hence the optimization of optical nonlinearities (i.e. magnitude of γ) can be achieved with fiber structures presenting aspect ratios near the edge of the EMR regime ($d/\Lambda = 0.35$) and for smaller hole periods. However, lowering the value of Λ eventually creates a very small core region that forces the guided mode to have a significant fraction of its power leaking into the cladding region and to eventually cut-off. Figure 2.3(b) displays the nonlinear parameter (γ) values for silica AC-PCF in the EMR at $\lambda = 835$ nm for the HE_{21} mode. We note that the value of γ increases with the d/Λ ratio, while decreases with Λ as expected from the inverse relationship with the effective mode area. In particular, high nonlinearities can be achieved for normalized hole diameters in the $0.2 < d/\Lambda < 0.35$ range and for sub-micron periods ($\Lambda < 1 \mu\text{m}$).

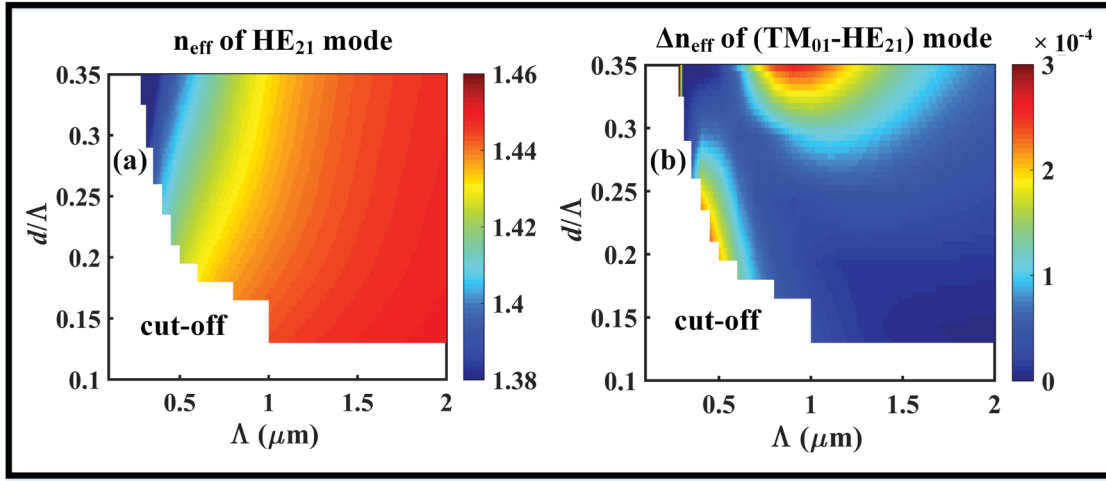


Figure 2.4 (a) Effective index of the HE_{21} mode and (b) its minimum effective index separation inside the LP_{11} group at $\lambda = 835$ nm in a silica AC-PCF operating in the endlessly mono-radial-order regime

Moreover, the fiber is designed for the stable propagation of mono-radial OAM beams, which depends on lifting the modal degeneracy of the constituent hybrid HE/EH cylindrical vector modes (S Ramachandran, Gregg, Kristensen, & Golowich, 2015; Ung, Vaity, et al., 2014; Yue et al., 2012). A common rule of thumb is to maintain a minimum intermodal separation of the effective indices of $\Delta n_{\text{eff}} \geq 10^{-4}$ between adjacent vector modes so as to promote their fiber transmission stability (S Ramachandran et al., 2015; Ung, Vaity, et al., 2014). Figure 2.4(a,b) shows the value of the HE_{21} effective mode index (n_{eff}) and its minimum intermodal separation (Δn_{eff}) with respect to the adjacent vector modes TE_{01} and TM_{01} . Figure 2.4(a) indicates that the value of n_{eff} increases almost linearly with the pitch Λ , ostensibly because a larger core radius ($b = 2\Lambda/3$) promotes a better E -field overlap within the high-refractive-index annular ring. Figure 2.4(b) indicates that a parametric space with sufficient intermodal separation is found in the region roughly bounded by $(0.3 \leq d/\Lambda \leq 0.35)$ and $(0.8 \leq \Lambda \leq 1.6 \mu\text{m})$. Similarly, another interesting region for the stable propagation of the HE_{21} mode can be found for small fiber geometries with $(0.18 \leq d/\Lambda \leq 0.25)$ and $(0.3 \leq \Lambda \leq 0.7 \mu\text{m})$, although this second region is located near the modal cut-off.

2.5 Chromatic dispersion engineering

The chromatic dispersion plays an important role in supercontinuum generation as it determines the extent to which spectral components of a short pulse will travel with different velocities. The undesirable effect of group velocity chromatic dispersion (GVD) is the temporal broadening of the optical pulse that ultimately affects the phase-matching and excitation of optical nonlinearities in the fiber. The GVD in the fiber is commonly described by the dispersion parameter (D) in units of ps/(km-nm):

$$D = -\frac{\lambda}{c} \frac{d^2 n_{eff}}{d\lambda^2} \quad (2.1)$$

where n_{eff} is the wavelength-dependent effective refractive index of the propagating mode of interest in the single-material fiber (silica in this case). We note that the material contribution to the total chromatic dispersion was here taken into account by implementing the Sellmeier equation of pure fused silica in our simulations. Similar to what was achieved with regular PCFs (Agrawal, 2000; Dudley & Taylor, 2010), we demonstrate below the ability to engineer the chromatic dispersion of CVBs and OAM modes in an AC-PCF through the precise tuning of its microstructure.

Henceforth, we investigated the dependence of the GVD on the geometrical parameters (d and Λ) of a silica AC-PCF optimized for supercontinuum generation at 835 nm input wavelength in the few femtoseconds regime. Our calculations in Fig. 2.5 indicate that low dispersion can be achieved inside a relatively large parameter space: ($0.3 \leq d/\Lambda \leq 0.35$) and ($1 \leq \Lambda \leq 2 \mu\text{m}$). Similarly, a smaller region of low GVD occurs near modal cut-off for ($0.18 \leq d/\Lambda \leq 0.25$) and ($0.3 \leq \Lambda \leq 0.7 \mu\text{m}$).

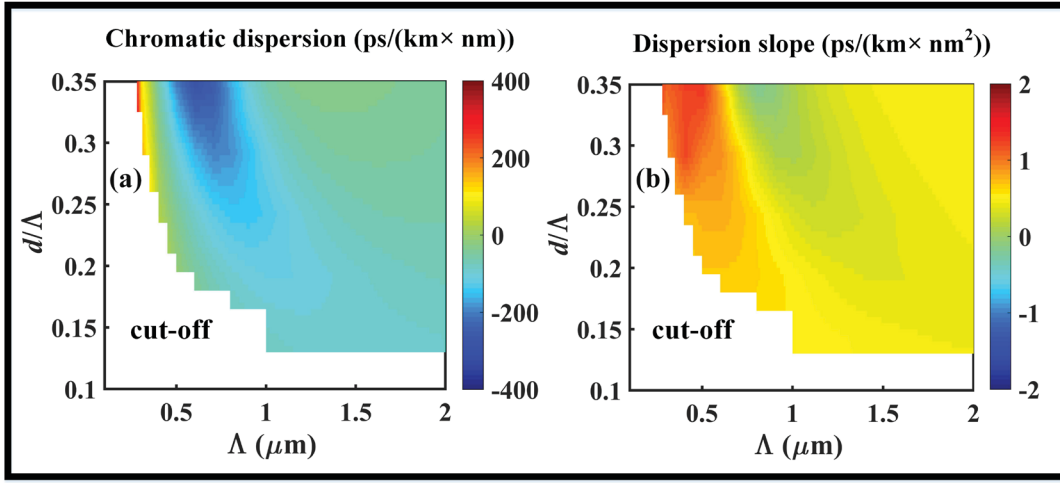


Figure 2.5 (a) Plot of the group velocity chromatic dispersion and (b) dispersion slope of HE_{21} mode at $\lambda = 835 \text{ nm}$ in silica AC-PCF within the endlessly mono-radial-order regime

Within these interesting regions of low absolute dispersion, inspection of Fig. 2.5(b) allows to further mitigate the effects of third-order dispersion by plotting the dispersion slope, which should also be minimized in order to enhance phase-matching with optical nonlinearities. In that regard we observe low dispersion slope values for fiber geometries with $(0.3 \leq d/\Lambda \leq 0.35)$ and $(0.8 \leq \Lambda \leq 1.2 \mu\text{m})$ that is co-located with a desirable region of low absolute GVD.

Figure 2.6 plots the chromatic dispersion as a function of wavelength for a number of potentially interesting AC-PCF configurations. In particular, for a given fixed pitch value of $\Lambda = 0.5 \mu\text{m}$, Fig. 2.6(a) indicates that it is possible to go from a near-zero dispersion at $\lambda = 835 \text{ nm}$ to high negative dispersion (in the normal dispersion regime), by increasing the normalized hole diameter (d/Λ) from 0.20 to 0.32. On the other hand, if one keeps the normalized hole diameter constant while increasing the pitch, Fig. 2.6(b) indicates that the GVD progressively shifts toward higher positive values in the direction of anomalous dispersion.

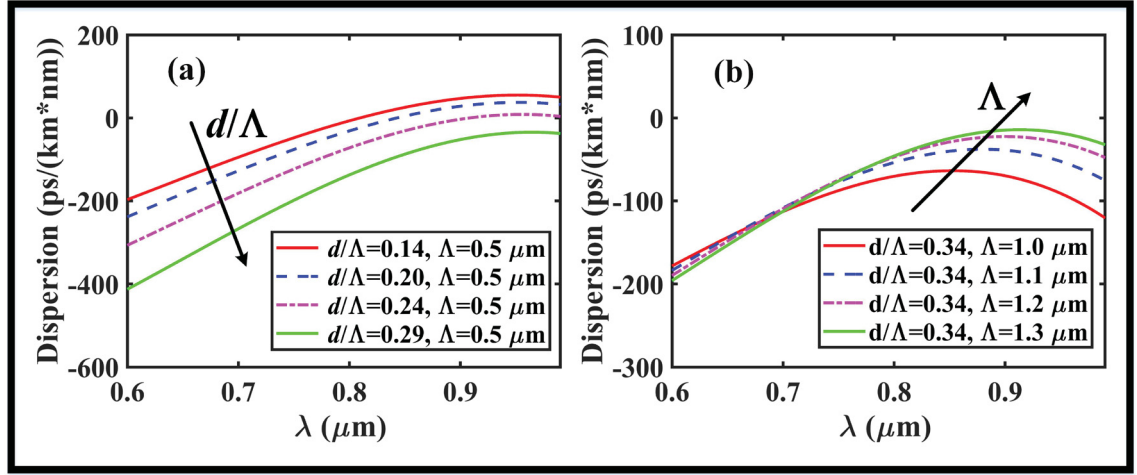


Figure 2.6 Group velocity dispersion curves for (a) different values of normalized hole diameters d/Λ with fixed period $\Lambda = 0.5 \mu\text{m}$, and (b) for various periods Λ with fixed ratio $d/\Lambda = 0.34$

Based on the analysis of Fig.2.6, we selected two promising designs of AC-PCF (also keeping in consideration practical fiber fabrication limitations) named “Fiber 1” and “Fiber 2” for the supercontinuum generation with short optical pulses centered at $\lambda = 835 \text{ nm}$. The structural parameters of the two optimized fiber designs and their principal modal properties are presented in Table 1.

Table 2.1 Linear and nonlinear optical properties of the HE_{21} mode in two designs of silica AC-PCF optimized for supercontinuum generation at 835 nm wavelength

	d/Λ	Λ (μm)	γ ($\text{W}^{-1} \text{ km}^{-1}$)	β_2 (s^2/m) (10^{-27})	β_3 (s^3/m) (10^{-41})	β_4 (s^4/m) (10^{-55})	β_5 (s^5/m) (10^{-70})	β_6 (s^6/m) (10^{-84})	β_7 (s^7/m) (10^{-98})
Fiber 1	0.34	1.3	10.6	11.25	3.21	1.84	9.89	-5.63	15
Fiber 2	0.20	0.5	14.7	4.61	7.73	1.04	26.7	-84.5	9.25

The β values in Table 1 denote the coefficients of the Taylor series expansion of the wavenumber $\beta(\omega)$ about the pulse’s center frequency (ω_0) (Agrawal, 2000). Here we note that β_1 (i.e. group velocity) was omitted since the calculations of the nonlinear pulse propagation in the next Section were performed in a moving time reference frame. In addition, we confirmed that the mode purity of the generated $\text{OAM}_{\pm 11}$ beams using both fiber

designs remained very high (> 96%) across the whole simulated range of wavelengths from 600 to 1200 nm. Details of the OAM mode purity calculations based on a modal field decomposition into spiral harmonics are provided in the Methods section

2.6 Numerical simulation of supercontinuum generation in AC-PCF

The nonlinear pulse propagation in the fiber can be simulated by solving the generalized nonlinear Schrödinger equation (GNLSE) (Agrawal, 2000; Dudley & Taylor, 2010) :

$$\frac{\partial A}{\partial z} + \frac{\alpha}{2}A - \sum_{n=2}^{\infty} \frac{i^{n+1}}{n!} \beta_n \frac{\partial^n A}{\partial T^n} = i\gamma \left(1 + i\tau_{shock} \frac{\partial}{\partial T} \right) \left(A(z, t) \int_{-\infty}^t R(t') \times |A(z, t - t')|^2 dt' \right) \quad (2.2)$$

Where, $A = A(z, t)$ is the electric field envelop, α is the attenuation constant, β_n is the n^{th} order dispersion coefficient [see Table 1] about the center frequency ω_0 , and γ is the nonlinear parameter given by:

$$\gamma = \frac{2\pi n_2}{\lambda A_{eff}} \quad (2.3)$$

In Eq. (2.3), n_2 represents the nonlinear refractive index of fused silica, λ denotes the wavelength and A_{eff} is the effective mode area as defined by (Afshar & Monro, 2009):

$$A_{eff} = \frac{\left| \int (\vec{e}_v \times \vec{h}_v^*) \cdot \vec{z} dA \right|^2}{\int |(\vec{e}_v \times \vec{h}_v^*) \cdot \vec{z}|^2 dA} \quad (2.4)$$

In Eq.(2.4), $\vec{e}_v(x, y, \omega)$ and $\vec{h}_v(x, y, \omega)$ respectively denote the transverse electric and magnetic vector field distributions which were here calculated via FEM simulations. The time

derivative term on the right-hand side of Eq. (2.2) includes the effect of dispersion owing to nonlinearity, associated with the phenomena of self-steepening and optical shock. The first term in the definition of τ_{shock} below is the dominant contribution while the second term includes the effect of the frequency-dependent effective mode area and nonlinear refractive index, as (Blow & Wood, 1989):

$$\tau_{shock} = \frac{1}{\omega_0} + \frac{d}{d\omega} \left[\ln \left(\frac{n_2(\omega)}{A_{eff}(\omega)} \right) \right]_{\omega_0} \quad (2.5)$$

This equation can be rewritten as:

$$\tau_{shock} = \frac{1}{\omega_0} + \left[\frac{1}{n_2(\omega)} \left(\frac{dn_2(\omega)}{d\omega} \right)_{\omega_0} - \frac{1}{A_{eff}(\omega)} \left(\frac{dA_{eff}(\omega)}{d\omega} \right)_{\omega_0} \right] \quad (2.6)$$

In this study we have utilized Eq. (2.6) to determine the shock time scale that takes into account the dependence of the optical shock time on the effective mode area, while we neglected the contribution from the frequency dependence of the nonlinear index n_2 , since this contribution is negligibly small. Further, frequency dependent effective mode area (third term in Eq. 2.6) is higher for Fiber 2 in comparison to Fiber 1, since mode area in Fiber 2 has a larger variation with change in wavelength as this design is closer to cut-off condition. The obtained values for τ_{shock} at the pump's central wavelength (835 nm) are thus found to be 0.62 fs and 0.59 fs for Fiber 1 and Fiber 2, respectively. The total nonlinear response $R(t)$ of the material, which includes both the instantaneous electronic and delayed ionic Raman contributions, is described as:

$$R(t) = (1 - f_R)\delta(t) + f_R h_R(t) \quad (2.7)$$

where in the case of silica glass we have $f_R = 0.18$ for the fractional contribution to the delayed Raman response, $\delta(t)$ is the Dirac function and h_R is the Raman response function which can be analytically modeled as:

$$h_R(t) = (1 - f_b)(\tau_1^2 + \tau_2^2)\tau_1 \exp\left(\frac{-t}{\tau_2}\right) \sin\left(\frac{t}{\tau_1}\right) + f_b \left[\frac{(2\tau_b - t)}{\tau_b^2}\right] \exp\left(\frac{-t}{\tau_b}\right) \quad (2.8)$$

where for silica (Lin & Agrawal, 2006): $\tau_1 = 12.2$ fs, $\tau_2 = 32$ fs, $f_b = 0.21$, $\tau_b = 96$ fs.

In general, the GNLSE must be solved through numerical methods. To that end, the split-step Fourier method is based on parsing the linear dispersive and nonlinear contributions of the GNLSE and solving them independently over small half discretization steps (Deiterding, Glowinski, Oliver, & Poole, 2013; Muslu & Erbay, 2003) Based on the latter approach to solving Eq. (2.2), we performed simulations of supercontinuum generation in a 20 cm long silica AC-PCF using the optimized parameters of Fiber 1 and Fiber 2 presented in Table 1. Simulations were performed using an unchirped Gaussian pulse of $\tau_{FWHM} = 60$ fs duration and 10 kW peak power (P_p). At $\lambda = 835$ nm center wavelength, Fiber 1 and Fiber 2 are both pumped in the normal dispersion regime ($D = -30.1$ and -12.56 ps/(km · nm), respectively) with nonlinear coefficient $\gamma = 10.6$ and 14.7 W⁻¹ km⁻¹. We note that since the designed fiber has no form birefringence, the effect of polarization coupling were not considered in the solution to GNLSE. Figure 2.7(a) shows the spectral and temporal evolution of the input Gaussian pulse in Fiber 1.

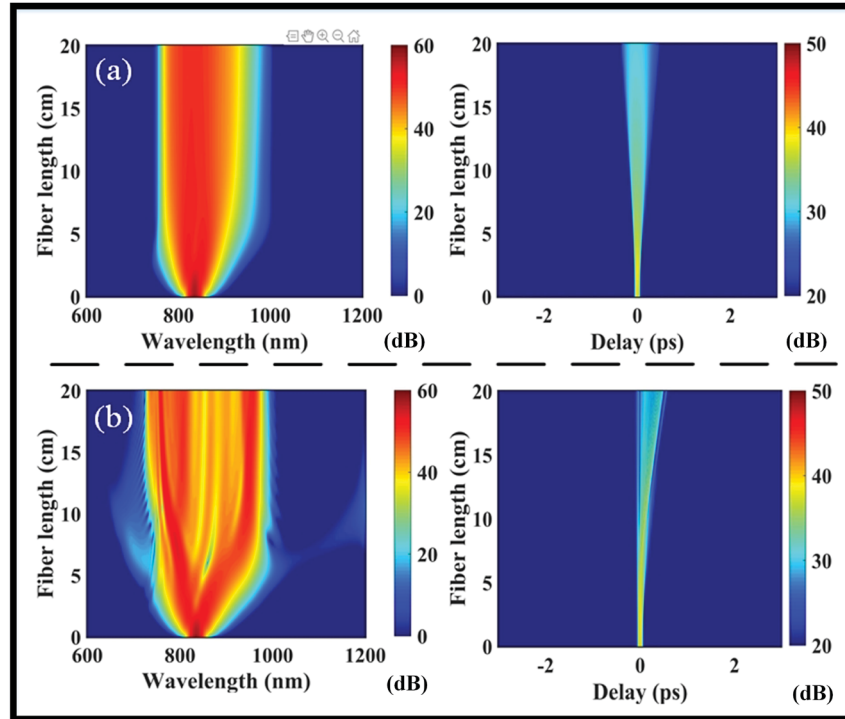


Figure 2.7 (a) Pulse spectral and temporal profiles as a function of propagation in (a) Fiber 1 with $\Lambda = 1.3 \mu\text{m}$ and $d/\Lambda = 0.34$, and (b) Fiber 2 with $\Lambda = 0.5 \mu\text{m}$ and $d/\Lambda = 0.2$ for 10 kW peak input power

Initial evolution of the spectrum is characterized by self-phase modulation and normal dispersion as these phenomena together leads to substantial spectral and temporal broadening as well as a rapid decrease in peak power over a short distance as expected (Agrawal, 2000). The significant amount of normal dispersion in Fiber 1 limits the nonlinear spectral broadening of the input pulse, the full extent of which occurs within 3 centimeters propagation length and is followed by the formation of additional red-shifted components due to Raman scattering. Figure 2.7(b) also illustrates temporal and spectral broadening of the input pulse for Fiber 2 since it is similarly pumped in the normal dispersion regime. However, the pumping occurs closer to the zero-dispersion wavelength and with a larger nonlinear coefficient. The latter conditions allow for a more rapid spectral broadening and significant power transfer towards the anomalous dispersion region. In this case, we thus observe complex soliton fission dynamics coupled with Raman scattering that results in dispersive-wave generation and a fine structuring of the output pulse spectrum.

Another set of calculations was performed to simulate the output spectrum after 20 cm propagation in either Fiber 1 or Fiber 2, for various levels of peak power (1, 10, 100 kW) of a 60 fs input pulse. We note that experimental demonstrations of SCG in small-core nonlinear fibers using comparable kW-level femtosecond pulses have been demonstrated in the past (Dudley et al., 2006). Figure 2.8(a) shows the corresponding spectral profile simulated for Fiber 1 where we observe that nonlinear spectral broadening dominates over the effects of chromatic dispersion such that an output spectrum spanning from 696 to 1058 nm at -20 dB from the top is obtained for 100 kW peak power. In the case of Fiber 2 in Fig. 2.8(b), the highest peak power is shown to translate into more power towards the anomalous dispersion regime such that the mechanisms of soliton fission and dispersive wave generation are more prominently displayed and lead to a spectral broadening spanning from 644 to 1219 nm at $P_p = 100$ kW.

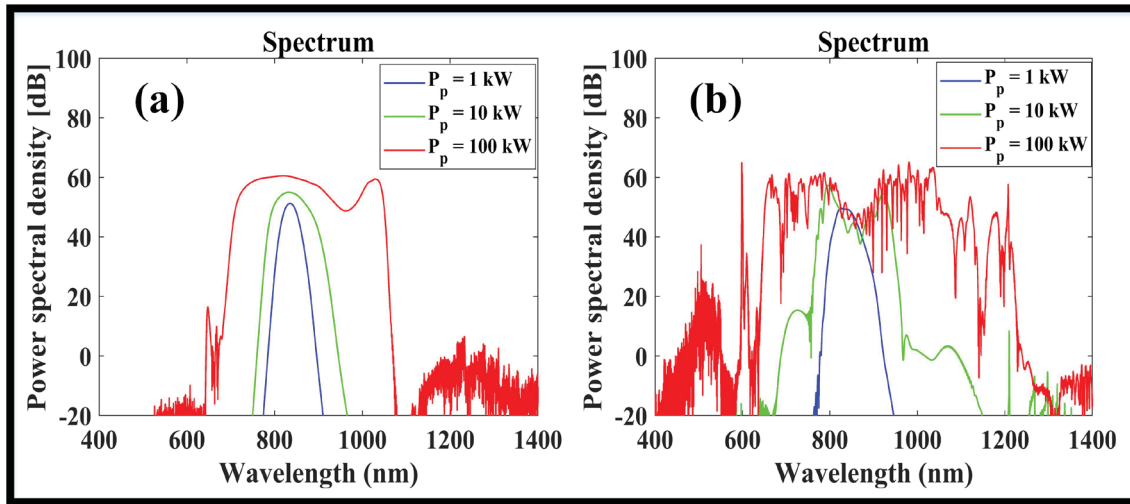


Figure 2.8 Output pulse spectra after 20 cm propagation in AC-PCF with (a) $\Lambda = 1.3 \mu\text{m}$ and $d/\Lambda = 0.34$ (Fiber 1), and (b) $\Lambda = 0.5 \mu\text{m}$ and $d/\Lambda = 0.2$ (Fiber 2) as a function of input pulse peak powers P_p

Hence, Fiber 2 with structural parameters $\Lambda = 0.5 \mu\text{m}$ and $d/\Lambda = 0.2$ represents the most promising fiber design for supercontinuum generation due to its higher optical nonlinearities and lower group velocity dispersion. However, fabrication of this design with very small

holes of diameter $d = 0.1 \mu\text{m}$ could pose practical problems, in which case the design of Fiber 1 will represent a viable alternate solution. The proposed fiber design is amenable to fabrication via the established stack-and-draw technique. For applications in the near-to-far infrared spectrum (including the C-band) for which hole diameters are relatively large ($d \geq 1 \mu\text{m}$) we expect no particular fabrication issues. However for applications that include the visible range (as in the present study) the holey cladding can become deeply sub-micron in size, such that particular care must be taken throughout the fiber fabrication process starting from the preform creation to the fiber drawing under precisely controlled gas pressure. Tolerance of the fiber design to imperfections in the fabrication process can be inferred from the parametric study of the modal properties shown in Figs 2.3–2.5. We remark that because the point of operation in Fiber 2 is close to cut-off, this specific design has low tolerance to perturbations in the nominal values of the structural parameters Λ and d/Λ . In the case of Fiber 1, Fig. 2.4(b) indicates that the minimum modal separation (Δn_{eff}) remains above the 10^{-4} threshold even for changes in the structural parameters as large as 10%. Figures 2.3 and 2.5 similarly indicate that Fiber 1 retains a fair degree of tolerance to structural perturbations (as large as 5%) with respect to optimal optical nonlinearities and GVD.

2.7 Conclusion

In summary, we have studied the design and simulation of the triangular-lattice annular core photonic crystal fiber (AC-PCF) enabling both the stable broadband guided-transmission and supercontinuum generation of optical vortex beams in fiber. The analytical investigation, supported by numerical simulations, shows that a novel waveguiding regime is possible in the AC-PCF in which the fiber strictly supports modes of the fundamental radial order at all wavelengths. This special regime, here called endlessly mono-radial, occurs when the photonic crystal structure obeys the condition $d/\Lambda < 0.35$. Similarly to standard PCFs, we also show that the AC-PCF can be tailor to enhance the optical nonlinearities as well as engineer the chromatic dispersion of the fiber. The unique waveguiding features of the proposed design thus make it an ideal medium to study mono-annular beams, namely

cylindrical vector beams and orbital angular momentum beams, within a linear or nonlinear broadband regime solely limited by the transparency window of the host material. In particular, we demonstrate through numerical solutions of the generalized nonlinear Schrödinger equation that properly optimized designs of the endlessly mono-radial AC-PCF can support the supercontinuum generation of stable optical vortex beams. The work is relevant to research in the topical areas of space-division multiplexing, super-resolution microscopy and optical sensing via structured light.

Contributions :

M.S. and B.U. contributed to the optical fiber design and co-wrote the manuscript. All authors contributed to the analysis and discussion of the data and reviewed the manuscript. B.U. conceived the idea and provided primary supervision of the work.

2.8 Appendix

Methods

We here describe the method of validation via FEM-based calculations of the AC-PCF's modal cutoffs with the reported full-vector analytical theory detailed in (Brunet, Ung, et al., 2014) for the functionally equivalent ring-core fiber (in an effective-index model). Here we note that in the design of AC-PCF in Fig. 2.1(a) the first ring of air holes are missing, whilst in a standard PCF it is the central hole that is missing. A proposed definition for the effective core radius (b) of an AC-PCF is $b = 2\Lambda/3$, thus exactly twice the value proposed for the PCF in (Saitoh & Koshiba, 2005).

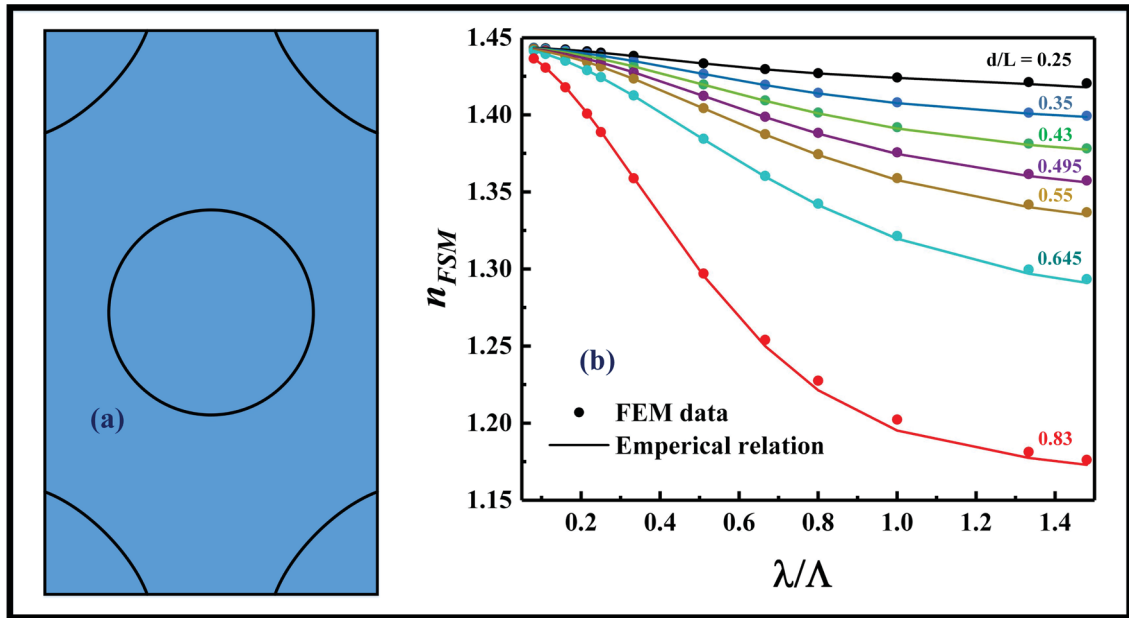


Figure 2.9 (a) Unit cell used in the FEM solver of the (b) effective index of the fundamental space-filling mode (n_{FSM}) as a function of normalized wavelength (λ/Λ) for different values of d/Λ aspect ratios. A comparison between the full-vector calculations with the approximate empirical relation in (Saitoh & Koshiba, 2005) is also presented

The AC-PCF is further defined by its core refractive index n_{core} , (i.e. refractive index of the host material) and the effective refractive index of the cladding as defined by the fundamental space-filling mode (n_{FSM}) in the triangular lattice of air holes of diameter d and period Λ . In this work, we obtained the effective index of the fundamental space-filling mode (Fig. 2.9(b)) by means of the full-vector FEM eigenmode solution of the infinite triangular lattice of air holes (where periodic boundary conditions were implemented on all sides of the unit cell in Fig. 2.9(a)). For validation purposes, the numerical results were compared with a reported empirical model in (Saitoh & Koshiba, 2005) as depicted in Fig. 2.9(b).

The condition of cut-off frequency for different eigenmodes (TE_{0m} , TM_{0m} , $HE_{v,m}$ and $EH_{v,m}$) of the ring core fiber are analytically defined in Eqs 2.9–2.12, respectively (Brunet, Ung, et al., 2014):

$$J_0(V_0)N_2(\rho V_0) - N_0(V_0)J_2(\rho V_0) = 0 \quad (2.9)$$

$$J_0(V_0)N_2(\rho V_0) - N_0(V_0)J_2(\rho V_0) = \frac{(1-n_0^2)}{n_0^2} [J_0(V_0)N_0(\rho V_0) - J_0(\rho V_0)N_0(V_0)] \quad (2.10)$$

$$J_{v-2}(V_0)N_v(\rho V_0) - N_{v-2}(V_0)J_v(\rho V_0) = \frac{(1-n_0^2)}{(1+n_0^2)} [J_v(V_0)N_v(\rho V_0) - J_v(\rho V_0)N_v(V_0)] \quad (2.11)$$

$$J_{v+2}(V_0)N_v(\rho V_0) - N_{v+2}(V_0)J_v(\rho V_0) = \frac{(1-n_0^2)}{(1+n_0^2)} [J_v(V_0)N_v(\rho V_0) - J_v(\rho V_0)N_v(V_0)] \quad (2.12)$$

here, J_ν and N_ν are Bessel functions of the first and second kind, ν is the azimuthal order, m is the radial order, V_0 is the cut-off normalized frequency with: $V_0 = k_0 b \sqrt{n_{core}^2 - n_{clad}^2}$, where $\rho = b/a = (2\Lambda/\sqrt{3})/(d/2)$, $n_0 = n_{core}/n_{FSM}$ and the inner cladding radius $a = d/2$. Of particular interest is the numerical solution of Eq. (2.11) for the first higher-radial order HE₁₂ mode which provides the cut-off condition for mono-radial order guiding.

The numerical solution of Eqs (2.9 – 2.12) using the above analytical formalism are compared with the cut-off frequencies obtained from the exact FEM simulation in Fig. 2.2(b). In the FEM simulations, the cut-off condition of all the modes is quantitatively defined based on the optical power fraction (f_p) guided within the transverse region of interest (i.e. fiber core) as given by:

$$f_p = \frac{||[f(s_z)dA]_{core}||}{||[f(s_z)dA]_{total}||} \quad (2.13)$$

where S_z denotes the Poynting vector and the core area is bounded by ($0 \leq r \leq b$). Through an iterative study, a power fraction threshold of $f_p = 40\%$ within the core area was identified as the criterion for modal cut-off. Therefore, all physical modes numerically found with $f_p > 40\%$ are considered as core-guided in our analysis, while those modes whose power fraction is below threshold are systematically rejected (i.e. cut-off). Figure 2.10 shows exemplar profiles of eigenmodes supported by an AC-PCF that are exactly at cut-off ($f_p = 40\%$).

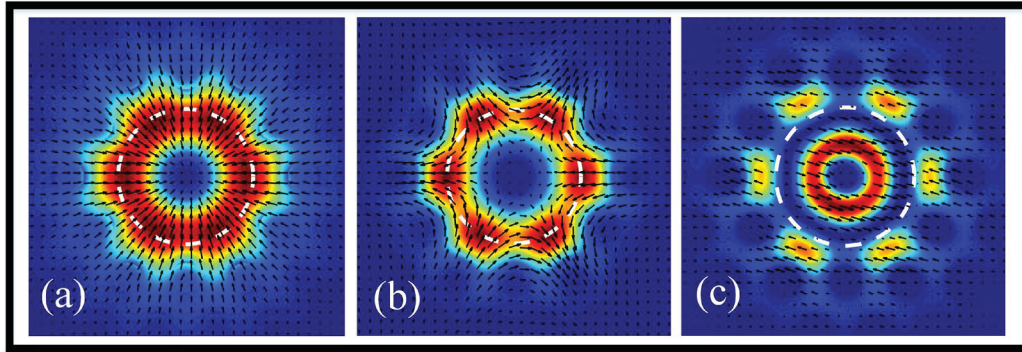


Figure 10. Profiles of (a) TM_{01} , (b) HE_{31} and (c) HE_{12} modes exactly at the modal cut-off threshold when $f_p = 40\%$ for an exemplar AC-PCF with $d/\Lambda = 0.5$ where the dashed white lines indicate the core region of interest of effective radius $b = 2\Lambda/3$

We have evaluated the modal purity of the $OAM_{\pm 11}$ beams generated in the Fiber 1 and Fiber 2 designs optimized for supercontinuum generation. To do so we performed the projection of the transverse field distribution $u(\rho, \theta)$ onto the “spiral harmonics” $\exp(-il\theta)$ where the variable l denote any l -th order OAM harmonic integer. We subsequently computed the energy C_l transmitted within each l -th OAM harmonic via (H. Li et al., 2016; Torner, Torres, & Carrasco, 2005):

$$C_l = \frac{1}{2\pi} \int_0^\infty \left| \int_0^{2\pi} u(\rho, \theta) \exp(-il\theta) d\theta \right|^2 \rho d\rho \quad (2.14)$$

Finally, the normalized power weight (P_l) for each l -th OAM harmonic (i.e. topological charge number) contained in the modal field under test is written as:

$$P_l = \frac{C_l}{\sum_{n=-\infty}^{\infty} C_n} \quad (2.15)$$

Figure 11(a) shows a typical “OAM spectrum” obtained using Eqs (2.14 and 2.15) and taking into account the harmonic ranges from $l = -10$ to $l = +10$ of the OAM_{-11} mode generated in Fiber 1 at 835 nm wavelength. The OAM spectrum indicates a very high (99%) $l = -1$ modal purity as expected, with residual peaks located at ± 6 charges about the main harmonic

ostensibly related to the six-fold symmetry of the photonic crystal structure. To verify that the high OAM mode purity is broadband, we computed in Fig. 2.11(b) the $OAM_{\pm 11}$ modes purities inside both optimized fibers within the range of simulated wavelengths from 600 to 1200 nm.

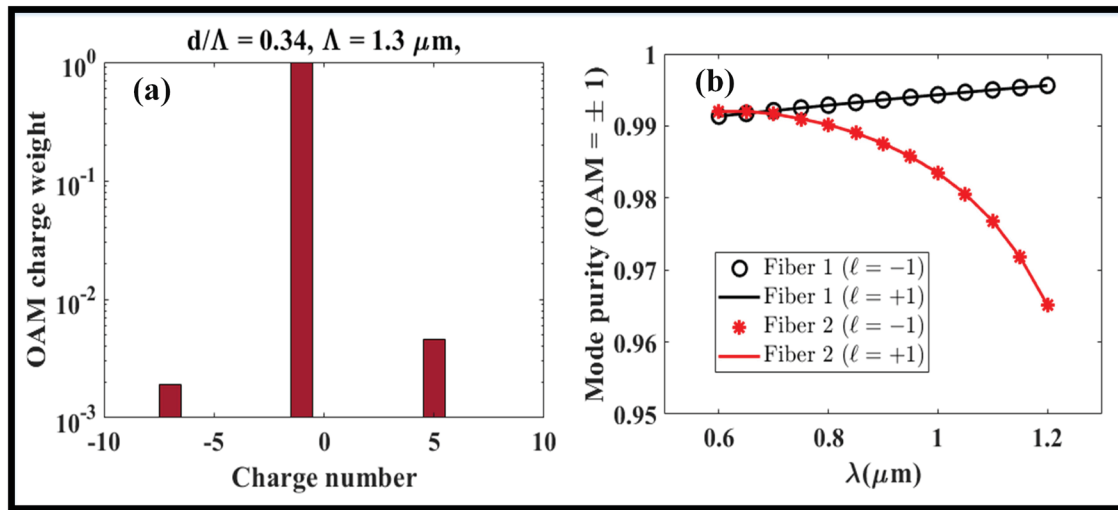


Figure 11. (a) OAM charge weights in Fiber 1 of generated OAM beam with topological charge ($\ell = -1$) at 835 nm (b) OAM mode purity as a function of wavelength for Fiber 1 and Fiber 2

One observes that the modal purity in Fiber 1 increases with the wavelength, while it decreases for Fiber 2. We attribute this behavior to the fact that Fiber 1 has a larger hole size ($0.442 \mu\text{m}$) compared to Fiber 2 ($0.1 \mu\text{m}$) such that modal confinement decreases with the wavelength in Fiber 2, whilst slightly improves in Fiber 1 for larger wavelengths. A similar relationship with the modal confinement was also observed for a different type of OAM fiber (H. Li et al., 2016).

CHAPTER 3

TRANSMISSION OF ORBITAL ANGULAR MOMENTUM AND CYLINDRICAL VECTOR BEAMS IN A LARGE-BANDWIDTH ANNULAR CORE PHOTONIC CRYSTAL FIBER

Manish Sharma ¹, Fatemeh Amirkhan ¹, Satyendra K. Mishra ¹, Dipankar Sengupta ¹, Younès Messaddeq ², François Blanchard ¹ and Bora Ung ¹

¹ Department of Electrical Engineering, École de technologie supérieure,
1100 Notre-Dame West, Montreal, Quebec, Canada H3C1K3

² Centre d'Optique, Photonique et Laser (COPL), Université Laval,
Québec, Canada G1V 0A6

Paper published in *Fibers*, April 2020

Résumé

Nous démontrons pour la première fois la propagation stable des faisceaux OAM et CVBs dans une fibre à cristal photonique avec un cœur annulaire (fibre conçue pour la transmission de faisceau d'ordre radial simple à large bande dans le régime de guidage dit « infiniment mono-radial »). Nous montrons que les faisceaux vectoriels-vortex peuvent maintenir des puretés de mode élevées supérieures à 18 dB après propagation dans la fibre. Ce test est fait sur toute la gamme de longueurs d'onde de 805 à 845 nm (plus de 17 THz de bande passante) à l'aide d'un laser accordable et une plaque spirale commerciale pour la génération de faisceaux vortex dans l'espace libre. Nos résultats confirment qu'une fibre à cristaux photoniques avec un cœur annulaire est un design prometteur pour la transmission à large bande de faisceaux vortex vectoriels qui ont des applications potentielles dans le multiplexage spatial, les communications quantiques, la détection optique et les pinces optiques.

3.1 Abstract

The stable propagation of orbital angular momentum and cylindrical vector beams in a newly designed annular core photonic crystal fiber (AC-PCF) tailored for the broadband single-radial order beam transmission (within the so-called “*endlessly mono-radial*” guiding regime) is demonstrated for the first time. It is shown that the vector-vortex beams can maintain high mode purities above 18 dB after propagation in the fiber under test over all of the wavelength range from 805 to 845 nm (over 17 THz bandwidth) investigated with the help of a tunable laser and an S -plate for the generation of singular beams in free space. Our results confirm that the AC-PCF is a promising design for the broadband transmission of vector-vortex beams that have potential applications in space-division multiplexing, quantum communications, optical sensing and trapping.

3.2 Introduction

We are still in the early stages of grasping the fundamental implications and applications of the vector-vortex beams. The so-called vortex beams carrying orbital angular momentum (OAM) harbor a phase singularity, while the cylindrical vector beams (CVB) present polarization singularities in their beam profiles (Allen et al., 1992; Yao & Padgett, 2011; Zhan, 2009). Conspicuously, both types of optical singularities lead to a beam recognized by a doughnut-shaped intensity profile. OAM beams can carry both spin and orbital angular momentum due to discrete states in circular polarization and helical phase (written as $\exp(iL\theta)$ where L is the topological charge and θ the azimuthal angle), respectively. Vortex beams have demonstrated promising advances in optical microscopy, optical trapping, space-division multiplexing, optical communications and for probing new (non)linear chiral light-matter interactions (Andersen et al., 2006; Bovino et al., 2011; Brullot et al., 2016; Padgett & Bowman, 2011; Ren et al., 2016; Schmiegelow et al., 2016; Willner et al., 2015; Yao & Padgett, 2011). Similarly, some CVBs (especially the radial TM_{01} and azimuthal TE_{01}

polarized beams) exhibit unique properties that enable novel light-matter interactions that can be exploited in super-resolution imaging, laser material processing and optical trapping, among others (Drevinskas et al., 2016; Kozawa, Matsunaga, & Sato, 2018; Kozawa & Sato, 2010; Youngworth & Brown, 2000; Zhan, 2009).

There is vigorous research being conducted to push the field further using both bulk optics and fiber-optic based platforms. Prior studies have demonstrated that fiber designs with a high-index annular core (i.e., “ring-core”) represent one of the most efficient approaches for the coupling and propagation of vector-vortex beams owing to the strong overlap between the beam’s optical intensity profile and the refractive index profile of the fibers (Brunet & Rusch, 2017; Brunet et al., 2015; Brunet, Vaity, et al., 2014; Gregg et al., 2015). Moreover, it was determined early on that suitable fiber designs must lift the modal degeneracy between the fiber eigenmodes in order to promote modal stability of CVB and OAM guided beams through lower crosstalk. The common rule to enable such stable transmission is to maintain intermodal refractive index separation of $\Delta n_{eff} \geq 10^{-4}$ between adjacent vector modes (Gregg et al., 2015; Siddharth Ramachandran et al., 2009). Solid annular-core fibers have shown interesting results (Brunet et al., 2015; Gregg et al., 2015) but have limitations in terms of achievable intermodal separations, chromatic dispersion and mode selection.

Microstructured fibers and photonic crystal fibers (PCF) in particular have recently attracted significant research interest towards alleviating the above limitations of solid-core fibers by exploiting the significantly increased design freedom afforded by the holey structure and the unique modal properties that emerge (Hu et al., 2016; Pakarzadeh & Sharif, 2019; Tandjè et al., 2018; Yue et al., 2012; Hu Zhang et al., 2017; L. Zhang et al., 2018). A particular design of annular-core photonic crystal fiber (AC-PCF) recently proposed the theoretical ability to enforce mono-radial vector-vortex mode guiding while preventing higher-radial order modes over a very large bandwidth (Sharma et al., 2019a). This unique waveguiding regime termed “*endlessly mono-radial*” (EMR) occurs when the periodic photonic crystal cladding has holes with a diameter (d) to pitch (Λ) ratio below a certain threshold: $d/\Lambda < 0.35$. Recently, Tandjè

et al. demonstrated vortex beam propagation inside a ring core photonic crystal fiber, although the latter fiber design was not EMR and the experimentally achieved OAM mode purities remained limited (Tandjè et al., 2019). In this work, the first experimental demonstration of both CVB and OAM beam transmission inside an endlessly mono-radial AC-PCF was performed. The stability of vector-vortex mode guiding in the AC-PCF was confirmed through polarimetric and interferometric measurements, which indicated good mode purity (>18 dB) over the whole 40 nm (17 THz) (limited by tunable laser operational range) bandwidth investigated with a near-infrared tunable laser.

3.3 Mode structure and attenuation in AC-PCF

The fabricated AC-PCF used in this work has a microstructure defined by air holes of average diameter ($d = 0.48 \mu\text{m}$) and separated by a periodic spacing of $\Lambda = 1.4 \mu\text{m}$ (scanning electron microscope (SEM) image of the cross-section is shown in Figure 3.1(a)), thus fulfilling the condition for operation in the “EMR” waveguiding regime ($d/\Lambda < 0.35$), where waveguiding is restricted to the following mono-radial modes: HE_{11} , TE_{01} , HE_{21} , TM_{01} , HE_{31} and EH_{11} .

To ensure the mono-radial operation of the few-mode fiber, it is critical to prevent excitation of the first bi-annular eigenmode (HE_{12}) of fiber, which occurs for $V \geq V_{cutoff} = 3.832$. Here, the V-parameter for the AC-PCF is defined as (Sharma et al., 2019a):

$$V = \frac{2\pi b}{\lambda} \left(\sqrt{n_{core}^2 - n_{FSM}^2} \right) \quad (3.1)$$

where b is the effective core radius, n_{core} is the refractive index of the solid glass material of the fiber (in this instance fused silica) and n_{FSM} denotes the effective refractive index of the so-called fundamental space-filling mode (n_{FSM}) in a triangular lattice of air-holes (Zhu & Brown, 2001). The effective core radius is given by $a = \frac{2\Lambda}{\sqrt{3}} = 1.62 \mu\text{m}$, as defined in (Sharma

et al., 2019a). The attenuation losses for the fundamental mode were measured in the wavelength range from 800 to 845 nm via the cutback method. The results in Figure 3.1(a) indicate average optical losses of around 0.5 dB/m inside the wavelength range of interest.

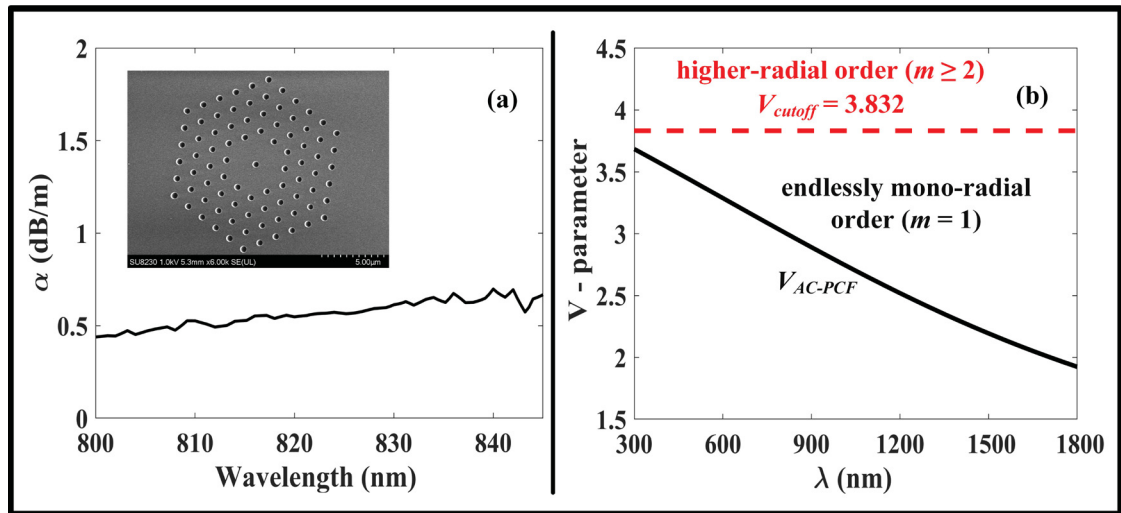


Figure 3.1 (a) Cutback losses of the used annular core photonic crystal fiber (AC-PCF), where the scanning electron microscope (SEM) image of the actual AC-PCF is shown in inset. (b) V -parameter of the AC-PCF as a function of the input wavelength in the 300–1800 nm range as calculated with finite-element method (FEM) simulations

Based on the specific geometry of our AC-PCF, full-vector finite-element method simulations of the V -parameter were performed [see Figure 3.1(b)], which confirmed that the fiber remains mono-radial ($V < V_{cutoff}$) irrespective of the input wavelength of excitation (i.e., operates in the EMR regime). We note that the simulations were only limited in practice on the UV end at 300 nm by the transmission window of the material, and not by a limitation of the EMR regime, which in theory applies for the whole electromagnetic spectrum.

3.4 Experimental setup and discussion

The experimental setup for the transmission and characterization of vector and vortex (CVB and OAM) beams is schematically depicted in Figure 3.2(a) and 3.2(b) respectively. Figure

3.2(a) shows the setup of OAM ($|L| = 1$) beam generation and launching, where the Gaussian beam from a tunable laser is collimated using objective lens and followed by a linear polarizer (LP) and a half-wave plate (HWP) for controlling the polarization orientation of the beam. Furthermore, the obtained linearly polarized beam passes through a quarter-wave plate (QWP), which converts the linear state to circular polarization state where the exact sign $s = \pm 1$ of circular polarization depends on the orientation of the incident linearly polarized light with respect to the QWP. Next, the *S*-Plate (i.e., space-variant radial polarization converter from Altechna (Sharma et al., 2019a)), designed for operating the wavelength of 815 (± 15) nm with more than 85% transmittance, is used to convert circular polarized light into the desired OAM vortex beam.

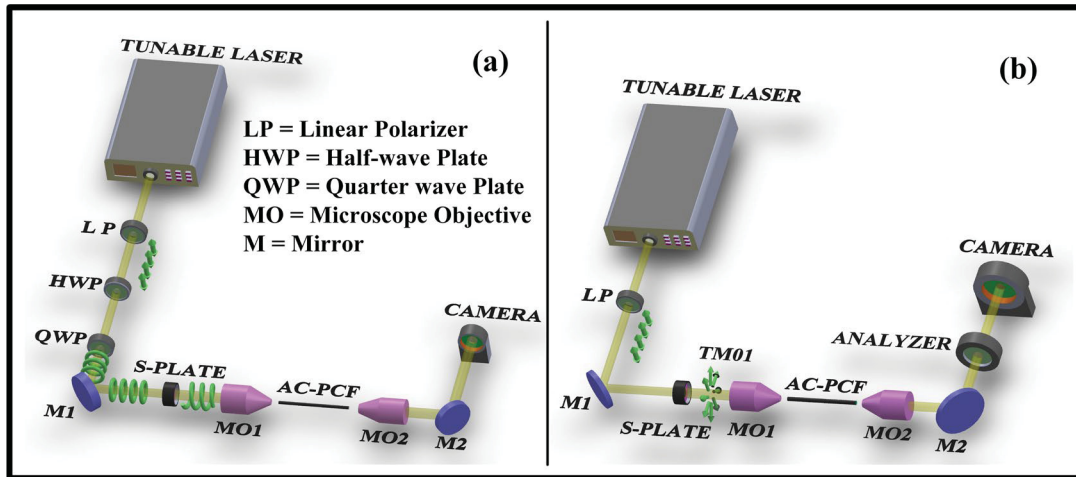


Figure 3.2 Experimental setup for launching and imaging (a) orbital angular momentum (OAM) beams and (b) cylindrical vector beams (CVB) (TE_{01} and TM_{01}) in the AC-PCF

Later, the obtained OAM ($|L| = +1$) beam is passed through a 20x and 0.4 NA microscope objective placed on a 6-axis stage in order to launch the vortex beam into the 3-meter long AC-PCF. Another 20x microscope objective lens is placed at the distal end of the fiber to collimate light before imaging on a CCD camera. Figure 3.2(b) shows that the experimental setup for the preparation of CVBs is very similar to that of Figure 3.2(a), with the exception that linearly polarized light is launched on the *S*-Plate (as opposed to circularly polarized) in

order to generate TE_{01} and TM_{01} beams depending on the orientation of linear polarization with respect to the optical axis of the S -Plate. Hence, polarization parallel to the axis of S -Plate gives TE_{01} while a perpendicular orientation result in a TM_{01} beam. Finally, a linear polarizer (i.e., analyzer) is placed between the fiber output and the charge-coupled device (CCD) camera for subsequent vector beam identification [see Figure 3.3].

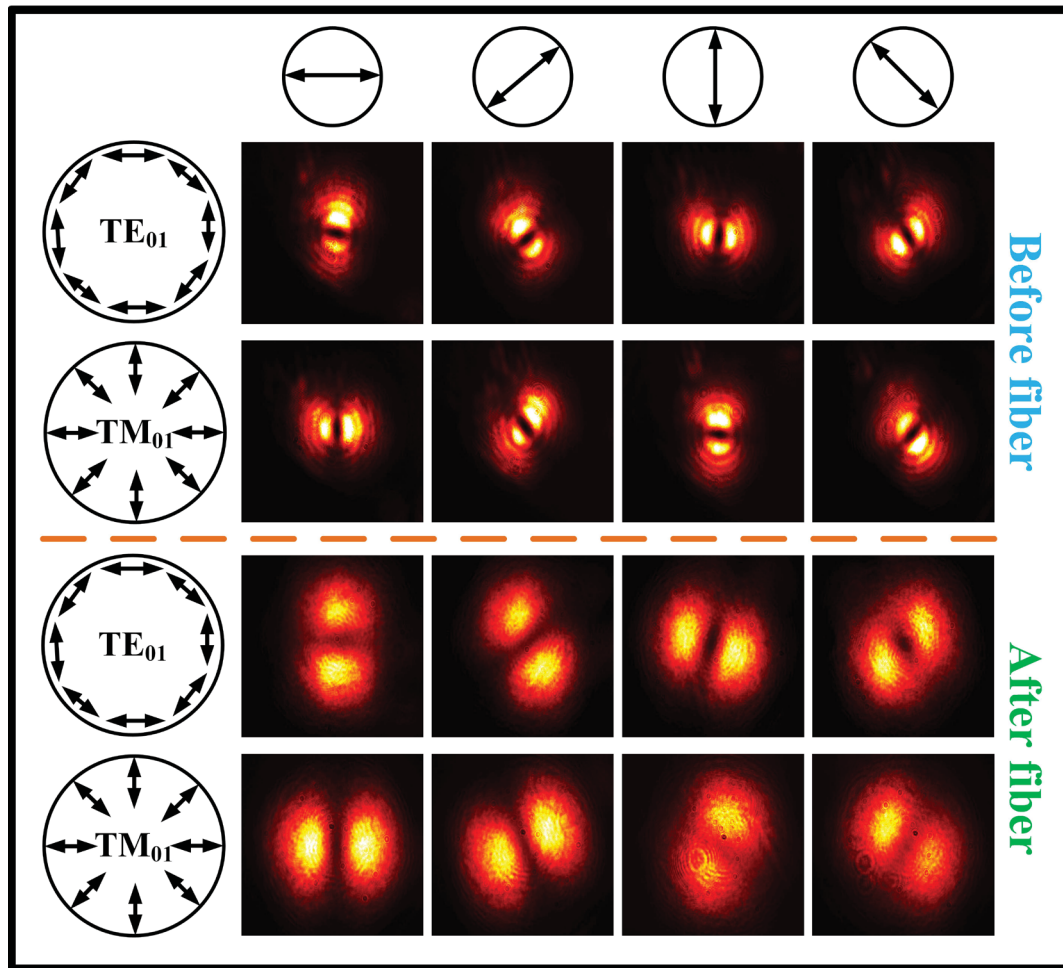


Figure 3.3 Experimental identification of the obtained CVBs (radial TM_{01} and azimuthal TE_{01}) before (top two rows) and after propagation in the AC-PCF (bottom two rows) through rotation of the analyzer positioned in front of the CCD camera

The CVB and OAM beam propagation in the AC-PCF is characterized by analyzing their respective intensity profiles at the distal end of the fiber. This was followed by the evaluation

of the achieved mode purity after propagation through the fiber. Figure 3.3 displays the intensity pattern of CVBs imaged after a rotating analyzer used for mode identification of the actual CVB (TE_{01} or TM_{01}) at hand. The first column in Figure 3.3 presents a schematic representation of the electric field distribution inside the azimuthally polarized (TE_{01}) and radially polarized (TM_{01}) beams, while the top row indicates the state of rotation angle of the analyzer. By monitoring the intensity profiles of the beams passing through the analyzer (Rows 2–5) with respect to the rotation state of the analyzer, one can identify the type of CVB beam under test (Pradhan et al., 2018).

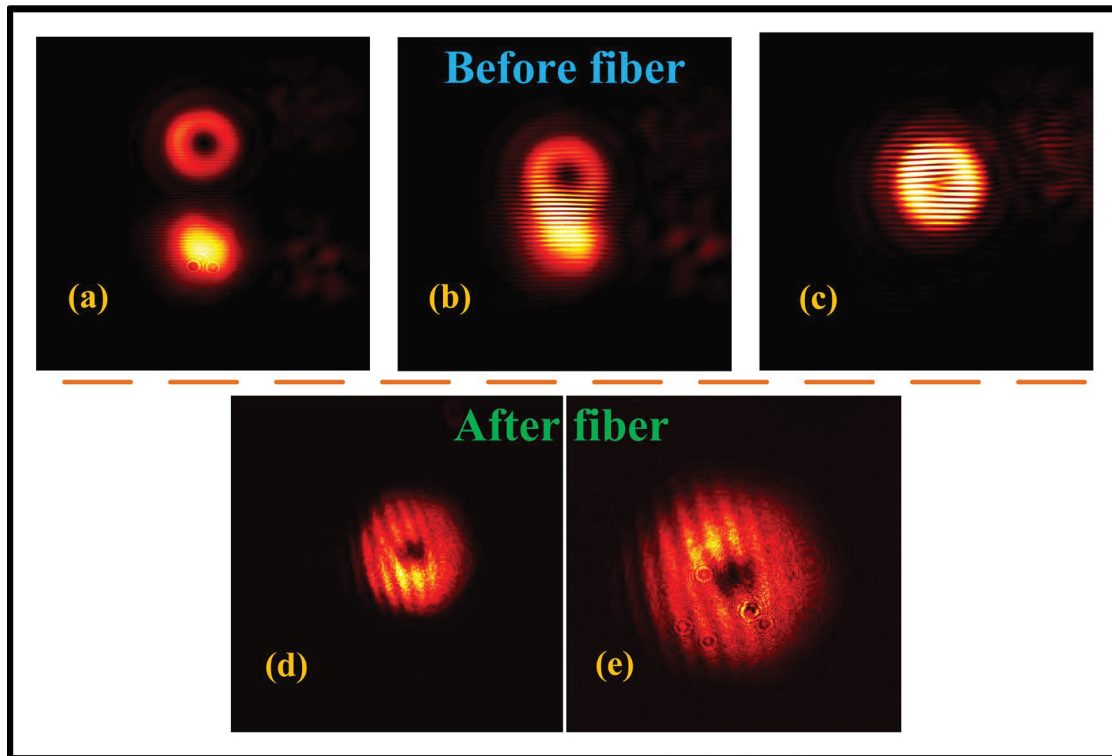


Figure 3.4 (a,b,c) Interference pattern of a $L = +1$ doughnut-shaped OAM beam with a reference Gaussian beam as they progressively merge to generate a single fork pattern before (Top row) and (d,e) after propagation in the fiber (Bottom row)

The intensity profiles in the second and third rows of Figure 3.3 were recorded immediately after the *S*-Plate and before fiber launching. The fourth and fifth rows of Figure 3.3 subsequently display the beam intensity profiles after propagation in the three-meter long

AC-PCF. The latter images indicate that the output (TM_{01} and TE_{01}) CV beams retained their polarization after propagation through the AC-PCF. Figure 3.4(a,b,c) displays the intensity profiles of a vortex and a reference Gaussian beam as they are gradually superposed to create the single fork pattern expected for the interference of a $L = +1$ helically-phased OAM beam with a tilted reference beam of constant phase front (Gecevicius et al., 2018; Hongwei Zhang et al., 2019). Similarly, Figure 3.4(d,e) shows a similar fork interference pattern created by the superposition of a reference Gaussian beam and the vortex beam output from the AC-PCF. More details about the experimental setup and procedure to achieve the interferograms in Figure 3.4 are provided in the Appendix. We further note that, prior to our experimental investigation, we measured the laser light coupling efficiency into the AC-PCF for the Gaussian and the vector-vortex beams as 58% and 44%, respectively. The smaller coupling efficiency of vector-vortex beams is due to the slightly larger input beam diameter (full width at half maximum diameter = $3.81\mu\text{m}$) of the vector-vortex beams at focus compared to the effective core diameter ($2b = 3.24\mu\text{m}$) of the AC-PCF. The full width at half maximum (FWHM) diameter of our vector-vortex beams was measured at focus of 20x microscope objected via the knife-edge method (Siegman, Sasnett, & Johnston, 1991) using a sharp atomic force microscope (AFM) tip scanned across the doughnut shaped beam in steps of 0.65 micrometer (via a three-axis micro-positioning stage) along the transverse direction.

The vortex beam purity was assessed over the whole investigated wavelength range by scanning the single-frequency tunable diode laser (TOPTICA Photonics DL Pro) from 805 nm to 845 nm (the investigation wavelength range was limited by operational range of tunable laser) in steps of 1 nm. The corresponding intensity images of the transmitted OAM beams were then used for evaluating the modal purity (uniform intensity profile) based on the azimuthal intensity distribution along the annular beam [more details on the method used for calculating the vortex mode purity is provided in the appendix]. Figure 3.5 presents the calculated vortex mode purities in dB units as a function of wavelength.

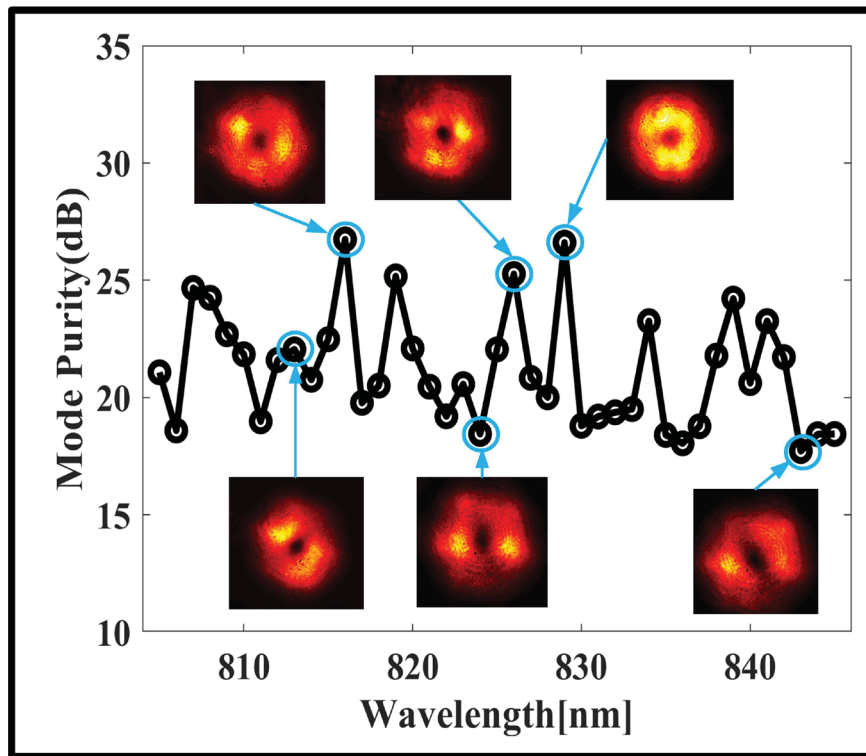


Figure 3.5 Mode purity of OAM beam at fiber output as a function of wavelength (from 805 to 845 nm in step on 1 nm using tunable laser), Inset: output beam images for selected wavelengths

The results show that the mode purity varies between 18 and 26 dB, which confirm that good modal purity of vortex modes can be achieved in the fabricated AC-PCF and as can be seen in the sampled intensity profiles shown in Figure 3.5.

3.5 Conclusion

In summary, we experimentally demonstrated, for first time, the stable transmission of single radial order singular beams—both polarization cylindrical vector beams (CVB) and the orbital angular momentum (OAM) phase vortex beams—inside a newly designed endlessly mono-radial annular-core photonic crystal fiber (AC-PCF) with sub-micron holey cladding features (Sharma et al., 2019a). The singular beams (OAM and CVBs) were prepared in free space using an *S*-waveplate and launched in the AC-PCF. Good singular beam purity (up to 26 dB) was demonstrated at the fiber output over the whole investigated wavelength range (805 to 845 nm), spanning a 17 THz bandwidth. This work is another step in the research towards the stable and broadband transmission of singular vector-vortex beams in tailored photonic crystal fibers, and particularly, in designs analogous to the AC-PCF. The results are relevant to applications in space-division multiplexing, quantum communication, sensing via structured light and optical manipulation.

Contributions:

M.S. and B.U. contributed to the optical fiber design and co-wrote the manuscript. M.S., F.A. and F.B. participated in the experimental demonstration. Y.M. contributed in the fabrication of the fiber. B.U. and F.B. provided primary supervision of the work. All authors contributed to the analysis of the data. All authors have read and agreed to the published version of the manuscript.

3.6 Appendix

Experimental setup for generating the fork interferogram pattern of vortex beams

Figure 3.6 shows the schematic of the experimental scheme used for identifying the topological sign and number ($L = \pm 1$) of the transmitted vortex beam through the creation of an interference pattern with a Gaussian reference beam on the recording camera. The reference Gaussian beam is obtained by placing a Wollaston prism that separates incident light into two linearly polarized light beams that become circularly polarized upon passing through the quarter-wave plate (QWP). One of the ensuing beams is then directed towards the *S*-Plate to generate the desired $L = +1$ OAM vortex beam.

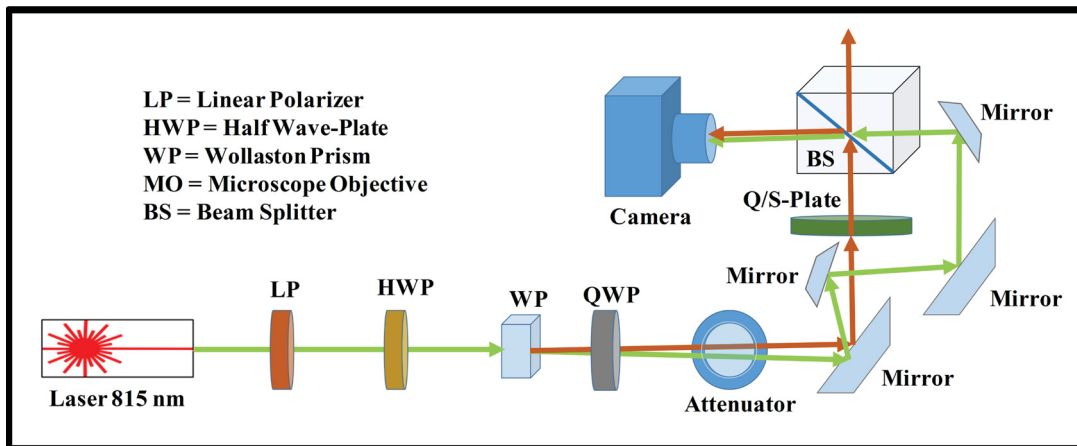


Figure 3.6 Experimental setup for recording the interference pattern of the Gaussian beam (path identified in green) and the vortex OAM beam (path identified in red) on the CCD camera

Further, both OAM and Gaussian beams are then combined using a beams splitter before the corresponding interference pattern can be observed and recorded on the CCD camera. We note that the two interfering beams were progressively brought closer to each other by controlling the orientation of the last three mirrors in the optical path. This setup was modified to allow the insertion of the fiber between the *S*-plate and beam splitter (BS) in the OAM beam optical path, so as to enable the characterization of the ensuing fork

interferogram after propagation through the AC-PCF under test (in the bottom row of Figure 3.4).

Mode purity method

To estimate the purity or quality of OAM beam after propagation through fiber in our experimental setup, we used mode purity measurement method based on the variation in azimuthal intensity pattern of optical vortices as performed in (Bozinovic, Kristensen, et al., 2011) where the normalized intensity variation (i.e., the “visibility”) along the azimuthal direction is defined as:

$$V = \frac{I_{max} - I_{min}}{I_{max} + I_{min}} \quad (3.2)$$

Here I_{max} and I_{min} are the maximum and minimum intensities of the beam along the scanned azimuthal direction. The visibility (V) is then used for evaluating the mode purity as:

$$\text{Mode purity (dB)} = 10 \log_{10} \left(\frac{1 + \sqrt{1 - V}}{V} \right)^2 \quad (3.3)$$

Figure 3.7 depicts the azimuthal intensity distribution (along the dotted black lines) of a typical $L = +1$ vortex beam generated at 821 nm wavelength with our experimental setup. In sub figure, the procedure for scanning intensity distribution along azimuthal orientation is demonstrated, where black dash line (circle with one given radius) on top of red color intensity image display line for scanned intensity data in 360 degrees. This one-dimensional intensity data gives I_{max} and I_{min} values, that are used in estimating V visibility parameter. Finally, equation 3.3 gives mode purity values in dB units. We note that similar mode purity measurements were performed for the entire investigated wavelength range from 805 to 845 nm.

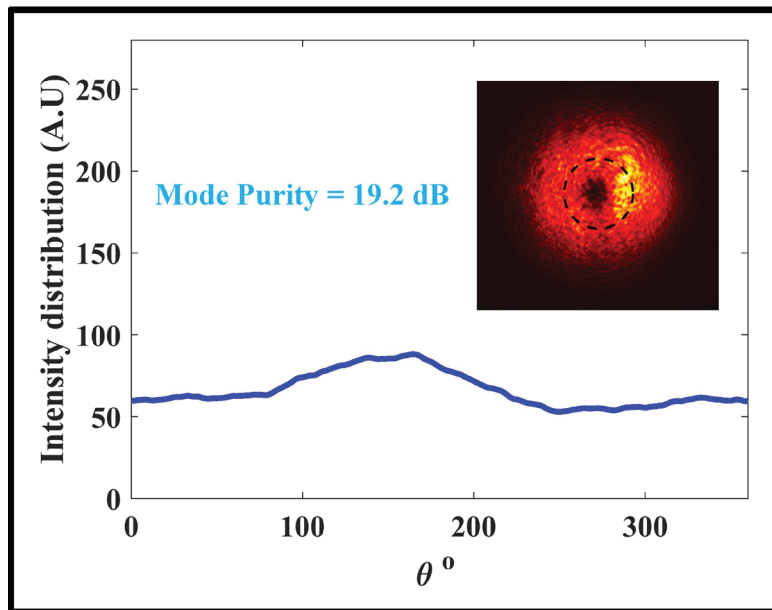


Figure 3.7 Azimuthal Intensity distribution of a typical vortex OAM beam at 821 nm (inset image of OAM with azimuthal ring)

CHAPTER 4

RADIALLY ANISOTROPIC RING-CORE OPTICAL FIBER: TOWARDS VECTOR-VORTEX GUIDED TRANSMISSION USING THE FULL MODAL SPACE

Manish Sharma¹, Dhasarathan Vigneswaran², Sophie LaRochelle³, Leslie A. Rusch³ and Bora Ung^{1, *}

- ¹ Department of Electrical Engineering, École de technologie supérieure, 1100 Notre-Dame West, Montreal, Quebec, Canada H3C1K3
- ² Dept. of Physics, University College of Engineering, Ramanathapuram Campus, Tamilnadu, India
- ³ Centre d'Optique, Photonique et Laser (COPL), Université Laval, Québec, Canada G1V 0A6

Paper published in *OSA Continuum*, April 2021

Résumé

La fibre avec un cœur annulaire radialement anisotrope (avec biréfringence cylindrique) est étudiée théoriquement et numériquement comme une nouvelle plate-forme pour la transmission de faisceaux vectoriels-vortex avec des propriétés uniques. Nous montrons tout d'abord les conditions paramétriques selon lesquelles la fibre permet une substitution modale du mode azimutal TE_{01} (ou radial TM_{01}) en remplacement du mode conventionnel HE_{11} de type gaussien, en tant que mode fondamental de la fibre. Nous démontrons aussi qu'il est possible de modifier significativement les propriétés de guidage de l'onde dans la fibre via l'addition d'une petite biréfringence radiale ($\sim 10^{-4}$) de manière à causer la dégénérescence des modes TE_{0m} et TM_{0m} . Cette dernière propriété est exploitée pour créer des faisceaux vortex stables et de haute pureté ($>99\%$) par la combinaison cohérentes des modes TE/TM sans affecter les modes hybrides HE/EH; une propriété non possible avec des fibres standards. Ces nouveaux résultats sont pertinents pour les domaines du multiplexage par répartition modale, la lumière structurée, la modélisation et fabrication de fibres optiques spéciales.

4.1 Abstract

The radially anisotropic ring-core fiber with cylindrical birefringence is theoretically and numerically investigated as a novel platform for the transmission of vector-vortex beams with unique modal properties. First, we elucidate the parametric conditions where such fiber enables *modal substitution* in which either the doughnut-shaped azimuthal TE_{01} or radial TM_{01} mode replaces the normal Gaussian-like HE_{11} mode as the fundamental mode of the waveguide. We also demonstrate that it is possible to significantly engineer the waveguiding properties of the fiber via the addition of small radial birefringence ($\sim 10^{-4}$) so as to make the (hitherto non-degenerate) TE_{0m} and TM_{0m} modes fully *degenerate*. The latter property is used to create stable vortex modes of high purity (>99%) with the newly degenerate modal pair – a feat not possible with standard few-mode fibers – all without affecting the co-propagating hybrid HE/EH modes that remain available as an independent basis set to produce vortex beams of similarly high purity. These new insights are relevant to the topical fields of mode-division multiplexing, structured light, fiber modelling and fabrication.

4.2 Introduction

Radially anisotropic fibers are a special class of optical fibers, first studied by Black et al., where the fiber displays cylindrical birefringence (Black, Veilleux, Bures, & Lapierre, 1985). Their theoretical analysis distinctively showed that a radially anisotropic optical fiber could be designed such as to have the fundamental mode to be either the azimuthal TE_{01} or radial TM_{01} mode instead of the usual linearly polarized HE_{11} mode (Black et al., 1985). Such fiber exhibits polar anisotropy, aka cylindrical material birefringence, where either the fiber core or cladding demonstrates different material refractive indices along the radial and azimuthal directions in polar coordinates (Black et al., 1985; S. H. Chen & Chen, 1994; T.-J. Chen & Chen, 1995; Yijiang, 1987). This approach also opens the possibility to enhance one's control over the selective excitation and modal separation of the radial and azimuthal (TE_{0m}

and TM_{0m}) families of guided modes in such fibers (Black et al., 1985; S. H. Chen & Chen, 1994). Furthermore, ring-core fibers have shown to not only be a favorable structure for high-order mode guiding in radially anisotropic fibers (Black et al., 1985; Y. Chen, 1991), but was also more recently actively studied for the stable transmission of vector as well as vortex beams (that carry orbital angular momentum (OAM)) owing to their ability to lift the near modal degeneracy between adjacent eigenmodes (Siddharth Ramachandran et al., 2009). Hence, radially anisotropic fibers with a ring-core structure offer a promising platform for studying structured light beams, which lends to further investigation.

Potential approaches towards the experimental demonstration of such anisotropic fibers include by means of liquid crystal structures (Ertman et al., 2018), and more recently, metamaterial based optical fibers (Pollock et al., 2016; Pratap et al., 2018; Pratap et al., 2015). These metamaterial based anisotropic optical fibers, have spurred new opportunities for research with possible applications in space-division multiplexing where, as we will show here, the fiber's radial anisotropy could be tailored so as to enable a richer variety of co-propagating vector-vortex modes compared to conventional isotropic fibers. Aside from niche applications in radial/azimuthal polarized laser delivery and endoscopic imaging, the TE_{0m} and TM_{0m} vector modes of optical fibers have mostly been neglected in other areas such as optical communications where they are traditionally seen as sources of noise (via modal crosstalk) and loss rather than potential information channels. One important reason is that the TE_{0m} and TM_{0m} modes in classical isotropic fibers are not degenerate and thus cannot form a stable OAM mode basis set (Dashti et al., 2006).

In this work, we propose and investigate the cylindrically anisotropic ring-core fiber design for the stable transmission of vector-vortex beams by means of a combination of either degenerate radially (TM_{0m}) and azimuthally (TE_{0m}) polarized vector modes, or the hybrid (HE / EH) modes. A full-vector finite element method-based fiber model was developed and studied with perfectly matched layer outer boundary conditions. Further, we evaluated the mode purity and intermodal refractive index separation of the resulting OAM modes. Finally,

we elucidate the waveguiding regimes where the proposed fiber can guide either the radially or azimuthally polarized vector mode as the fundamental mode.

4.3 Fiber design parameters

In circular core optical fibers, it is generally known that vortex beams can be formed by the coherent superposition of $\pm \frac{\pi}{2}$ phase-shifted degenerate high-order hybrid modes:

$$CV_{\pm\ell,m}^{\pm} = HE_{\ell+1,m}^e \mp iHE_{\ell+1,m}^o \quad (4.1a)$$

$$CV_{\pm\ell,m}^{\mp} = EH_{\ell-1,m}^e \mp iEH_{\ell-1,m}^o \quad (4.1b)$$

Here, CV stands for “circular vortex” and ℓ represents the azimuthal number (or topological charge) of the corresponding OAM mode (Snyder & Love, 2012).

Vortex beams can additionally be created via a similar combination of the $\pm \frac{\pi}{2}$ phase-shifted azimuthally/radially polarized TE_{0m} and TM_{0m} modes (Dashti et al., 2006; Sharma, Pradhan, & Ung, 2019b) via :

$$UV_{\pm\ell,m}^{\mp} = TM_{0,m} \mp iTE_{0,m} \quad (4.2)$$

Because the TE_{0m} and TM_{0m} modes are normally non-degenerate in common isotropic circular optical fibers, the resulting OAM mode are known to be unstable vortices (UV) that quickly decays upon propagation in optical fiber (Dashti et al., 2006). Mode-division multiplexing (MDM) in cylindrical few-mode fibers (FMF) can be supported through either the well-known linearly polarized (LP) mode basis set or the stable vortex mode basis set described above. For a given normalized V-parameter value, let's say $V = 3$ without loss of generality, the FMF can in theory support a greater number of independent LP modes ($LP_{01}^{x,y}$, $LP_{11a}^{x,y}$, $LP_{11b}^{x,y}$; total of 6 polarization mode channels) when compared to the vortex basis set: $CV_{\pm 01}^{\pm}$ and $CV_{\pm 11}^{\pm}$ (total of 4 polarization mode channels). However in practice, the near degeneracies in modal and polarization distribution tend to couple the high-order even “a”

and odd “b” LP modes that result in significant crosstalk. The latter issue can be resolved using special polarization-maintaining FMs that enable to lift these degeneracies so as to fully exploit the LP mode basis set (Corsi et al., 2020; Wang et al., 2017).

In this work, we show that it is possible to resolve the phase mismatch between the TE_{0m} and TM_{0m} modes so as to make them degenerate by adding a small level of radial birefringence (i.e. radial anisotropy) in the high-index ring shaped core, all without affecting the remaining HE/EH hybrid modes. Such degenerate TE/TM modes then become available to complete the full vortex mode basis set [Eq. (4.2)] that can be utilized in MDM applications or otherwise. Figure 4.1 shows a schematic diagram for the refractive index profile of the proposed radially anisotropic ring-core fiber, with a and b denoting the inner and outer core radii respectively, with their ratio defined as $\rho = \frac{a}{b}$.

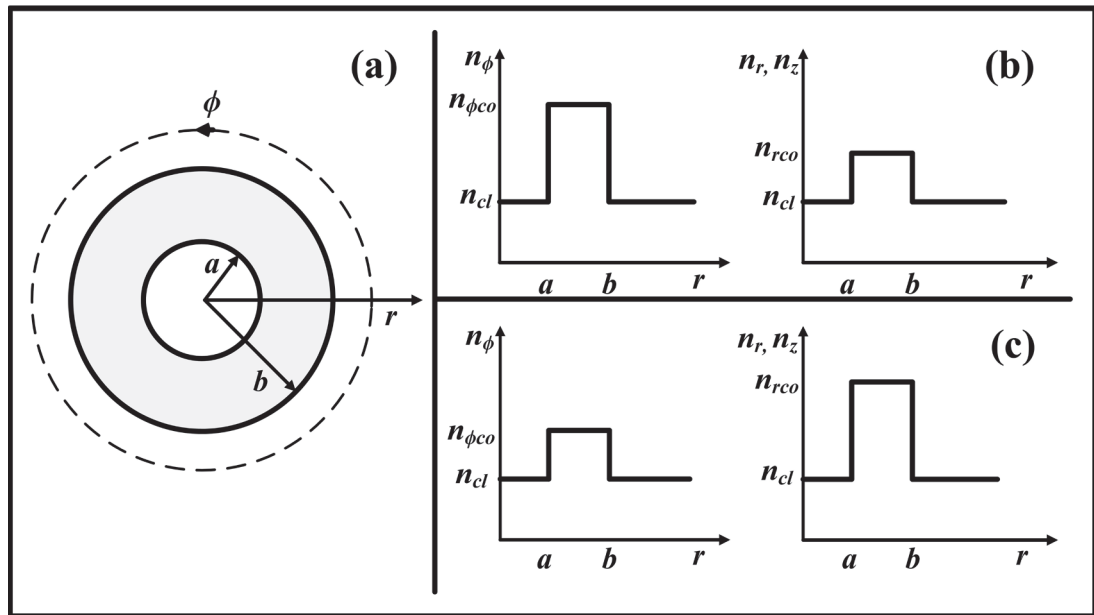


Figure 4.1. Schematic diagram of the anisotropic ring-core fiber showing the radial and azimuthal axes along which the refractive index profile is defined (n_r & n_ϕ), and for two general cases of core anisotropy (b) $n_\phi > n_r$ and (c) $n_\phi < n_r$

The birefringence in the fiber is defined along the two principal axes in polar coordinates (n_r, n_ϕ) while the axial refractive index was here taken as $n_z = n_r$ as was similarly done in

(Y. Chen, 1991). We note that the effect of the axial component (n_z) is negligible since the magnitude of the transverse guided fields (E_r, E_ϕ) remained dominant compared to the longitudinal field (E_z) in our FEM simulations. In this study we assumed the inner and outer cladding material to be isotropic fused silica with a refractive index of $n_{\phi cl} = n_{rcl} = n_{cl} = 1.444$ at 1550 nm wavelength (used throughout this study) while the effect of the radial and azimuthal components of the core refractive index ($n_{rco}, n_{\phi co}$) was numerically investigated for values ranging from 1.450 to 1.500 with steps of 0.005. The latter fiber parameters yield a maximum core-cladding refractive index contrast of $\Delta n = 0.056$ that is close to practical attainable values reported in doped-core fused silica glass (Ung, Vaity, et al., 2014).

The fiber design parameters considered for this study have a core inner radius $a = 1$ μm and outer radius $b = 4$ μm giving an aspect ratio of $\rho = 0.25$. This aspect ratio was selected so that it is thin enough to have significant modal separation ($>10^{-5}$) between adjacent vortex modes; but not too thin so as to become impractical to fabricate or to couple light. All while exhibiting modal cutoff properties that remain practically unchanged from a standard step-index fiber as was demonstrated for the isotropic ring-core fiber (Brunet, Ung, et al., 2014).

In order to make our analysis more general we also define two relative parameters, $\Delta_r = \frac{n_{rco}^2 - n_{cl}^2}{2n_{cl}^2}$ and $\Delta_\phi = \frac{n_{\phi co}^2 - n_{cl}^2}{2n_{cl}^2}$, that respectively denote the core's radial refractive index contrast and azimuthal refractive index contrast.

4.4 Results and discussion

We investigated the modal properties of the first two mode families (LP_{01} and LP_{11}) in the proposed radially anisotropic ring-core fibers for a range of absolute core refractive indices, $1.45 \leq n_{rco} \leq 1.50$ and $1.45 \leq n_{\phi co} \leq 1.50$, which translate into the following range of normalized refractive index contrasts: $0.42 \times 10^{-2} \leq \Delta_r \leq 3.9 \times 10^{-2}$ and $0.42 \times 10^{-2} \leq \Delta_\phi \leq 3.9 \times 10^{-2}$. The simulation results in Fig. 4.2(a) [and Fig. 4.2(c)] show that the

value of effective refractive index (n_{eff}) for the fundamental HE_{11} mode [and the HE_{21} mode] increases with both the Δ_r and Δ_ϕ refractive index contrasts. We note that the black dash line in all subfigures highlights the reference case when the fiber is isotropic: $\Delta_r = \Delta_\phi$.

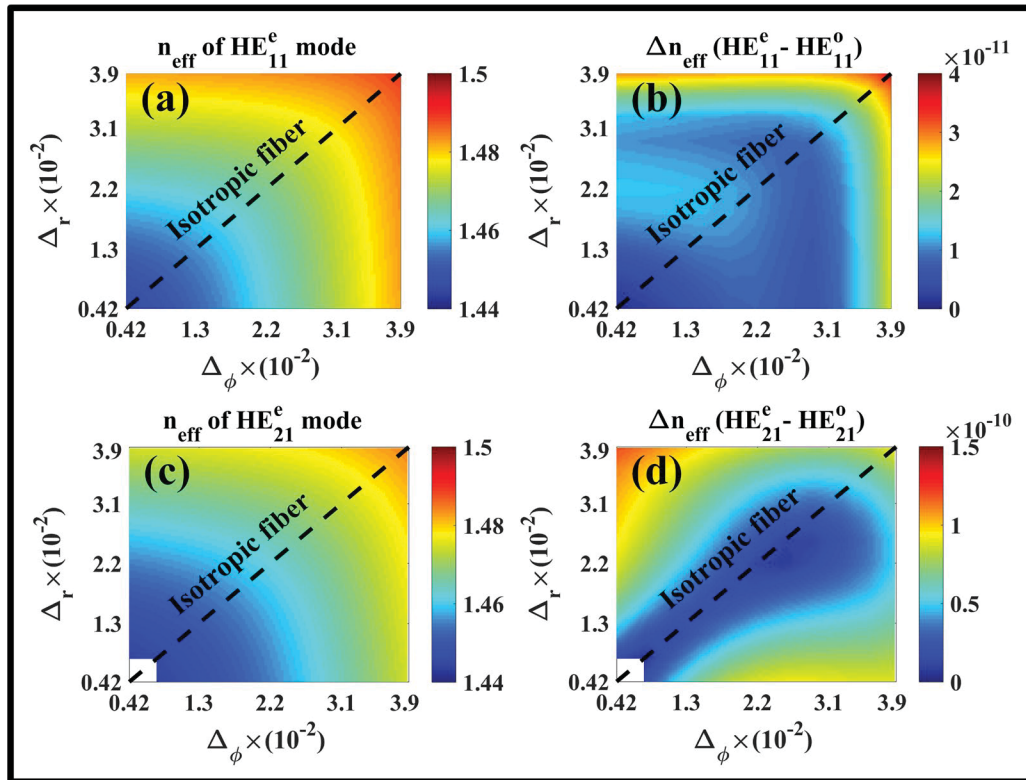


Figure 4.2. (a) Effective index (n_{eff}) of the HE_{11}^e and (c) HE_{21}^e modes, while (b) effective index separation (Δn_{eff}) between HE_{11}^e and HE_{11}^o and (d) HE_{21}^e and HE_{21}^o modes

Figure 4.2(b) shows the difference in the modal indices of the even and odd HE_{11} modes, which indicates that the HE_{11} mode retains a pure polarization degeneracy despite the significant radial birefringence (up to 3.9%) introduced in the fiber. A similar behavior is shown in Fig. 4.2(d) for the even and odd HE_{21} modes. The reason for this sustained degeneracy is because the hybrid HE/EH modes have a completely mixed polarization such that their even and odd states have evenly distributed E-field components in both the radial and azimuthal directions. The latter behavior may be desirable in several applications - including for optical communications - where a perfectly polarization-degenerate fundamental HE_{11} mode is useful. Importantly, it also suggests that vortex modes created via

the coherent superposition of the HE/EH hybrid modes [in Eq. (4.1)] still remain possible and unaffected by the addition of radial birefringence in the fiber.

Figure 4.3(a)-(b) show the effective refractive index of the TM_{01} and TE_{01} modes as a function of the core relative index contrast in the radial (Δ_r) and azimuthal (Δ_ϕ) directions. As expected, we see in Fig. 4.3(a) that the TM_{01} mode with radial polarization ($E_r, 0$) depends only on changes in Δ_r , while in Fig. 3(b) we observe the reverse behavior: the azimuthally polarized TE_{01} mode ($0, E_\phi$) solely depends on Δ_ϕ .

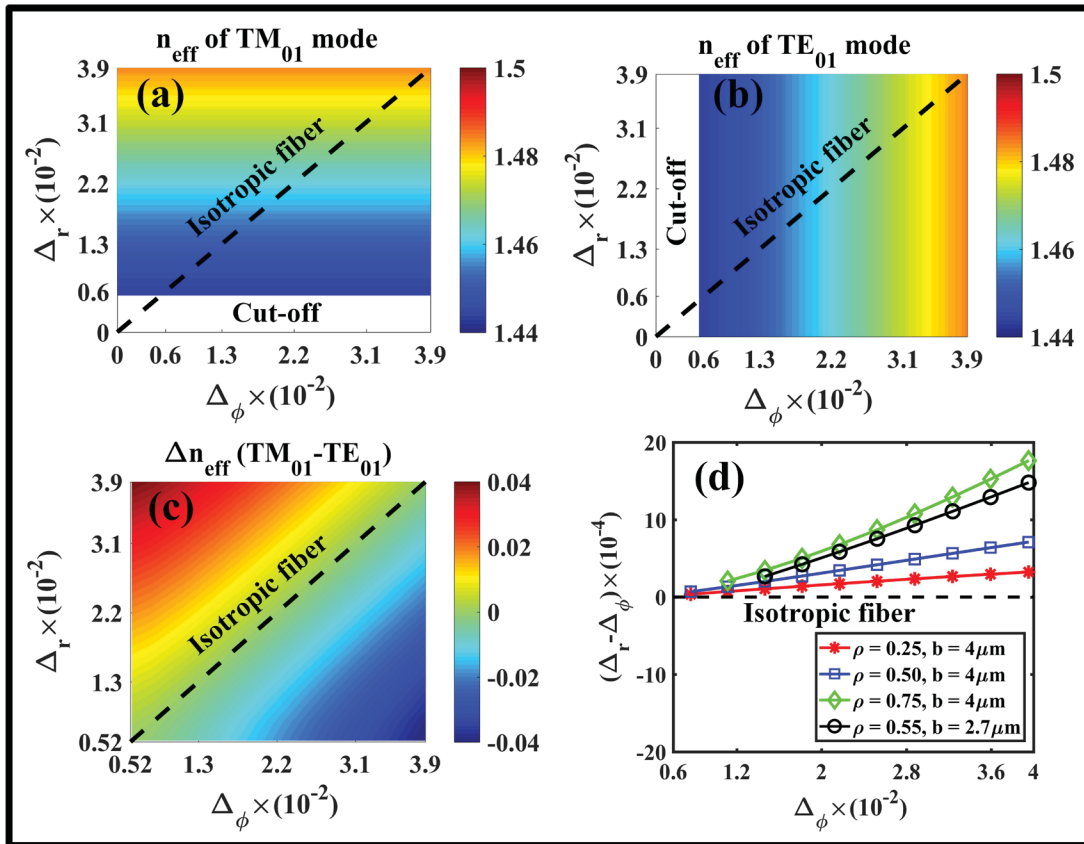


Figure 4.3. (a) Effective index (n_{eff}) of the TM_{01} and (b) TE_{01} mode (c) Effective index separation (Δn_{eff}) between TM_{01} and TE_{01} (d) Anisotropic fiber condition for degeneracy ($\Delta n_{eff} (TM_{01} - TE_{01}) < 10^{-10}$) of radially and azimuthally polarized mode propagation for

four different fibers (with $\rho = 0.25, 0.50, 0.75$ and $b = 4 \mu\text{m}$ as well as $\rho = 0.55$ and $b = 2.7 \mu\text{m}$) based on FEM calculation

Here we note that simulations are performed for a range of relative core index contrasts of Δ_r or $\Delta_\phi \geq 0.53 \times 10^{-2}$, because the cut-off limit for the TE_{01} , / TM_{01} mode was found to be $\Delta_{r/\phi} \approx 0.53 \times 10^{-2}$. We also confirmed that the latter cut-off values are validated with a theory of ring-core fibers based on the exact solution of Maxwell equations and using the dimensionless V-parameter (Brunet, Ung, et al., 2014).

For a radially anisotropic ring-core fiber this parameter must be defined separately for TM modes as $V_{TM} = (2\pi b/\lambda) \left(\sqrt{n_{rco}^2 - n_{cl}^2} \right)$, and for TE modes: $V_{TE} = (2\pi b/\lambda) \left(\sqrt{n_{\phi co}^2 - n_{cl}^2} \right)$. Through this formalism we numerically found, as expected, the cut-off condition for both the TE_{01} and TM_{01} modes as $V_{cut(r,\phi)} = 2.412$, a value that is in very close quantitative agreement with a similar isotropic ring-core fiber of ratio $\rho = 0.25$ (Brunet, Ung, et al., 2014). Owing to their mixed E-field polarization distribution, the definition of the V-parameter for the HE/EH hybrid modes, $V_{HE/EH} = (2\pi b/\lambda) \left(\sqrt{\bar{n}_{co}^2 - \bar{n}_{cl}^2} \right)$, depends on the transverse areal average of the radial and azimuthal indices, $\bar{n}_i = \int_i (n_r + n_\phi) r d\phi dr / \left[2 \int_i r d\phi dr \right]$, inside the respective core and cladding regions ($i = \{co, cl\}$). One can then readily determine the corresponding cut-off conditions of the high-order HE/EH hybrid modes using the exact relations derived for the isotropic ring-core fiber (Brunet, Ung, et al., 2014).

One of the prime objectives of the current study is to find a fiber design that enables the TE_{01} and TM_{01} modes to become degenerate so as to form stable OAM modes via Eq. (4.2). Figure 4.3(c) displays the effective refractive index separation (Δn_{eff}) between TE_{01} and TM_{01} mode within the fiber design space. The latter plot allows to identify fiber parameters for which the condition of TE/TM modal degeneracy occurs: $\Delta n_{eff} < 10^{-10}$. On inspection

of Fig. 4.3(c) one realizes that the condition for TE/TM modal degeneracy ($\Delta n_{eff} \rightarrow 0$) is found in proximity to the normal isotropic fiber case. A zoom-in on the region of interest [Fig. 4.3(d)] indicates that TE/TM modal degeneracy can effectively be obtained when $\Delta_r > \Delta_\phi$ and that only a small amount of radial birefringence ($\Delta_r \sim 10^{-4}$) is required, and increases quasi-linearly with the core-cladding refractive index contrast of the fiber. Here we also investigated the effect the core's aspect ratio ρ on the radial birefringence for $\rho = 0.25, 0.50, 0.75$ and $b = 4 \text{ um}$ as shown in Fig. 4.3(d). Figure 4.3(d) also includes the fiber design ($\rho = 0.55, b = 2.7 \text{ um}$) for which we found the highest modal separation (to be discussed in Fig. 4.5). The latter result indicates that the proposed radially anisotropic ring-core fiber could in principle be realized using weakly birefringent metamaterials arranged along a cylindrical symmetry (Pollock et al., 2016; Pratap et al., 2018; Pratap et al., 2015).

Another interesting feature of the radially anisotropic ring-core fiber relates to a parametric space where either the TE_{01} or TM_{01} mode becomes the fundamental mode of the fiber, thus replacing the conventional HE_{11} mode in standard optical fibers. The latter feature could benefit the fiber delivery of cylindrical vector beams and their applications, including: super-resolution imaging modalities (Kozawa et al., 2018; Tian, Fu, & Gu, 2015; Zhan, 2009), laser material processing (Allegre, Perrie, Edwardson, Dearden, & Watkins, 2012; Drevinskas et al., 2016) and mode-division multiplexing (J. Liu et al., 2018; Qiao et al., 2017). The azimuthally polarized TE_{01} mode becomes the lowest-order mode within the region bordered by the white line in Fig. 4.4(a) which delineates the criterion for fundamental TE_{01} mode: $\Delta n_{eff} (TE_{01} - HE_{11}^e) \geq 0$.

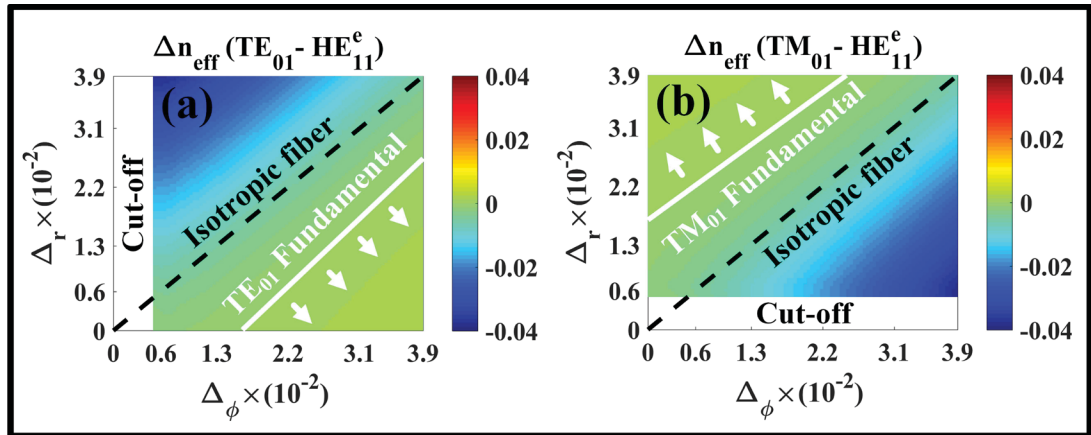


Figure 4.4. (a) Anisotropic fiber design criterion for fundamental TE_{01} and (b) TM_{01} mode

Similarly, Fig. 4.4(b) identifies the region where the radially polarized TM_{01} mode becomes fundamental ($\Delta n_{eff} (TM_{01} - HE_{11}^e) \geq 0$). We note that the ability to tune the phase-matching conditions between the generic fundamental HE_{11} mode of the fiber and the radial/azimuthal (TM_{01}/TE_{01}) modes could be exploited in optical sensing applications by means of modal interferometric measurements.

As described in Eqs. (4.1)-(4.2), the proposed fiber can be designed for the stable transmission of vortex beams formed by the combination of either hybrid HE/EH cylindrical vector modes or the radially (TM_{0m}) and azimuthally (TE_{0m}) polarized modes. In Fig. 4.5 we examine the particular case where both the CV_{11} and UV_{11} vortex modes are supported by a properly designed radially anisotropic ring-core fiber.

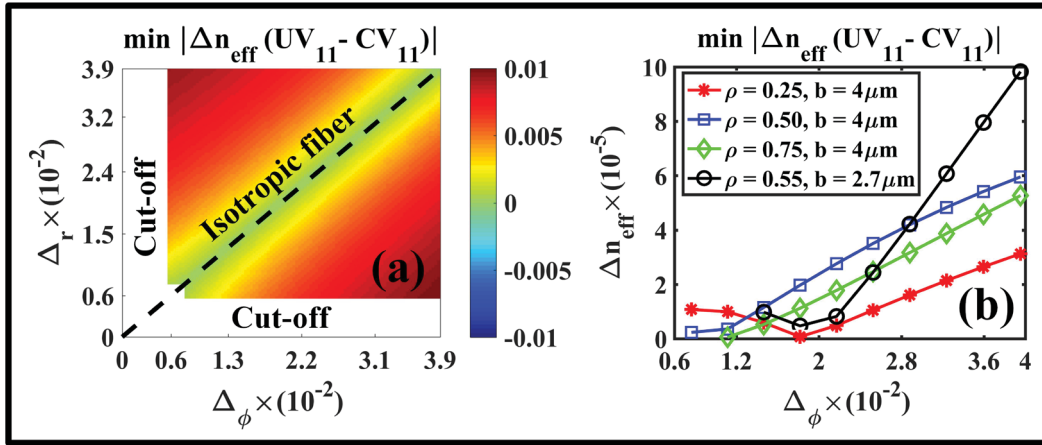


Figure 4.5. (a) Relative minimum absolute refractive index separation ($\min |\Delta n_{\text{eff}}(\text{UV}_{11} - \text{CV}_{11})|$) between CV_{11} and unstable UV_{11} beams and (b) for different anisotropic fiber designs as done in Fig. 4.3(d)

We subsequently study the guided stability of CV and UV modes in fiber, which largely depends on the intermodal separation between co-propagating mode, as low intermodal separation leads to high energy coupling between different OAM modes resulting in lower mode stability and purity. Henceforth, to study the stability of CV_{11} ($\text{HE}_{21}^e \mp i \text{HE}_{21}^o$) and UV_{11} ($\text{TM}_{01} \mp i \text{TE}_{01}$) modes in fiber, we calculated the minimum absolute refractive index separation between adjacent eigenmodes, namely, the TE_{01} and HE_{21}^e pair ($\Delta n_{\text{eff}}(\text{TE}_{01} - \text{HE}_{21}^e)$), and the TM_{01} and HE_{21}^o pair ($\Delta n_{\text{eff}}(\text{TM}_{01} - \text{HE}_{21}^o)$) in Fig. 4.5 (a). Looking at Fig. 4.5(a) one realizes that the parametric region with sufficient minimum absolute refractive index separation ($\min |\Delta n_{\text{eff}}(\text{UV}_{11} - \text{CV}_{11})| \geq 5 \times 10^{-5}$) appears in principle quite broad. Figure 4.5(b) allows to further refine this investigation by showing that the UV_{11} mode created by the superposition of TE_{01} and TM_{01} modes can reach levels of minimum intermodal separation $|\Delta n_{\text{eff}}(\text{UV}_{11} - \text{CV}_{11})| \geq 5 \times 10^{-5}$ that are close to what has been previously reported in isotropic ring-core fibers (Ma & Ramachandran, 2020). Moreover, our simulations indicate that for fiber parameters $\rho = 0.55$ and $b = 2.7 \mu\text{m}$ one can theoretically achieve large intermodal separation ($\Delta n_{\text{eff}} \sim 10^{-4}$) that is generally desirable for the long-distance and low-crosstalk fiber transmission of optical vortex modes.

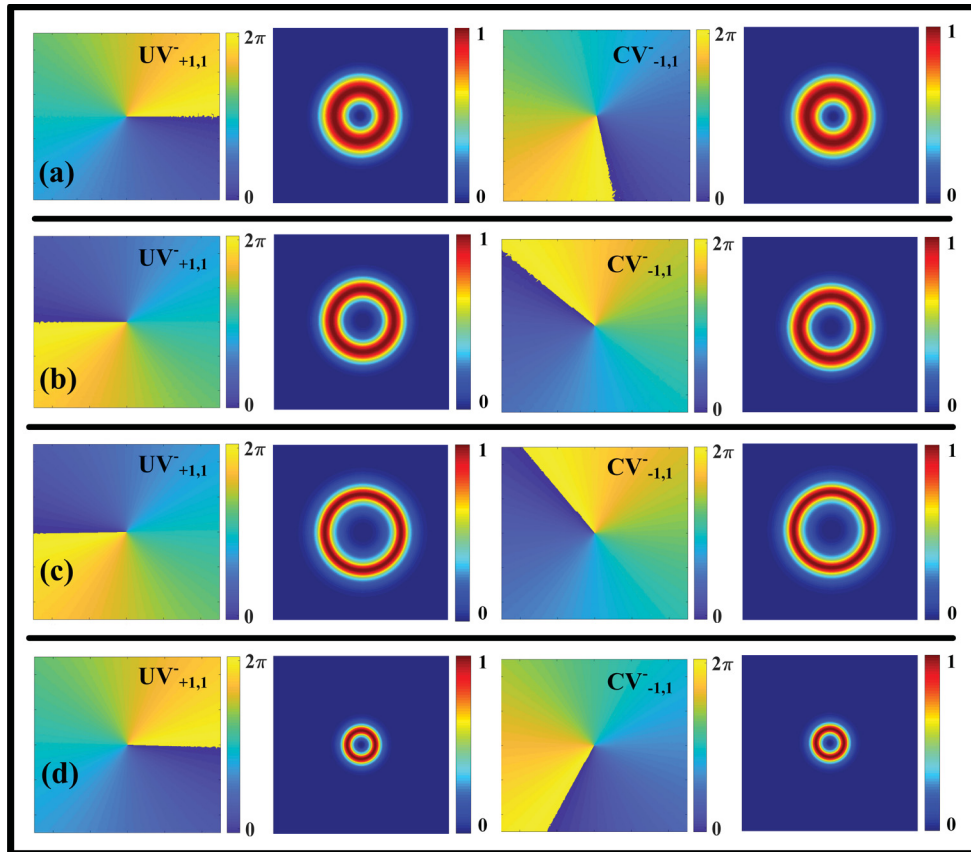


Figure 4.6. Simulated phase distribution and intensity profile of (a) $UV_{+1,1}^-$ and $CV_{-1,1}^-$ modes for $\rho = 0.25$ (b) 0.50 and (c) 0.75, while fiber core radius $b = 4$ μm and (d) for $\rho = 0.55$ and $b = 2.7$ μm

We expect the intermodal separation between adjacent eigenmodes to become even wider ($>10^{-4}$) for larger OAM charge weights ($|\ell| > 1$) as reported in similar isotropic ring-core fiber designs (Ma & Ramachandran, 2020). We further note that the previous systematic approach could be extended to find the appropriate design parameters of the radially anisotropic ring-core fiber that will support higher-order ($|\ell| \geq 2$) vortex modes enabled by both CV and UV modes.

Figure 4.6(a)-(c) presents the phase distribution and intensity profiles of OAM_{11}^\pm modes formed by the coherent superposition of hybrid HE modes ($CV_{-1,1}^- = HE_{21}^e + i HE_{21}^o$) as well as the radially and azimuthally polarized vector modes ($UV_{+1,1}^- = TE_{01} + i TM_{01}$) for fiber

parameters: $\rho=0.25, 0.50, 0.75$, $b=4$ um, $\Delta_r = 0.0360$ and $\Delta_\phi = 0.0359$. In addition, Fig. 4.6(d) plots the intensity and phase distributions for the fiber design ($\rho=0.55$, $b=2.7$ um) with which we achieved the highest intermodal separation in our simulations. One can observe in Fig. 4.6 that the calculated OAM mode purities qualitatively appear very good.

The corresponding exact OAM purities of the CV_{-11}^- and UV_{+11}^- modes were calculated and the results for the exemplar fiber design $\rho=0.25$ and $b=4$ um are shown in Fig. 4.7(a). As expected, the modal purities for the dominant topological charges ($\ell = \pm 1$) are greater than 99.9%, with minor weights distributed to neighboring charge numbers [Fig. 4.7(a)]. Mode purity was here evaluated by calculating the normalized power weight (P_ℓ) of each OAM charge number (i.e. the integer order of azimuthal harmonic) represented by ℓ , and performing the projection of the transverse electric field distribution $u(\rho, \theta)$ on the ‘‘spiral harmonics’’ $\exp(-i\ell\theta)$. The power C_ℓ carried by each ℓ -th order topological charge number was then obtained (Sharma et al., 2019b; Torner et al., 2005):

$$C_\ell = \frac{1}{2\pi} \int_0^\infty \left| \int_0^{2\pi} u(\rho, \theta) \cdot \exp(-i\ell\theta) \right|^2 \rho d\rho \quad (4.3)$$

The normalized power weight for each spiral harmonic was then determined simply:

$$P_\ell = \frac{C_\ell}{\int_{n=-\infty}^{\infty} C_\ell} \quad (4.4)$$

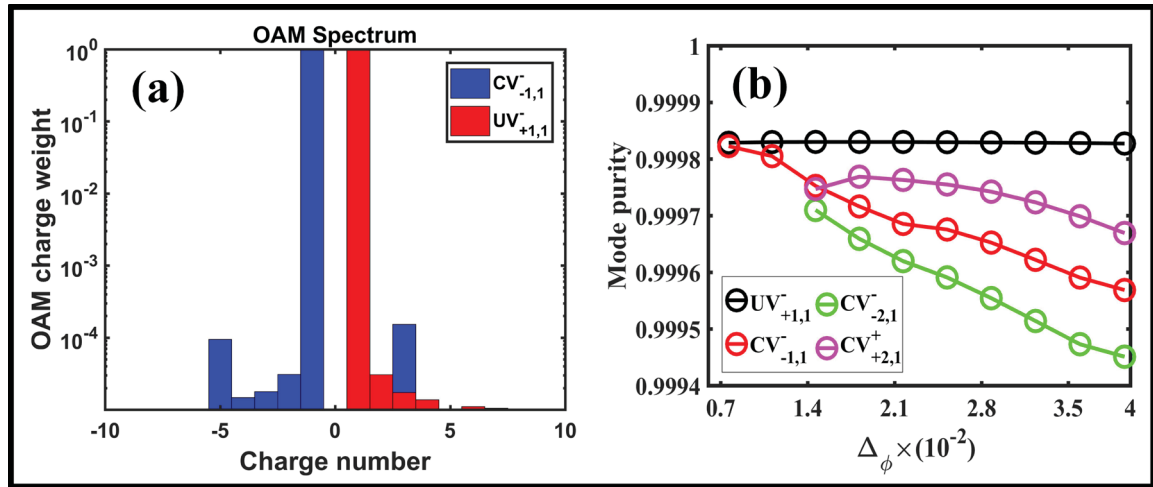


Figure 4.7. (a) OAM charge weights of generated OAM beams ($CV_{-1,1}^-$ and $UV_{+1,1}^-$) in fiber with $\rho = 0.25$, $b = 4 \text{ um}$ and $\Delta_r = 0.036$, $\Delta_\phi = 0.0359$ (for design point with highest Δ_ϕ in Fig. 4.3(d)) (b) Vortex mode purity of ($UV_{+1,1}^-$, $CV_{-1,1}^-$, $CV_{-2,1}^-$ and $CV_{+2,1}^+$) for all fiber designs (red curve in Fig. 4.3(d))

We extended the investigation of OAM mode purity in Fig. 4.7(b) to the high-order $CV_{\pm 2,1}^\pm$ modes and for the multiple fiber designs that support both stable CV and UV modes, previously identified and studied in Fig. 4.3(d) and Fig. 4.5(b). Our results [Fig. 4.7(b)] indicate that high modal purity (>99%) is similarly achieved in these other cases of interest for the radially anisotropic ring-core fiber. We nonetheless observe a very slow decline in the purities of the $CV_{-1,1}^-$, $CV_{-2,1}^-$ and $CV_{+2,1}^+$ modes with higher refractive index contrast Δ_ϕ values. In contrast, the modal purity of the $UV_{+1,1}^-$ vortex mode created by the degenerate radial and azimuthal eigenmodes remained fairly constant, irrespective of changes in the core's refractive index contrast.

4.5 Conclusion

We propose the radially anisotropic ring-core fiber as a new class of optical fiber tailored for the efficient guided transmission of vector-vortex beams. This new fiber is characterized by a core that exhibits cylindrical birefringence along the principal polar coordinates (in contrast to along the Cartesian coordinates for the usual linear birefringence). In particular, by means of theoretical analysis and FEM based numerical simulations, we elucidate the waveguiding conditions for which the fiber supports either the radially (TM_{01}) or the azimuthally (TE_{01}) polarized modes so the lowest-order fundamental mode. Also probably of higher practical interest, we show that the insertion of relatively small radial birefringence ($\Delta_r \sim 10^{-4}$) in the fiber core allows the hitherto non-degenerate TE_{0m} and TM_{0m} modes to become degenerate so as to enable the creation of stable optical vortex beams of high modal purity (>99%) through their coherent superposition. This unique feat can be achieved without affecting the remaining hybrid HE/EH modes of mixed polarization. These results are of particular relevance to OAM based mode-division multiplexing since the newly available TE/TM based vortex modes can be added on top of the commonly studied OAM channels created by the HE/EH modal basis set. The work is relevant to the areas of space-division multiplexing, transmission of structured light, fiber modelling and fabrication.

Contributions:

M.S. and B.U. contributed with the initial idea of the optical fiber design. All authors contributed to the analysis and discussion of the data and co-wrote the manuscript. All authors have read and agreed to the published version of the manuscript.

4.6 Appendix

Appendices include data for effective index values of CV_{21}^- , CV_{21}^+ modes : Fig. 4.8(a) shows the n_{eff} values of EH_{11}^e mode. Results display that the value of n_{eff} increases with increase in either Δ_r or Δ_ϕ value, and which region shows the cut-off for EH_{11}^e mode. Figure 4.8(b) indicates Δn_{eff} between EH_{11}^e and EH_{11}^o modes.

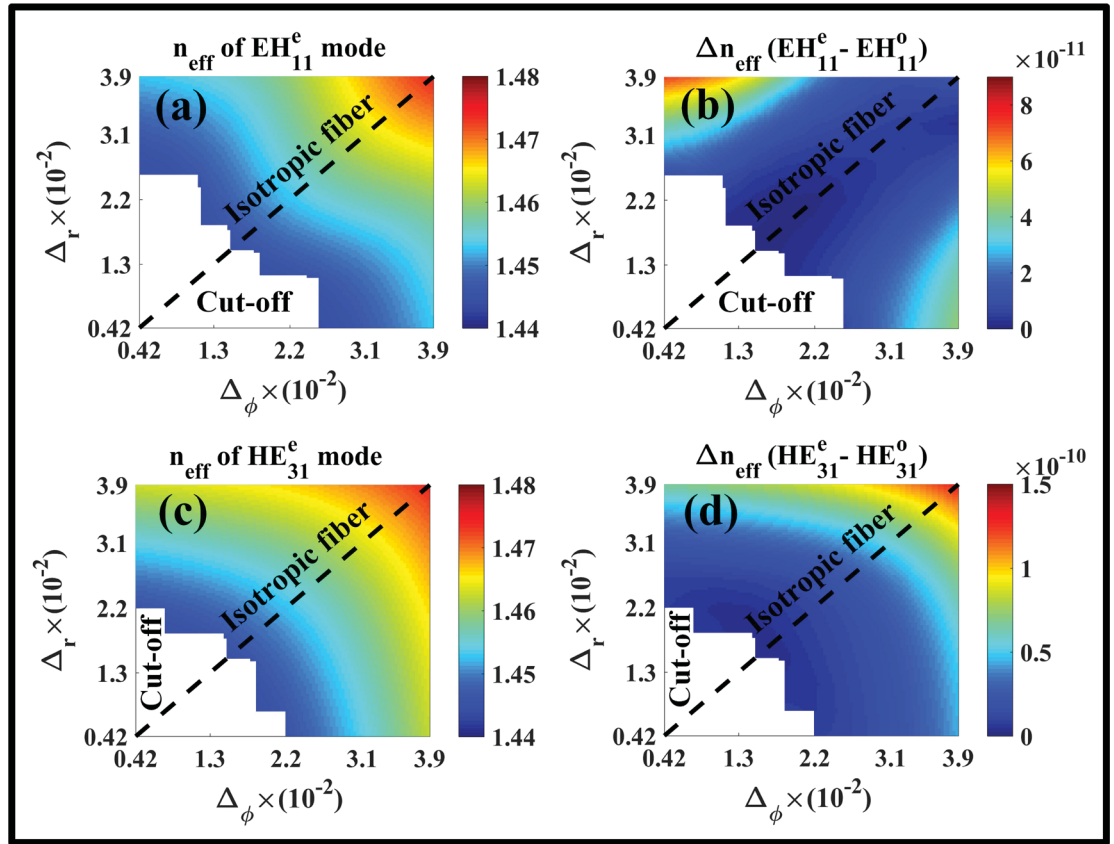


Figure 4.8. (a) Effective index (n_{eff}) of EH_{11}^e and (c) HE_{31}^e modes, while (b) effective index separation (Δn_{eff}) between EH_{11}^e and EH_{11}^o , (d) between HE_{31}^e and HE_{31}^o modes

The maximum intermodal separation $\Delta n_{eff} < 9 \times 10^{-11}$, demonstrate degeneracy for EH_{11}^e and EH_{11}^o modes irrespective of anisotropic, ideal for stability of OAM ($\ell = 2$) beam in fiber. Finally, n_{eff} values for HE_{31}^e can be found in Fig. 4.8(c) and

subsequently Δn_{eff} is shown in Fig. 4.8(d) for HE_{31}^e and HE_{31}^o modes, where $\Delta n_{eff} < 1.5 \times 10^{-10}$ for all fiber design parameters.

CONCLUSION

The OAM and CV beams of light have numerous promising applications starting from optical communication (where these beams offer tangible solutions to increases data transmission capacity) to super resolution imaging. In addition to this, supercontinuum light source of such beams could stimulate new research discoveries and applications that need require high quality and broadband source of optical vortices. Therefore, effective application of these beams requires stable and efficient guiding medium as optical fibers, which could allow linear propagation or nonlinear supercontinuum generation of these beam. Several fiber designs have been proposed in order to achieve stable transmission and supercontinuum generation of optical vortex. These fiber designs includes both step index ring fiber for stable transmission and ring photonic crystal fiber toward stable transmission and supercontinuum generation. Although ideal fiber design toward stable supercontinuum generation of optical vortex, with high mode purity still a landmark to attain. To fill this void, this thesis reports novel fiber design candidates that enable stable transmission of these vortex modes and intended toward there supercontinuum generation, ultimate object of this work.

To start with, we have investigated fiber design and simulation based on hexagonal-lattice structure of air holes named as annular core photonic crystal fiber (AC-PCF), that enables stable broadband transmission and supercontinuum generation of optical vortices. A finite element method-based simulation was performed to attain novel waveguiding regime in AC-PCF, where fiber strictly support first order radial mode irrespective of operational wavelength and is supported by theoretical mathematical investigation. This guiding regime is named as endlessly mono-radial guiding, occurs for fiber design condition $d/\Lambda < 0.35$. It is followed by fiber design parameter engineering to achieve desired optical properties as: flat lower chromatic dispersion, higher or lower nonlinearities, based on application either linear optical communication or nonlinear supercontinuum generation of single ring intensity optical vortices. Finally, a numerical study is performed by solving generalized nonlinear

Schrödinger equation toward stable supercontinuum generation of optical vortices in ACPCF. Unique characteristics of proposed fiber design thus make it suitable guiding medium to explore mono-annular beams (OAM and CV beams), linear or nonlinear broadband regime. Both theoretical and numerical simulation results presented in this work could enhance understanding of future researcher in further exploring similar fiber design candidates for optical vortices.

In second stage, the endlessly mono-radial AC-PCF was fabricated and we experimentally demonstrated stable propagation of mono-radial singular beam, both OAM and CV beams. The scanning electron microscope (SEM) image of fabricated AC-PCF has an average air hole diameter ($d = 0.48 \mu\text{m}$) and periodic air spacing of $\Lambda = 1.4 \mu\text{m}$, thus satisfying condition for endlessly mono-radial guiding ($d/\Lambda < 0.35$). Further, attenuation losses for fundamental mode propagation in were measured and found to be around 0.5 dB/m inside in 800 - 845 nm wavelength range. Finally, singular beams (OAM and CVBs) were created in free space using well known S-waveplate and then launched in AC-PCF. The experimental results demonstrated that singular beams maintain good mode purity for large wavelength range of investigation. The experimental characterization results demonstrate that such fiber design could become a significant step towards the stable and broadband transmission of OAM and CV beams in result could be leads to applications in high-speed communication, sensing employing structured light and many more.

Obviously, there is no perfect fiber design suitable for achieving stability and higher mode purity of optical vortex. There is always a tradeoff between number of mono-radial modes fiber support, their mode stability and purity. In Particular, fiber designs that enforce endlessly mono-radial guiding, air holes to pitch ratio (d/Λ) need to be < 0.35 , which in result effect confinement loss (as evident from cutback loss data 0.5 dB/m for 800 - 845 nm wavelength range in fabricated AC-PCF) of guiding modes. These confinement losses could be minimized by designing fiber with large air hole pitch (Λ), in other words increasing fiber core size. However, complete photonic crystal fiber structure including cladding need to be

less than $125\ \mu\text{m}$ as this is standard for fiber optic communication systems. Moreover, increasing fiber size increases mode field diameter, hence reduces nonlinear coefficient (ideal for linear application but not so good in supercontinuum generation of mon-radial modes) further it effects fiber dispersion which need to be optimized. In addition to this, large core size could increase birefringence (evident in simulations performed) in fiber, thus effecting stability of optical vortex, especially of polarization vortices. Hence, fiber design suitable for telecom application that demonstrate low overall losses remains to be explored, which desires future research in order to understand the relation of air hole pitch size against fiber losses and birefringence.

In addition, fiber characterization experiment in this work is limited to the calculation of attenuation loss and measuring optical vortex mode stability after travelling through fiber. There are several other linear (polarization mode dispersion, chromatic dispersion, bending loss and signal to noise ratio) and nonlinear (stimulated Brillouin and Raman scattering) fiber characterizations that could be performed to better understand higher mode guidance in AC-PCF. Likewise, the vortex mode stability and purity calculations are limited to topological charge ($l = 1$) as available S-plate could generate vortex beams of first order. The excitation and transmission of higher topologically charged beams in the AC-PCF is something to perform in a future work.

Finally, we propose a new class of optical fiber known as radially anisotropic ring core fiber for efficient co-propagation of vector-vortex beams formed by superposition of either degenerate radially (TM_{0m}) and azimuthally (TE_{0m}) polarized vector modes (a feat not achievable is standard ring fiber), or hybrid (HE / EH) modes. The proposed new fiber is characterized by its core that displays cylindrical birefringence along principle polar coordinates. The FEM based numerical simulation results interpret the waveguiding conditions where either the radially (TM_{01}) or the azimuthally (TE_{01}) polarized modes become the fundamental mode instead of the usual linearly polarized HE_{11} mode. The numerical simulation also shows that adding small radial birefringence ($\sim 10^{-4}$) in ring core

of fiber could allow usually non-degenerate TE_{0m} and TM_{0m} modes (in conventional circular ring fiber) to become degenerate, thus make possible to create stable optical vortex (with high theoretical modal purity ($>99\%$)) by superposition of TE_{0m} and TM_{0m} modes. Further, this radial birefringence does not affect the degeneracy of hybrid HE/EH modes. These findings are of particular significance in mode-division multiplexing since newly created TE/TM based OAM mode could be added to already available OAM channels (by HE/EH hybrid modes).

The results presented in chapter 4 towards design of radially anisotropic ring core fiber are of high significance in order to realize co-propagation of all kinds of degenerated vortex mode. However, this work is limited to FEM based numerical simulation and therefore a fully developed theoretical or mathematical model to better understand effect of anisotropy on different vector modes of fiber, in particular hybrid modes like: HE/EH modes will immensely benefit future research community. Finally, this work proposes numerical optimization of radially anisotropic ring core fiber and basically propose idea of new fiber type that could be realized using metamaterial, however for now we are unable to predict experimental realization towards fabrication of this fiber types. Hence, research for experimental fabrication of such fiber type would give new dimension to possibly future optical communication.

At the end, there are many questions remains open in this thesis, which is not unanticipated, as we explored only several facets of very vast topic. We conclude by discussing some open topics in following section that could be explored in future.

STATEMENT OF ORIGINAL CONTRIBUTION & FUTURE RECOMMENDATIONS

Statement of original contribution

The original contributions to the research described in this thesis are summarized below:

1. Theoretical design and optimization of a novel annular core photonic crystal fiber is presented for the first time, which exhibit broadband transmission of endlessly mono-radial OAM and CVBs.
2. A theoretical case study is reported regarding application of AC-PCF in supercontinuum generation of vortex beams.
3. Fabricated AC-PCF has been experimentally characterized for transmission of these doughnut shaped optical vortices, which shows higher mode purity and stability.
4. Radially anisotropic ring-core optical fiber has been demonstrated for novel light guiding properties i.e, towards vector-vortex mode transmission using the full modal space of fiber.

Recommendations for future work

Structured light (i.e. optical vortices) has several unique emerging application and consequently fiber design for stable transmission of optical vortices remains rich in photonic research. Here we proposed some suggestions for further improvement on fiber designs reported in this thesis followed by their possible application so as to extend the research covered in this thesis:

AC-PCF fiber design and characterization for other applications

The endlessly mono-radial AC-PCF fiber was initially designed specifically for supercontinuum generation of optical vortices, where design parameters are optimized

recognizing target center wavelength near 835 nm. Henceforth, further design optimizations are required on this AC-PCF (while keeping $d/\Lambda = 0.35$) to achieve better characterization and deeper knowledge in application related to optical communication and fiber based optical sensing (using optical vortices). Besides this, the average optical losses reported are of around 0.5 dB/m for AC-PCF in the wavelength range from 800 to 845 nm, which require further improvement for feasibility in application related to communication. In addition to this, several other fiber characterizations need to be performed i.e: refractive index measurement, polarization mode dispersion, chromatic dispersion, bending loss and signal to noise ratio (linear) and supercontinuum generation, stimulated Brillouin and Raman scattering (nonlinear). Likewise, excitation and transmission of higher topologically charged beams to calculate the vortex mode stability and purity can be performed to realized mode division multiplexing. Finally, it is required to experimentally transmit several mono-radial vortex modes and study the effect of crosstalk between each mode in order to realize multiple optical communication channel. This study will allow to maintain better stability and higher mode purity of each vortex mode in fiber. Other than this, significant efforts are required toward designing multiplexer and demultiplexer both for free-space optics and integrated photonic and studying performance of optical vortex-based communication systems. Finally an experimental comparison study between ring core fibers and annular core photonic crystal fiber design (similar to chapter 3 experimental work) would allow a better evaluation of potential possible application of AC-PCF.

Application of AC-PCF in sensing based on optical vortices.

Fiber – based optical sensors have evolved as effective sensing techniques as these sensors are extremely compact, precise, and cost effective. Photonic crystal fibers owing to microstructure array of air holes can become significant for continuous monitoring of chemical samples as: blood glucose, food samples and bio fluids, which are used in biomedical and chemical industry. Such specialty fibers have several tunable parameters such as: air hole diameter, pitch, and number of concentric air holes rings, thus demonstrate

advantage over conventional all-solid fibers in realizing higher sensitivity. Moreover, air hole in PCF provides micro – fluidic channels in realizing ultra-small volume of specimen or sample additionally the fact that these micro channels are closer to the fiber core, allows better interaction of the analytes with core modes of optical fiber. Therefore, this technique could allow one to study interaction of analytes with guided optical vortex beams in AC-PCF and has potential for development of a novel fiber-optics sensors.

Developing theoretical model and studying possible fabrication techniques of radially anisotropic ring-core fiber

The chapter 4 in this thesis, reports finite element method based theoretical study on optimization of radially anisotropic ring-core optical fiber, which could be ideal candidates for co-propagation of IV and CV modes. Current research is limited to theoretical simulation where optimized fiber candidates are proposed. Therefore, in order to understand the exact phenomenon of radial anisotropy on different fiber modes (especially hybrid modes like: HE/EH modes), future need is to develop a mathematical model based on Helmholtz equation. In addition, an extensive feasible study is required for experimental fabrication of radially anisotropic fiber using metamaterial-based technique. It could have promising application in areas of space-division multiplexing and optical communication. In parallel to this, researcher also required to explore different other possible techniques for the fabrication of such radial anisotropic optical fibers.

ANNEXE I

PRINCIPLES OF THE FINITE-ELEMENT METHOD

All fibers design (annular core photonic crystal fiber and radially anisotropic ring core fiber) proposed in this thesis are analysis using Finite element method implemented using commercially available COMSOL Multiphysics software (that allows application of FEM method in numerous engineering problems as: structural mechanics, fluid dynamics and electromagnetic). The software has several physics modules with could be integrated together for multiphase problem if needed. It is integrated with computer-aided design (CAD) for designing structures (however with limited flexibility for design change). Other than this, the software allows Matlab scripting interface therefore one can easily perform design parameter changes, meshing optimization and variation in physical and boundary parameters.

Optical waveguides guided modes are governed by time-independant Helmholtz equation and written in terms of E electric field component:

$$(\nabla^2 + k_0^2 n^2)E = 0 \quad (\text{A I-1})$$

where time dependance was assumed $e^{-i\omega t}$ and k_0 is wavevector.

The FEM method divided domains into subdomains or finite size elements called the process of discretization. This discretization can be achieved by employing regular or irregular triangles in case of two-dimensional problem and tetrahedron for three-dimensional problems. Then the interpolation function of second or higher order polynomial is defined locally for all subdomains to approximate the unknown field inside subdomains. This order of polynomial depends on desired accuracy of solution and size of subdomain. Higher order shape function is advised in case of complex problem as: for waveguide regions with rapidly varying field amplitude. Further, smaller size of shape function reduces the numerical error

in simulation, although increases degree of freedoms to solve for and in results requires higher computer memory. Therefore, one need to perform convergence analysis before when performing finite-element calculations such that solution converges asymptotically towards given values (already known analytical values). Implementation of FEM using COMSOL Multiphysics starts with defining geometry, where transverse structure of fiber is defined. Working with Matlab scripting interface allows to change fiber parameters or perform parameter sweep for air hole pitch and diameter. Further, material's physical properties need to be set appropriately for each subdomain in geometry as: the air hole domain is defined air properties (refractive index of air) and other domains are defined with pure silica fiber wavelength dependence refractive index equation. The outer layer of fiber geometry is defined by Perfect Match Layers (PMLs) condition is defined, which act as absorbing boundary to introduce no back reflection from incidence electromagnetic radiation. This allows to truncate the domain of interest for simulation and it mimics the infinite structure with finite domain (Wu, Kingsland, Lee, & Lee, 1997). The material defined for PML domain is always similar to its connecting domain (hence pure silica in this case). This is followed by setting physics and all types of boundary conditions including PML condition. Domain discretization is done using meshing, where mesh size can determine the accuracy of solution and time required. One example of meshing is showing in Fig-A I-1 (a) to (c) with different zoom ratio, regenerated in COMSOL. As in figure, courser mesh is drawn for region of less interest while, very fine mesh is required for fiber core region where highest field intensity is found as in Fig-A I-1(d). Other less prominent regions require a smaller number of elements thus reduce simulation time. The recent version of COMSOL provide flexibility to define a mesh control domain or boundary specifically for meshing, which add in mesh optimization.

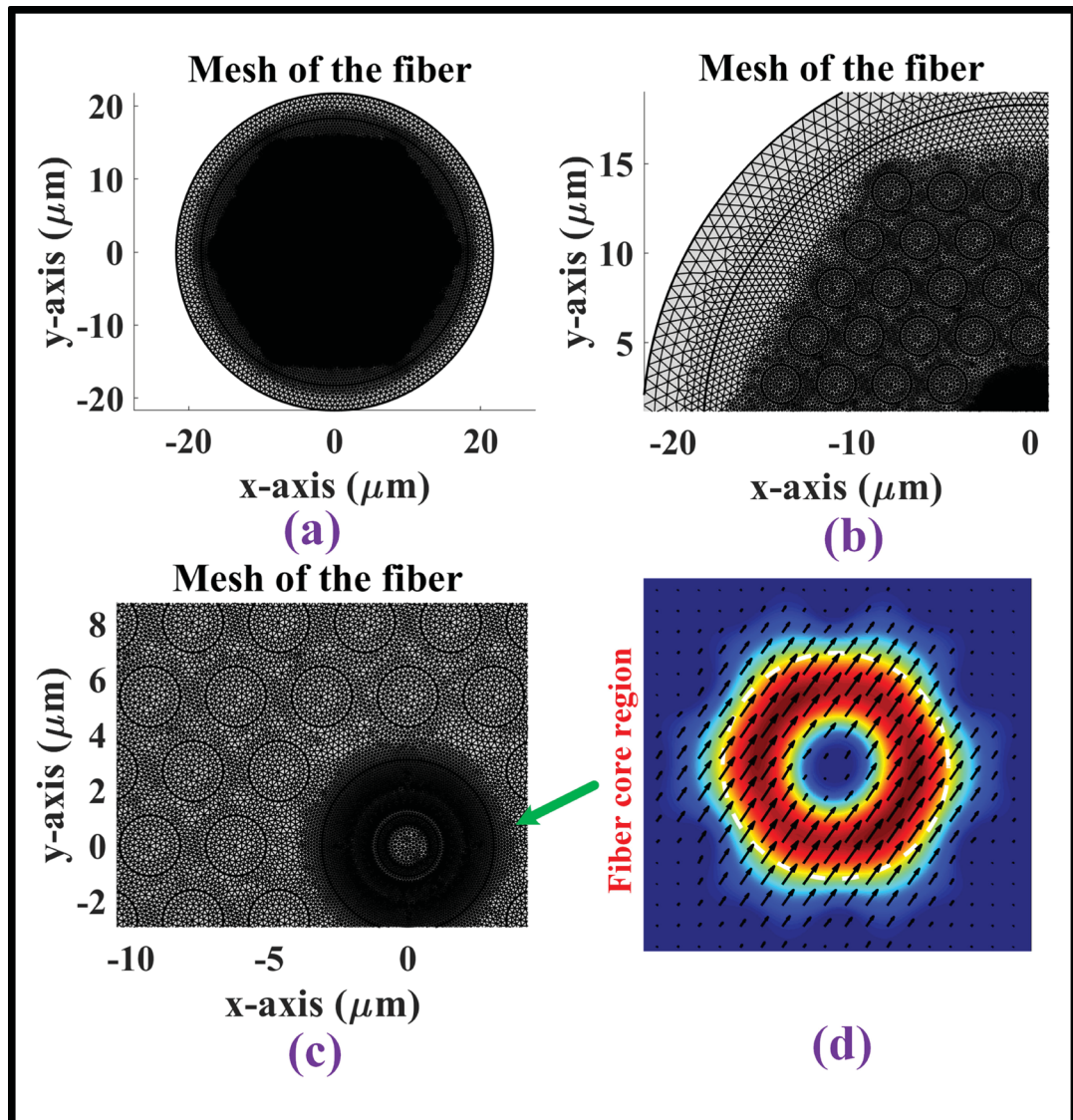


Figure-A I-1 Example of an FEM simulation the generated mesh by COMSOL at different zoom scales, farthest (a) to closest (c) and (d) simulated mode field of HE_{11} guided in core for modelling annular core photonic crystal fiber

ANNEXE II

BEAM SIZE MEASUREMENT (KNIFE – EDGE METHOD)

To estimate the coupling efficiency (justification of launching efficiency in section 3.4, the vector-vortex beams as 44%), OAM beam size (at focus of microscope objective) is measured using knife-edge technique (well known for beam size measurement of Gaussian beam) (Siegman et al., 1991). Figure-A II-1 (a) shows the schematic image of experimental setup used for beam size measurement, here OAM (doughnut shape) beam coming from S-Plate is focused using microscope objective 1, which is a 20x and 0.4 NA microscope objective.

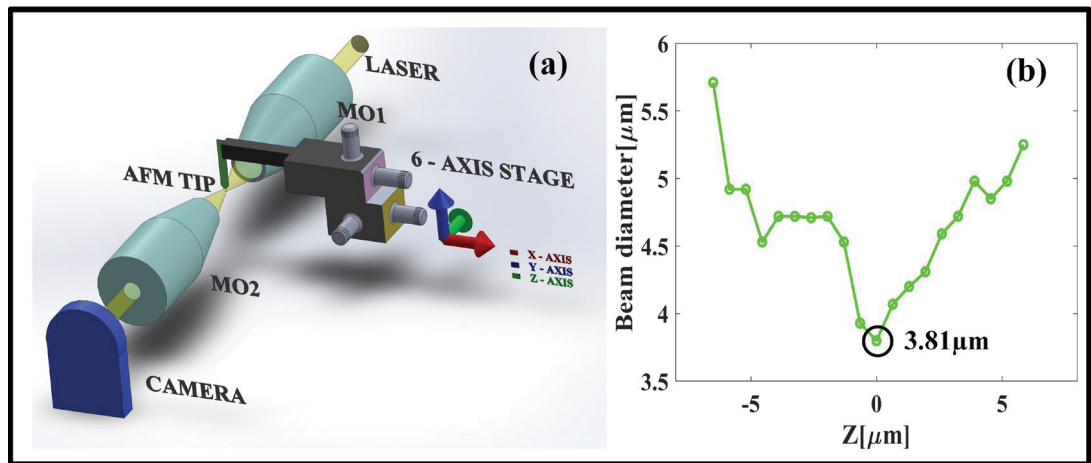


Figure-A II-1 (a) Experimental setup of knife edge method for beam (OAM) size measurement (b) Variation of OAM beam size along Z (Focus) -axis

This is followed by another 20x microscope objective used for collimation of OAM beam and is imaged via CCD camera. A sharp AFM tip (fabricated in lab) is used for straight knife-edge cutting into a doughnut shaped OAM beam in step of 0.65 micrometer (minimum resolution can be achieved manually using 6 - axis stage) along transverse direction and corresponding intensity profile of beam is imaged (recorded) along with the power. Initially when the beam is not covered by AFM tip, the measured power remains to maximum value, while the power decreases as beam is gradually covered by tip and attained minimum in fully

covered state. Hence, the power is measured as a function of propagation along transverse direction. The obtained data is polynomial fitted and further the numerical differentiations of fitted data give approximate the beam shape or size to measured. In fig-A II-1(a) the direction of beam cutting is along x axis (transverse), while Z axis demonstrate the direction of beam propagation or focus axis of MO. The beam size measurement process discussed above is followed along focus axis (z axis) with 1.3 micrometer step size to first reaches close to focus (within 0.65 micrometer region). Figure 6 (b) shows the plot of beam size obtained along focus axis, where $z = 0$ is the focus point found. The beam size along z axis clearly show that, minimum beam size measure at focus is 3.8 micrometer (at focus beam size is obtained with optimum manually achievable step size of 0.65 mm) and this value increases as we move away from focus axis.

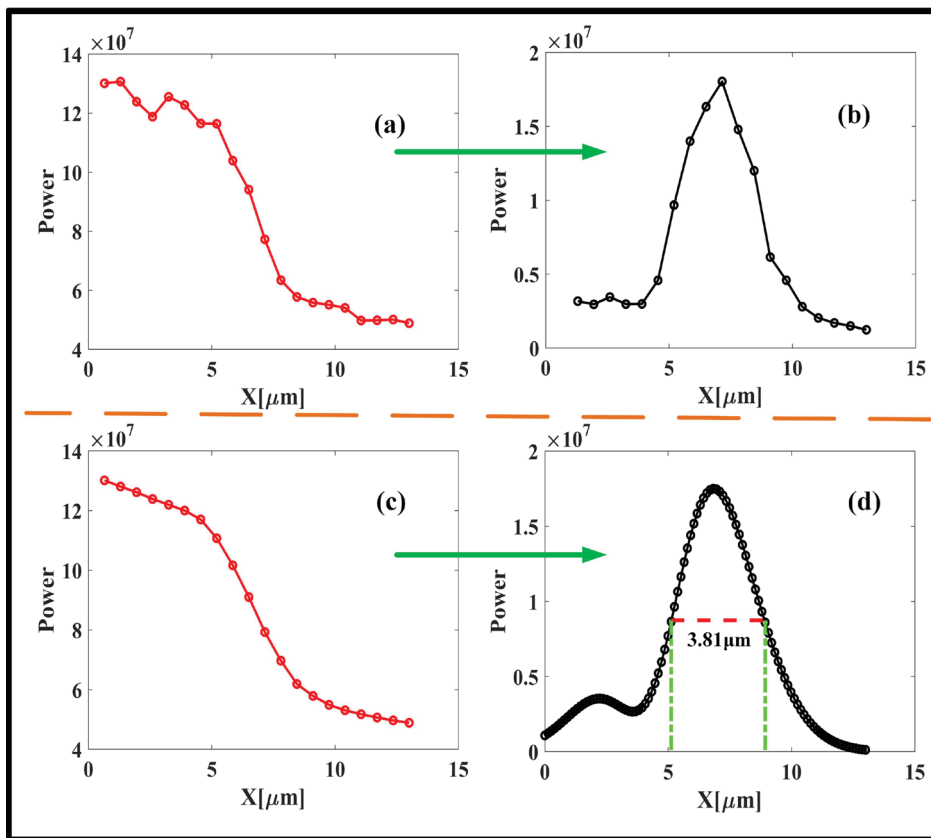


Figure-A II-2 (a) Experimental data of power obtained during knife-edge measurement for beam (OAM) size (b) numerical differentiation (data) of the power measured by the knife-

edge method (c) Polynomial fitting of power measured (d) numerical differentiation of the fitted power

Figure-A II-2 shows the experimental data obtained (using knife-edge method) for beam size of OAM beam at focus ($Z = 0$) of microscope objective. Fig-A II-2(a) show the plot of measured power as a function of AFM tip location, while Fig-A II-2(b) shows the actual beam size estimated by numerical differentiation of power data. In addition to this, the polynomial fitting of actual data is done as in Fig-A II-2(c), which after numerical differentiation gives the beam size shown in Fig-A II-2(d).

LIST OF PUBLICATIONS

Journals:

- Sharma, M., Pradhan, P., & Ung, B. (2019). Endlessly mono-radial annular core photonic crystal fiber for the broadband transmission and supercontinuum generation of vortex beams. *Scientific reports*, 9(1), 1-12
- Sharma, M., Amirkhan, F., Mishra, S. K., Sengupta, D., Messaddeq, Y., Blanchard, F., & Ung, B. (2020). Transmission of Orbital Angular Momentum and Cylindrical Vector Beams in a Large-Bandwidth Annular Core Photonic Crystal Fiber. *Fibers*, 8(4), 22.
- Sharma, M., Vigneswaran, D., LaRoche S., Rusch, L. A., & Ung, B. (2021). Radially anisotropic ring-core optical fiber: towards vector-vortex guided transmission using the full modal space. *OSA Continuum* 4.4 (2021): 1282-1292..
- Pradhan, P., Sharma, M., & Ung, B. (2018). Generation of perfect cylindrical vector beams with complete control over the ring width and ring diameter. *IEEE Photonics Journal*, 10(1), 1-10.

Conferences:

- Sharma, M., & Ung, B. (2018). Design and fabrication of novel photonic crystal fiber for supercontinuum generation of OAM beam. Photonic North 2018.
- Sharma, Manish, Mishra, S. K., & Ung, B. (2019, September). Ultra-sensitive and large dynamic range refractive index sensor utilizing annular core photonic crystal fiber. In *Photonic Fiber and Crystal Devices: Advances in Materials and Innovations in Device Applications XIII* (Vol. 11123, p. 1112305). International Society for Optics and Photonics.
- Mishra, S. K., Sharma, Manish, & Ung, B. (2019, September). OAM beam propagation in hollow core capillary fiber for the study of chiral light matter interactions. In *Optical Trapping and Optical Micromanipulation XVI* (Vol. 11083, p. 1108330). International Society for Optics and Photonics.
- Azad, Saeed, Satyendra Kumar Mishra, Manish Sharma, Ricardo Izquierdo, and Bora Ung. "Low magnetic field detection via nanometre scale air-holes photonic crystal fiber filled with magnetic fluid." In 2019 IEEE SENSORS, pp. 1-4. IEEE, 2019.

Sharma, Manish, Fatemeh Amirkhan, Satyendra K. Mishra, Dipankar Sengupta, Younès Messaddeq, François Blanchard, and Bora Ung. "Annular core photonic crystal fiber for propagation of optical vortices." In 2020 Conference on Lasers and Electro-Optics (CLEO), pp. 1-2. IEEE, 2020.

Sharma, Manish, Fatemeh Amirkhan, Satyendra K. Mishra, Dipankar Sengupta, Younès Messaddeq, François Blanchard, and Bora Ung. "Annular core photonic crystal fiber for transmission of endlessly mono-radial vortex beams." In Specialty Optical Fibers, pp. SoM3H-7. Optical Society of America, 2020.

BIBLIOGRAPHIE

- Afshar, S., & Monro, T. M. (2009). A full vectorial model for pulse propagation in emerging waveguides with subwavelength structures part I: Kerr nonlinearity. *Optics express*, 17(4), 2298-2318.
- Agrawal, G. P. (2000). Nonlinear fiber optics. Dans *Nonlinear Science at the Dawn of the 21st Century* (pp. 195-211). Springer.
- Alexeyev, A., Fadeyeva, T., Volyar, A., & Soskin, M. (1998). Optical vortices and the flow of their angular momentum in a multimode fiber. *Semiconductor Physics Quantum Electronics & Optoelectronics*.
- Allegre, O., Perrie, W., Edwardson, S., Dearden, G., & Watkins, K. (2012). Laser microprocessing of steel with radially and azimuthally polarized femtosecond vortex pulses. *Journal of Optics*, 14(8), 085601.
- Allen, L., Beijersbergen, M. W., Spreeuw, R., & Woerdman, J. (1992). Orbital angular momentum of light and the transformation of Laguerre-Gaussian laser modes. *Physical Review A*, 45(11), 8185.
- Andersen, M., Ryu, C., Cladé, P., Natarajan, V., Vaziri, A., Helmerson, K., & Phillips, W. D. (2006). Quantized rotation of atoms from photons with orbital angular momentum. *Physical review letters*, 97(17), 170406.
- Birks, T. A., Knight, J. C., & Russell, P. S. J. (1997). Endlessly single-mode photonic crystal fiber. *Optics letters*, 22(13), 961-963.
- Bisson, J.-F., Li, J., Ueda, K., & Senatsky, Y. (2006). Radially polarized ring and arc beams of a neodymium laser with an intra-cavity axicon. *Optics express*, 14(8), 3304-3311.
- Black, R., Veilleux, C., Bures, J., & Lapierre, J. (1985). Radially anisotropic lightguide mode selector. *Electronics Letters*, 21(21), 987-989.
- Blow, K. J., & Wood, D. (1989). Theoretical description of transient stimulated Raman scattering in optical fibers. *IEEE Journal of Quantum Electronics*, 25(12), 2665-2673.
- Bovino, F. A., Braccini, M., Bertolotti, M., & Sibilìa, C. (2011). Management of the orbital angular momentum of vortex beams in a quadratic nonlinear interaction. *Optics communications*, 284(10-11), 2587-2593.

- Bozinovic, N., Kristensen, P., & Ramachandran, S. (2011). Long-range fiber-transmission of photons with orbital angular momentum. Dans *CLEO: Science and Innovations* (pp. CTuB1). Optical Society of America.
- Bozinovic, N., Ramachandran, S., Brodsky, M., & Kristensen, P. (2011). Record-length transmission of photons entangled in orbital angular momentum (OAM). Dans *Frontiers in Optics* (pp. PDPB1). Optical Society of America.
- Brulot, W., Vanbel, M. K., Swusten, T., & Verbiest, T. (2016). Resolving enantiomers using the optical angular momentum of twisted light. *Science advances*, 2(3), e1501349.
- Brunet, C., & Rusch, L. A. (2017). Optical fibers for the transmission of orbital angular momentum modes. *Optical Fiber Technology*, 35, 2-7.
- Brunet, C., Ung, B., Bélanger, P.-A., Messaddeq, Y., LaRochelle, S., & Rusch, L. A. (2014). Vector mode analysis of ring-core fibers: Design tools for spatial division multiplexing. *Journal of lightwave technology*, 32(23), 4046-4057.
- Brunet, C., Ung, B., Wang, L., Messaddeq, Y., LaRochelle, S., & Rusch, L. A. (2015). Design of a family of ring-core fibers for OAM transmission studies. *Optics Express*, 23(8), 10553-10563. doi: 10.1364/OE.23.010553.
Repéré à <http://www.opticsexpress.org/abstract.cfm?URI=oe-23-8-10553>
- Brunet, C., Vaity, P., Messaddeq, Y., LaRochelle, S., & Rusch, L. A. (2014). Design, fabrication and validation of an OAM fiber supporting 36 states. *Optics express*, 22(21), 26117-26127.
- Cameron, R. P., Götte, J. B., Barnett, S. M., & Yao, A. M. (2017). Chirality and the angular momentum of light. *Philosophical Transactions of the Royal Society A: Mathematical, Physical and Engineering Sciences*, 375(2087), 20150433.
- Chen, M., Mazilu, M., Arita, Y., Wright, E. M., & Dholakia, K. (2013). Dynamics of microparticles trapped in a perfect vortex beam. *Optics letters*, 38(22), 4919-4922.
- Chen, R., Agarwal, K., Sheppard, C. J., & Chen, X. (2013). Imaging using cylindrical vector beams in a high-numerical-aperture microscopy system. *Optics letters*, 38(16), 3111-3114.
- Chen, S. H., & Chen, T. J. (1994). Observation of mode selection in a radially anisotropic cylindrical waveguide with liquid-crystal cladding. *Applied Physics Letters*, 64(15), 1893-1895.

- Chen, T.-J., & Chen, S.-H. (1995). Propagation of lower-order modes in a radially anisotropic cylindrical waveguide with liquid crystal cladding. *Journal of lightwave technology*, 13(8), 1698-1705.
- Chen, Y. (1991). Anisotropic ring fibers with cylindrical polar principal axes. *Optics letters*, 16(12), 904-906.
- Corsi, A., Chang, J. H., Wang, R., Wang, L., Rusch, L. A., & LaRochelle, S. (2020). Highly elliptical core fiber with stress-induced birefringence for mode multiplexing. *Optics letters*, 45(10), 2822-2825.
- Dashti, P. Z., Alhassen, F., & Lee, H. P. (2006). Observation of orbital angular momentum transfer between acoustic and optical vortices in optical fiber. *Physical review letters*, 96(4), 043604.
- Deiterding, R., Glowinski, R., Oliver, H., & Poole, S. (2013). A reliable split-step Fourier method for the propagation equation of ultra-fast pulses in single-mode optical fibers. *Journal of lightwave technology*, 31(12), 2008-2017.
- Drevinskas, R., Zhang, J., Beresna, M., Gecevičius, M., Kazanskii, A. G., Svirko, Y. P., & Kazansky, P. G. (2016). Laser material processing with tightly focused cylindrical vector beams. *Applied Physics Letters*, 108(22), 221107.
- Dudley, J. M., Genty, G., & Coen, S. (2006). Supercontinuum generation in photonic crystal fiber. *Reviews of modern physics*, 78(4), 1135.
- Dudley, J. M., & Taylor, J. R. (2010). *Supercontinuum generation in optical fibers*. Cambridge University Press.
- Duocastella, M., & Arnold, C. B. (2012). Bessel and annular beams for materials processing. *Laser & Photonics Reviews*, 6(5), 607-621.
- Ertman, S., Rutkowska, K., & Woliński, T. R. (2018). Recent progress in liquid-crystal optical fibers and their applications in photonics. *Journal of lightwave technology*, 37(11), 2516-2526.
- Essiambre, R.-J., & Tkach, R. W. (2012). Capacity trends and limits of optical communication networks. *Proceedings of the IEEE*, 100(5), 1035-1055.
- Forbes, K. A., & Andrews, D. L. (2018). Optical orbital angular momentum: twisted light and chirality. *Optics letters*, 43(3), 435-438.

- Gecevičius, M., Drevinskas, R., Beresna, M., & Kazansky, P. G. (2014). Single beam optical vortex tweezers with tunable orbital angular momentum. *Applied Physics Letters*, *104*(23), 231110.
- Gecevicius, M., Ivanov, M., Beresna, M., Matijosius, A., Tamuliene, V., Gertus, T., . . . Smilgevicius, V. (2018). Toward the generation of broadband optical vortices: extending the spectral range of a q-plate by polarization-selective filtering. *JOSA B*, *35*(1), 190-196.
- Gibson, G., Courtial, J., Padgett, M. J., Vasnetsov, M., Pas'ko, V., Barnett, S. M., & Franke-Arnold, S. (2004). Free-space information transfer using light beams carrying orbital angular momentum. *Optics express*, *12*(22), 5448-5456.
- Golowich, S. E., Kristensen, P., Bozinovic, N., Gregg, P., & Ramachandran, S. (2012). Fibers supporting orbital angular momentum states for information capacity scaling. Dans *Frontiers in Optics* (pp. FW2D. 2). Optical Society of America.
- Gregg, P., Kristensen, P., Golowich, S., Olsen, J., Steinvurzel, P., & Ramachandran, S. (2013). Stable transmission of 12 OAM states in air-core fiber. Dans *CLEO: 2013* (pp. 1-2). IEEE.
- Gregg, P., Kristensen, P., & Ramachandran, S. (2015). Conservation of orbital angular momentum in air-core optical fibers. *Optica*, *2*(3), 267-270.
- Grosjean, T., Courjon, D., & Spajer, M. (2002). An all-fiber device for generating radially and other polarized light beams. *Optics Communications*, *203*(1-2), 1-5.
- Hamazaki, J., Morita, R., Chujo, K., Kobayashi, Y., Tanda, S., & Omatsu, T. (2010). Optical-vortex laser ablation. *Optics express*, *18*(3), 2144-2151.
- Hansinger, P., Maleshkov, G., Garanovich, I., Skryabin, D., Neshev, D., Dreischuh, A., & Paulus, G. (2016). White light generated by femtosecond optical vortex beams. *JOSA B*, *33*(4), 681-690.
- Hu, Z.-A., Huang, Y.-Q., Luo, A.-P., Cui, H., Luo, Z.-C., & Xu, W.-C. (2016). Photonic crystal fiber for supporting 26 orbital angular momentum modes. *Optics express*, *24*(15), 17285-17291.
- Hwang, I. K., Yun, S. H., & Kim, B. Y. (1999). Long-period fiber gratings based on periodic microbends. *Optics letters*, *24*(18), 1263-1265.

- Ishio, H., Minowa, J., & Nosu, K. (1984). Review and status of wavelength-division-multiplexing technology and its application. *Journal of lightwave technology*, 2(4), 448-463.
- Kabir, M. A., Hassan, M. M., Hossain, M. N., Paul, B. K., & Ahmed, K. (2020). Design and performance evaluation of photonic crystal fibers of supporting orbital angular momentum states in optical transmission. *Optics Communications*, 125731.
- Karimi, E., Schulz, S. A., De Leon, I., Qassim, H., Upham, J., & Boyd, R. W. (2014). Generating optical orbital angular momentum at visible wavelengths using a plasmonic metasurface. *Light: Science & Applications*, 3(5), e167-e167.
- Kozawa, Y., Matsunaga, D., & Sato, S. (2018). Superresolution imaging via superoscillation focusing of a radially polarized beam. *Optica*, 5(2), 86-92.
- Kozawa, Y., & Sato, S. (2005). Generation of a radially polarized laser beam by use of a conical Brewster prism. *Optics letters*, 30(22), 3063-3065.
- Kozawa, Y., & Sato, S. (2010). Optical trapping of micrometer-sized dielectric particles by cylindrical vector beams. *Optics express*, 18(10), 10828-10833.
- Kumar, R., Mehta, D. S., Sachdeva, A., Garg, A., Senthilkumaran, P., & Shakher, C. (2008). Generation and detection of optical vortices using all fiber-optic system. *Optics Communications*, 281(13), 3414-3420.
- Lazarev, G., Hermerschmidt, A., Krüger, S., & Osten, S. (2012). LCOS spatial light modulators: trends and applications. *Optical Imaging and Metrology: Advanced Technologies*, 1-29.
- Levy, U., Tsai, C.-H., Pang, L., & Fainman, Y. (2004). Engineering space-variant inhomogeneous media for polarization control. *Optics letters*, 29(15), 1718-1720.
- Li, G., Bai, N., Zhao, N., & Xia, C. (2014). Space-division multiplexing: the next frontier in optical communication. *Advances in Optics and Photonics*, 6(4), 413-487.
- Li, H., Ren, G., Lian, Y., Zhu, B., Tang, M., Zhao, Y., & Jian, S. (2016). Broadband orbital angular momentum transmission using a hollow-core photonic bandgap fiber. *Optics letters*, 41(15), 3591-3594.
- Li, L., & Li, F. (2013). Beating the Rayleigh limit: Orbital-angular-momentum-based super-resolution diffraction tomography. *Physical Review E*, 88(3), 033205.

- Li, M., Yan, S., Zhang, Y., Liang, Y., Zhang, P., & Yao, B. (2019). Optical sorting of small chiral particles by tightly focused vector beams. *Physical Review A*, *99*(3), 033825.
- Li, S., & Wang, J. (2015). Adaptive power-controllable orbital angular momentum (OAM) multicasting. *Scientific reports*, *5*(1), 1-7.
- Lin, Q., & Agrawal, G. P. (2006). Raman response function for silica fibers. *Optics letters*, *31*(21), 3086-3088.
- Liu, J., Li, S.-M., Zhu, L., Wang, A.-D., Chen, S., Klitis, C., . . . Yu, S.-Y. (2018). Direct fiber vector eigenmode multiplexing transmission seeded by integrated optical vortex emitters. *Light: Science & Applications*, *7*(3), 17148-17148.
- Liu, K., Cheng, Y., Gao, Y., Li, X., Qin, Y., & Wang, H. (2017). Super-resolution radar imaging based on experimental OAM beams. *Applied Physics Letters*, *110*(16), 164102.
- Ma, Z., & Ramachandran, S. (2020). Propagation stability in optical fibers: role of path memory and angular momentum. *Nanophotonics*, *1*(ahead-of-print).
- Marrucci, L., Karimi, E., Slussarenko, S., Piccirillo, B., Santamato, E., Nagali, E., & Sciarrino, F. (2011). Spin-to-orbital conversion of the angular momentum of light and its classical and quantum applications. *Journal of Optics*, *13*(6), 064001.
- Mushiake, Y., Matsumura, K., & Nakajima, N. (1972). Generation of radially polarized optical beam mode by laser oscillation. *Proceedings of the IEEE*, *60*(9), 1107-1109.
- Muslu, G., & Erbay, H. (2003). A split-step Fourier method for the complex modified Korteweg-de Vries equation. *Computers & Mathematics with Applications*, *45*(1-3), 503-514.
- Neshev, D. N., Dreischuh, A., Maleshkov, G., Samoc, M., & Kivshar, Y. S. (2010). Supercontinuum generation with optical vortices. *Optics express*, *18*(17), 18368-18373.
- Niederriter, R., Siemens, M., & Gopinath, J. (2015). Fiber optic sensors based on orbital angular momentum. Dans *2015 Conference on Lasers and Electro-Optics (CLEO)* (pp. 1-2). IEEE.
- Padgett, M. (2014). Light's twist. *Proceedings of the Royal Society A: Mathematical, Physical and Engineering Sciences*, *470*(2172), 20140633.
- Padgett, M., & Bowman, R. (2011). Tweezers with a twist. *Nature photonics*, *5*(6), 343.

- Pakarzadeh, H., & Sharif, V. (2019). Control of orbital angular momentum of light in optofluidic infiltrated circular photonic crystal fibers. *Optics Communications*, 438, 18-24.
- Pohl, D. (1972). Operation of a ruby laser in the purely transverse electric mode TE₀₁. *Applied Physics Letters*, 20(7), 266-267.
- Pollock, J. G., Iyer, A. K., Pratap, D., & Anantha Ramakrishna, S. (2016). A class of circular waveguiding structures containing cylindrically anisotropic metamaterials: Applications from radio frequency/microwave to optical frequencies. *Journal of Applied Physics*, 119(8), 083103.
- Prabhakar, G., Gregg, P., Rishøj, L., & Ramachandran, S. (2016). In-fiber monomode octave-spanning oam supercontinuum. Dans *2016 Conference on Lasers and Electro-Optics (CLEO)* (pp. 1-2). IEEE.
- Pradhan, P., Sharma, M., & Ung, B. (2018). Generation of perfect cylindrical vector beams with complete control over the ring width and ring diameter. *IEEE Photonics Journal*, 10(1), 1-10.
- Pratap, D., Bhardwaj, A., & Ramakrishna, S. A. (2018). Inhomogeneously filled, cylindrically anisotropic metamaterial optical fiber. *Journal of Nanophotonics*, 12(3), 033002.
- Pratap, D., Ramakrishna, S. A., Pollock, J. G., & Iyer, A. K. (2015). Anisotropic metamaterial optical fibers. *Optics express*, 23(7), 9074-9085.
- Qiao, W., Lei, T., Wu, Z., Gao, S., Li, Z., & Yuan, X. (2017). Approach to multiplexing fiber communication with cylindrical vector beams. *Optics letters*, 42(13), 2579-2582.
- Ramachandran, S., Gregg, P., Kristensen, P., & Golowich, S. (2015). On the scalability of ring fiber designs for OAM multiplexing. *Optics express*, 23(3), 3721-3730.
- Ramachandran, S., & Kristensen, P. (2013). Optical vortices in fiber. *Nanophotonics*, 2(5-6), 455-474.
- Ramachandran, S., Kristensen, P., & Yan, M. F. (2009). Generation and propagation of radially polarized beams in optical fibers. *Optics letters*, 34(16), 2525-2527.
- Ramachandran, S., Wang, Z., & Yan, M. (2002). Bandwidth control of long-period grating-based mode converters in few-mode fibers. *Optics letters*, 27(9), 698-700.

- Rao, Y. J., Ribeiro, A. L., Jackson, D. A., Zhang, L., & Bennion, I. (1995). Combined spatial-and time-division-multiplexing scheme for fiber grating sensors with drift-compensated phase-sensitive detection. *Optics letters*, *20*(20), 2149-2151.
- Ren, Y., Li, L., Wang, Z., Kamali, S. M., Arbabi, E., Arbabi, A., . . . Ahmed, N. (2016). Orbital angular momentum-based space division multiplexing for high-capacity underwater optical communications. *Scientific reports*, *6*, 33306.
- Ren, Y., Wang, Z., Xie, G., Li, L., Cao, Y., Liu, C., . . . Zhao, Z. (2015). Free-space optical communications using orbital-angular-momentum multiplexing combined with MIMO-based spatial multiplexing. *Optics letters*, *40*(18), 4210-4213.
- Richardson, D., Fini, J., & Nelson, L. E. (2013). Space-division multiplexing in optical fibres. *Nature photonics*, *7*(5), 354-362.
- Richardson, D. J. (2010). Filling the light pipe. *Science*, *330*(6002), 327-328.
- Rosales-Guzmán, C., Bhebhe, N., & Forbes, A. (2017). Simultaneous generation of multiple vector beams on a single SLM. *Optics express*, *25*(21), 25697-25706.
- Rubano, A., Cardano, F., Piccirillo, B., & Marrucci, L. (2019). Q-plate technology: a progress review. *JOSA B*, *36*(5), D70-D87.
- Rumala, Y. S., Milione, G., Nguyen, T. A., Pratavieira, S., Hossain, Z., Nolan, D., . . . Alfano, R. R. (2013). Tunable supercontinuum light vector vortex beam generator using a q-plate. *Optics letters*, *38*(23), 5083-5086.
- Rusch, L. A., Rad, M., Allahverdyan, K., Fazal, I., & Bernier, E. (2018). Carrying data on the orbital angular momentum of light. *IEEE Communications Magazine*, *56*(2), 219-224.
- Saitoh, K., & Koshiba, M. (2005). Empirical relations for simple design of photonic crystal fibers. *Optics express*, *13*(1), 267-274.
- Saitoh, K., & Matsuo, S. (2013). Multicore fibers for large capacity transmission. *Nanophotonics*, *2*(5-6), 441-454.
- Saripalli, R. K., Ghosh, A., Apurv Chaitanya, N., & Samanta, G. (2019). Frequency-conversion of vector vortex beams with space-variant polarization in single-pass geometry. *Applied Physics Letters*, *115*(5), 051101.
- Schmiegelow, C. T., Schulz, J., Kaufmann, H., Ruster, T., Poschinger, U. G., & Schmidt-Kaler, F. (2016). Transfer of optical orbital angular momentum to a bound electron. *Nature communications*, *7*, 12998.

- Sharma, M., Amirkhan, F., Mishra, S. K., Sengupta, D., Messaddeq, Y., Blanchard, F., & Ung, B. (2020). Transmission of orbital angular momentum and cylindrical vector beams in a large-bandwidth annular core photonic crystal fiber. *Fibers*, 8(4), 22.
- Sharma, M., Pradhan, P., & Ung, B. (2019a). Endlessly mono-radial annular core photonic crystal fiber for the broadband transmission and supercontinuum generation of vortex beams. *Scientific reports*, 9(1), 2488.
- Sharma, M., Pradhan, P., & Ung, B. (2019b). Endlessly mono-radial annular core photonic crystal fiber for the broadband transmission and supercontinuum generation of vortex beams. *Scientific reports*, 9(1), 1-12.
- Shtaif, M. (2008). Performance degradation in coherent polarization multiplexed systems as a result of polarization dependent loss. *Optics express*, 16(18), 13918-13932.
- Siegman, A. E., Sasnett, M., & Johnston, T. (1991). Choice of clip levels for beam width measurements using knife-edge techniques. *IEEE Journal of Quantum Electronics*, 27(4), 1098-1104.
- Snoeyink, C., & Wereley, S. (2013). Single-image far-field subdiffraction limit imaging with axicon. *Optics letters*, 38(5), 625-627.
- Snyder, A. W., & Love, J. (2012). *Optical waveguide theory*. Springer Science & Business Media.
- Tandjè, A., Yammine, J., Bouwmans, G., Dossou, M., Vianou, A., Andresen, E. R., & Bigot, L. (2018). Design and Fabrication of a Ring-Core Photonic Crystal Fiber for Low-Crosstalk Propagation of OAM Modes. Dans *2018 European Conference on Optical Communication (ECOC)* (pp. 1-3). IEEE.
- Tandjè, A., Yammine, J., Dossou, M., Bouwmans, G., Baudelle, K., Vianou, A., . . . Bigot, L. (2019). Ring-core photonic crystal fiber for propagation of OAM modes. *Optics letters*, 44(7), 1611-1614.
- Tian, N., Fu, L., & Gu, M. (2015). Resolution and contrast enhancement of subtractive second harmonic generation microscopy with a circularly polarized vortex beam. *Scientific reports*, 5(1), 1-8.
- Tokizane, Y., Oka, K., & Morita, R. (2009). Supercontinuum optical vortex pulse generation without spatial or topological-charge dispersion. *Optics express*, 17(17), 14517-14525.

- Torner, L., Torres, J. P., & Carrasco, S. (2005). Digital spiral imaging. *Optics express*, 13(3), 873-881.
- Trichili, A., Park, K.-H., Zghal, M., Ooi, B. S., & Alouini, M.-S. (2019). Communicating using spatial mode multiplexing: Potentials, challenges, and perspectives. *IEEE Communications Surveys & Tutorials*, 21(4), 3175-3203.
- Ung, B., Vaity, P., Wang, L., Messaddeq, Y., Rusch, L., & LaRochelle, S. (2014). Few-mode fiber with inverse-parabolic graded-index profile for transmission of OAM-carrying modes. *Optics express*, 22(15), 18044-18055.
- Ung, B., Wang, L., Brunet, C., Vaity, P., Jin, C., Rusch, L., . . . LaRochelle, S. (2014). Inverse-parabolic graded-index profile for transmission of cylindrical vector modes in optical fibers. Dans *Optical Fiber Communication Conference* (pp. Tu3K. 4). Optical Society of America.
- Volpe, G., & Petrov, D. (2004). Generation of cylindrical vector beams with few-mode fibers excited by Laguerre–Gaussian beams. *Optics Communications*, 237(1-3), 89-95.
- Wang, L., Nejad, R. M., Corsi, A., Lin, J., Messaddeq, Y., Rusch, L., & LaRochelle, S. (2017). Linearly polarized vector modes: enabling MIMO-free mode-division multiplexing. *Optics express*, 25(10), 11736-11749.
- Weber, R., Michalowski, A., Abdou-Ahmed, M., Onuseit, V., Rominger, V., Kraus, M., & Graf, T. (2011). Effects of radial and tangential polarization in laser material processing. *Physics Procedia*, 12, 21-30.
- Wildanger, D., Rittweger, E., Kastrup, L., & Hell, S. W. (2008). STED microscopy with a supercontinuum laser source. *Optics express*, 16(13), 9614-9621.
- Willner, A. E., Huang, H., Yan, Y., Ren, Y., Ahmed, N., Xie, G., . . . Zhao, Z. (2015). Optical communications using orbital angular momentum beams. *Advances in Optics and Photonics*, 7(1), 66-106.
- Willner, A. E., Xie, G., Li, L., Ren, Y., Yan, Y., Ahmed, N., . . . Willner, A. J. (2016). Design challenges and guidelines for free-space optical communication links using orbital-angular-momentum multiplexing of multiple beams. *Journal of Optics*, 18(7), 074014.
- Witkowska, A., Leon-Saval, S., Pham, A., & Birks, T. (2008). All-fiber LP 11 mode convertors. *Optics letters*, 33(4), 306-308.

- Wong, G., Kang, M. S., Lee, H., Biancalana, F., Conti, C., Weiss, T., & Russell, P. S. J. (2012). Excitation of orbital angular momentum resonances in helically twisted photonic crystal fiber. *Science*, 337(6093), 446-449.
- Wu, J.-Y., Kingsland, D. M., Lee, J.-F., & Lee, R. (1997). A comparison of anisotropic PML to Berenger's PML and its application to the finite-element method for EM scattering. *IEEE Transactions on Antennas and Propagation*, 45(1), 40-50.
- Yan, L., Gregg, P., Karimi, E., Rubano, A., Marrucci, L., Boyd, R., & Ramachandran, S. (2015). Q-plate enabled spectrally diverse orbital-angular-momentum conversion for stimulated emission depletion microscopy. *Optica*, 2(10), 900-903.
- Yan, L., Kristensen, P., & Ramachandran, S. (2019). Vortex fibers for STED microscopy. *Apl Photonics*, 4(2), 022903.
- Yao, A. M., & Padgett, M. J. (2011). Orbital angular momentum: origins, behavior and applications. *Advances in Optics and Photonics*, 3(2), 161-204.
- Ye, J., Li, Y., Han, Y., Deng, D., Guo, Z., Gao, J., . . . Qu, S. (2016). Excitation and separation of vortex modes in twisted air-core fiber. *Optics express*, 24(8), 8310-8316.
- Yi, X., Ling, X., Zhang, Z., Li, Y., Zhou, X., Liu, Y., . . . Wen, S. (2014). Generation of cylindrical vector vortex beams by two cascaded metasurfaces. *Optics express*, 22(14), 17207-17215.
- Yijiang, C. (1987). Anisotropic fiber with cylindrical polar axes. *Applied Physics B*, 42(1), 1-3.
- Yimin, Z., Tao, R., Li, H., Fang, W., Dong, Z., Dai, C., . . . Zhu, Y. (2020). Stable generation of cylindrical vector beams with an all-fiber laser using polarization-maintaining and ring-core fibers. *Optics express*, 28(12), 18351-18359.
- Youngworth, K. S., & Brown, T. G. (2000). Focusing of high numerical aperture cylindrical-vector beams. *Optics express*, 7(2), 77-87.
- Yu, W., Ji, Z., Dong, D., Yang, X., Xiao, Y., Gong, Q., . . . Shi, K. (2016). Super-resolution deep imaging with hollow Bessel beam STED microscopy. *Laser & Photonics Reviews*, 10(1), 147-152.
- Yue, Y., Zhang, L., Yan, Y., Ahmed, N., Yang, J.-Y., Huang, H., . . . Willner, A. E. (2012). Octave-spanning supercontinuum generation of vortices in an As₂S₃ ring photonic crystal fiber. *Optics letters*, 37(11), 1889-1891.

- Zeng, J., Wang, X., Sun, J., Pandey, A., Cartwright, A. N., & Litchinitser, N. M. (2013). Manipulating complex light with metamaterials. *Scientific reports*, 3, 2826.
- Zhan, Q. (2009). Cylindrical vector beams: from mathematical concepts to applications. *Advances in Optics and Photonics*, 1(1), 1-57.
- Zhang, H., Mao, B., Han, Y., Wang, Z., Yue, Y., & Liu, Y. (2019). Generation of orbital angular momentum modes using fiber systems. *Applied Sciences*, 9(5), 1033.
- Zhang, H., Zhang, X., Li, H., Deng, Y., Xi, L., Tang, X., & Zhang, W. (2017). The orbital angular momentum modes supporting fibers based on the photonic crystal fiber structure. *Crystals*, 7(10), 286.
- Zhang, L., Zhang, K., Peng, J., Deng, J., Yang, Y., & Ma, J. (2018). Circular photonic crystal fiber supporting 110 OAM modes. *Optics Communications*, 429, 189-193.
- Zhang, W., Wei, K., Huang, L., Mao, D., Jiang, B., Gao, F., . . . Zhao, J. (2016). Optical vortex generation with wavelength tunability based on an acoustically-induced fiber grating. *Optics express*, 24(17), 19278-19285.
- Zhao, H., Wang, P., Yamakawa, T., & Li, H. (2019). All-fiber second-order orbital angular momentum generator based on a single-helix helical fiber grating. *Optics letters*, 44(21), 5370-5373.
- Zhao, Y., Liu, Y., Zhang, C., Zhang, L., Zheng, G., Mou, C., . . . Wang, T. (2017). All-fiber mode converter based on long-period fiber gratings written in few-mode fiber. *Optics letters*, 42(22), 4708-4711.
- Zhao, Z., Wang, J., Li, S., & Willner, A. E. (2013). Metamaterials-based broadband generation of orbital angular momentum carrying vector beams. *Optics letters*, 38(6), 932-934.
- Zheng, R., Gu, C., Wang, A., Xu, L., & Ming, H. (2010). An all-fiber laser generating cylindrical vector beam. *Optics express*, 18(10), 10834-10838.
- Zhu, Z., & Brown, T. G. (2001). Analysis of the space filling modes of photonic crystal fibers. *Optics express*, 8(10), 547-554.